Characterization and Modeling of Smooth and Notched Rolled ZEK100-O under Cyclic Load

by

Yi Ling

A thesis

presented to the University of Waterloo

in the fulfillment of the

thesis requirement for the degree of

Master of Applied Science

in

Mechanical and Mechatronics Engineering

Waterloo, Ontario, Canada, 2018

Author's Declaration

I hereby declare that I am the sole author of this thesis. This is a true copy of the thesis, including any required final revisions, as accepted by my examiners.

I understand that my thesis may be made electronically available to the public.

Abstract

As an effective way to reduce greenhouse gas emissions, goals on weight reduction has been focused by automotive manufacturers to meet the environmental regulations. Magnesium (Mg) alloys, with its high specific strength and low density, are particularly attractive to applications where light-weight is a part of its objective. However, Magnesium alloys with its unique crystallographic structure (Hexagonal Close Packing) provide different deformation mechanisms in contrast to steel or Aluminum alloys are currently been used for load-bearing components which have to be studied. As fatigue failure is a major concern, this thesis aims to characterize the stress-strain response as well as fatigue properties of ZEK100-O rolled sheet and to model the stress-strain responses and fatigue properties at the notch root where the crack is most likely to initiate due to the stress concentration when a notch is present.

Initially, the cyclic behavior of rolled ZEK100-O Magnesium alloy sheet has been investigated by performing fully-reversed and strain-controlled tension-compression tests with the strain amplitude span from 0.3% to 2.3% on the smooth specimen and load-controlled cyclic tests on notched specimens. In addition, the fatigue properties of the material are also investigated by fitting the fatigue test results to the Smith-Watson-Topper (SWT) and Jahed-Varvani energy models.

Next, the phenomenological stress-strain model for asymmetric materials proposed by Dallmeier et al. has been implemented using the fully-reversed and strain-controlled tension-compression test results on ZEK100-O and results available on AZ31B-H24 which have shown good agreement. A MATLAB code has been written to obtain all the necessary material parameters from one single hysteresis which has visible twin exhaustion and further investigation shown that a stress-strain hysteresis with a strain amplitude of 2% is sufficient. With an additional cyclic stress-strain curve (CSSC) input, the MATLAB code is capable of predicting the stress-strain responses for a given strain history.

Furthermore, the cyclic behavior and fatigue properties of rolled ZEK100-O and AZ31B-H24 Magnesium alloy notched sample has been investigated by performing fully-reversed load-controlled tension and compression tests. To induce sufficient amount of plasticity yet to prevent general yielding at the notch root, the applied nominal load has been chosen based on its compressive yield stress, which is lower in contrast to its tensile yield stress. Given an elastic stress concentration factor of 2.5 at the notch root based on the test sample geometry, four different nominal stress levels (50%, 60%, 70% and 80% of compressive yield stress equivalent load) were chosen. The strain field around the notch root during the cyclic loading has been captured using the digital image correlation (DIC) technique. In addition, the

crack initiation and propagation have also been captured simultaneously using DIC for its fatigue properties.

The strain predictions at the notch root at the end of each loading segment using both Neuber's and Glinka's rule have been examined on both ZEK100-O and AZ31B-H24 based on the strain measurements at the notch root. It has been found that the strain predictions are reasonably close to the experimentally obtained value for both Neuber's and Glinka's rule. However, the strain prediction using Neuber's rule tend to give a larger value in contrast to Glinka's rule, which is more conservative as long as life prediction is concerned. At the same time, the effects of the stress state at the notch root (plane stress or plane strain) to the axial strain measurements have also been studied by performing additional fully-reversed load-controlled tension and compression tests on notched samples with different thicknesses.

Finally, upon the existing MATLAB code which is capable of predicting the stress-strain responses for a given strain history, notch analysis based on Neuber's and Glinka's methods have been integrated by applying either Neuber's or Glinka's rule upon the stress-strain curve generated using the phenomenological model for each reversal. Additionally, the plane strain correction has been used to obtain the stress-strain responses at the notch root under plane strain condition from the plane stress solution. Having the stress-strain responses at the notch root, a modified SWT and Jahed-Varvani (J-V) energy model based on the uniaxial fully-reversed and strain-controlled tension-compression fatigue test results on smooth samples incorporate with Miner's rule have been used to ultimately predict the life of a notch member providing its elastic stress concentration factor and nominal load history. The life predictions on the notch members under both constant and variable amplitude loads have been examined on ZEK100-O and AZ31B-H24 which yield good results.

Acknowledgments

I would like to express my sincerest gratitude to my supervisors, Professor Hamid Jahed and Professor Grzegorz Glinka for this amazing journey, for all the invaluable support, advice and guidance.

Special thanks to Dr. Yung-Li Lee, Dr. Yibing Shi, Umesh Dighrasker, Marie Mills and Mohammed Malik at Fiat Chrysler Automobiles (FCA) for all the great discussions and advice.

Additionally, I would also like to thank Ali A. Roostaei for all the support and suggestions.

Lastly, I would like to express my deepest love to my parents, this journey would not have been possible without their supports and encouragements.

Table of Contents

List of Figures

List of tables

Chapter 1: Introduction

The greenhouse gas emissions by human activities are believed to be the major cause of global warming and the rise of the sea levels over the last few decades [1] . Statistics by the United States Environmental Protection Agency have shown that, in 2016, the transportation sector contributes to 28% of the total greenhouse gas emissions in the US, as shown in Figure 1:

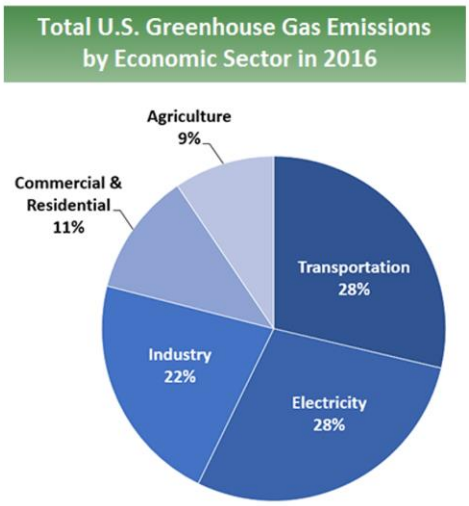

Figure 1. Total U.S. Greenhouse gas emissions by economic sector in 2016. (Total Emissions in 2016 = 6,511 Million Metric Tons of CO_2 equivalent) [2]

Governments around the world have set the regulations for the automotive manufactures in order to suppress the carbon dioxide emission from the burn of fossil fuels. Many technologies have been developed over the years to reduce the emissions of the internal combustion engines, such as exhaust gas recirculation (EGR), lean-burn technology, etc. Additionally, electric vehicles have also been developed to achieve the goal of zero emission in recent years.

To further reduce the emission and energy consumption, an effective way is to reduce the vehicle weight, which can ultimately reduce the amount of energy needed for the acceleration and at the same time, reduce the amount of energy dissipated as heat through the break during the deceleration.

The concept of light weighting involves the use of new types of materials which is lighter in weight yet retains the structural integrity over time. Magnesium alloys are good candidates for this application due to its high specific strength and high specific stiffness. However, magnesium alloys exhibit anisotropy as well as tension-compression asymmetry [3] [4] , which cannot be easily modeled using the traditional

methods for symmetric materials. In addition to that, magnesium alloys also exhibit poor formability due to its unique HCP (hexagonal close-packed) crystal structure which has only a limit number of deformation mechanisms at room temperature. To mitigate these problems, new types of magnesium alloys have been developed over the years with the addition of rare-earth elements such as Ce, Nd, La, etc. ZEK100-O is a relatively new type of rare-earth (RE) contained magnesium alloy with good room temperature formability. To be able to properly design load-bearing components made of ZEK100-O magnesium alloy, the quasi-static and cyclic properties of ZEK100-O were studied.

To be able to properly model the cyclic stress-strain behaviors of magnesium alloys under uniaxial load, the phenomenological model proposed by Dallmeier et al. [5] for wrought magnesium alloys has been studied and examined on ZEK100-O and AZ31B-H24, which yield good results.

The stress-strain responses at the notch root under fully-reversed nominal stresses for both ZEK100-O and AZ31B-H24 were studied too. To be able to predict the stress-strain responses and ultimately predict the fatigue life of the notched components, both Neuber's and Glinka's (ESED) approximation methods were examined on both ZEK100-O and AZ31B-H24. With the help of the phenomenological model and the plane strain correction by Dowling, N. [6] , both Neuber's and Glinka's approximation methods provide notch strain predictions with a reasonable accuracy.

Besides, two fatigue models: Smith-Watson-Topper (SWT) [7] , which is using a strain-based approach and Jahed-Varvani model (later referred to as the J-V energy model) [8] [9] , which is using an energy-based approach are both examined on ZEK100-O. Due to the assumption made by SWT, which assumes the fully-reversed strain-controlled tests are also fully-reversed in stress is not true for ZEK100-O due to the tension-compression asymmetry, the strain versus life curve has been used to directly fit to the SWT relation instead of Coffin-Manson relation (later referred to as the SWT direct-fit). Both SWT direct-fit and J-V energy model yield good predictions on the fatigue life of ZEK100-O magnesium alloy.

Finally, a notch analysis program has been developed and coded in MATLAB to incorporate the phenomenological model with Neuber's and Glinka's rule to first predict the local stress-strain responses at the vicinity of the notch root, then use SWT direct-fit and J-V energy model to ultimately predict the fatigue life of a given notched member.

As a brief overview, the major objectives of this thesis are four folds:

1) The characterization of the stress-strain responses and fatigue behaviors of ZEK100-O on smooth and notched specimens
2) Modeling of the stress-strain hysteresis loops for magnesium alloys using the phenomenological model proposed by Dallmeier et al.
3) Assess and implement the Neuber's and Glinka's approximation method upon the phenomenological model for the notch analysis on magnesium alloys
4) Assess and integrate the fatigue models (SWT direct-fit and J-V energy model) to the smooth sample and notch analysis

Chapter 2 contains the literature review of the general properties of magnesium alloys and of the material to be investigated, namely, ZEK100. Besides, the phenomenological model by Dallmeier et al. [5] is discussed in detail. Finally, the knowledge about the approximation methods for the notch analysis (Neuber's rule and Glinka's rule) presented in the current literature is also reviewed.

Chapter 3 presents the experimental characterization of the quasi-static, cyclic and fatigue properties of ZEK100-O. Notch responses of ZEK100-O and additional tests on notched AZ31B-H24 notched specimens have also been discussed, which will be used to validate the notch response predictions using the approximation methods.

Chapter 4 is dedicated to the modeling of the stress-strain hysteresis loops using the phenomenological model by Dallmeier et al. [5] and the implementation of the approximation methods (Neuber's and Glinka's rule) for notch analysis.

Chapter 5 discusses the two fatigue models been used to model the fatigue behaviors of ZEK100-O, namely, SWT and Jahed-Varvani models. Besides, Miner's rule is also examined for the fatigue life predictions of both smooth and notched specimens under variable amplitude loads.

Chapter 6 is focusing on the discussion of the capabilities and input requirements of the developed notch analysis MATLAB program. In addition to that, flowcharts are also presented to give a brief overview of how the core of the MATLAB program is working.

Chapter 7 summarizes all the conclusions of the work presented from chapter 2 to chapter 6. Furthermore, some recommendations of the future work are also provided at the end.

Chapter 2: Literature review

Magnesium and its alloys typically exhibit poor formability, anisotropy as well as tension-compression asymmetry at room temperature [3] [4] which is distinct from strength-differential effect reported in high strength steels [10] .The poor formability is due to its unique HCP (hexagonal close-packed) crystal structure, which has only a limit numbers of deformation mechanisms, specifically, basal <a>, prismatic <a>, pyramidal <a> and pyramidal <c+a> slip systems [13] , shown in Figure 2-a.

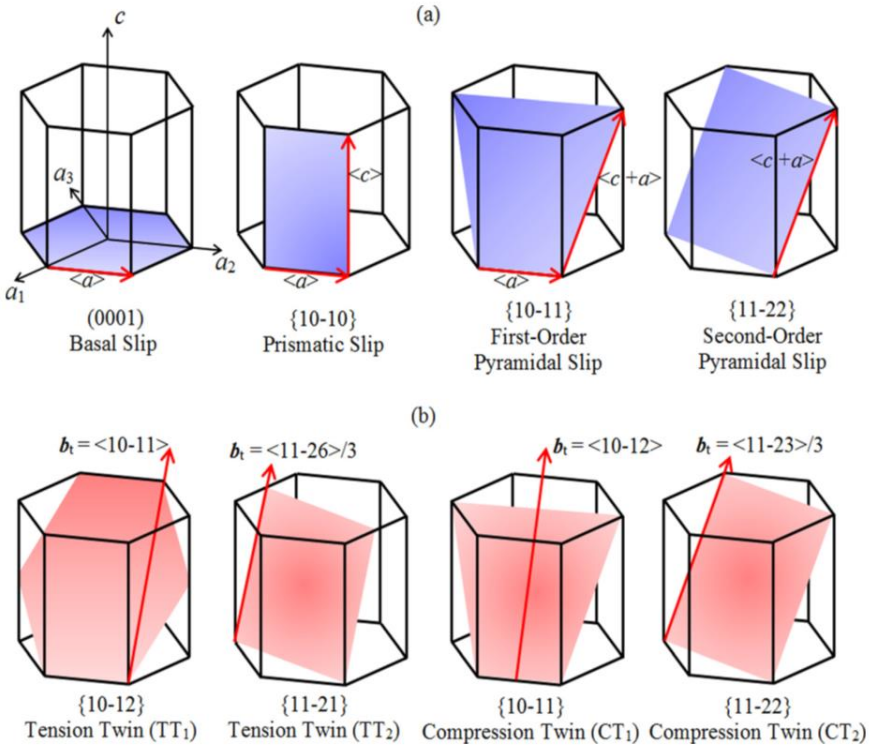

Figure 2. Schematic of the HCP unit cell showing all possible: (a) slip and (b) twinning systems [12]

These slip systems can be activated at different levels of CRSS (critical resolved shear stress) and at the room temperature, basal <a> slip is the only slip system available since other slip systems require a relatively higher CRSS [14] - [16] . Another deformation mechanism dedicated to HCP crystal is twinning, shown in Figure 2-b. There are two active twinning mechanisms in magnesium which are the contraction twinning (TT_1) and extension twinning (CT_1) [17] The contraction twinning permits the HCP unit cell to contract in its c-axis, as the c-axis is re-oriented by 56.2 degrees, whereas the extension twinning permits the unit cell to elongate in its c-axis, while the c-axis re-oriented by 86.3 degrees [4] . It has been

shown that twinning can be activated by direct or indirect extension or contraction of the c-axis [20] -[22] . Due to the manufacturing process of the rolled sheet magnesium alloy, strong basal textures are normally developed where the c-axis lying almost orthogonal to the surface of the sheet. As a result, wrought magnesium alloys normally exhibit tension-compression asymmetric and directional anisotropy [23] -[29] .

It has been shown that the addition of the RE (rare-earth) elements weakens the basal texture of the rolled magnesium alloys, which improves the ductility and reduces the tension-compression asymmetry by suppressing the twinning process [30] -[32] . T. Al-Samman et al. suggested that the highly soluble rare-earth elements such as Ga and Nd atoms segregate to the grain boundaries and affect the grain boundary motion, which alters the recrystallization and grain growth. The solute clusters cause strain heterogeneity and influence the nucleation and growth process of recrystallization [58] .

There have been numerous studies on fatigue of wrought magnesium alloys including AZ31B extrusion, forged and sheets [33] -[45] , ZK60 extrusion and forged [46] -[48] , AM30 extrusion [49] -[54] , and AZ80 extrusion and forged [55] -[57] . However, studies on ZEK100 has been limited. ZEK100-O is a relatively new type of commercial RE-containing magnesium alloy. The O-temper indicates that the material has been annealed to remove any cold work in the rolling process [30] . The elemental composition is given in Table 1:

Zn	Nd	Zr	Mn	Mg
1.3 (wt%)	0.2 (wt%)	0.25 (wt%)	0.01 (wt%)	Balance

Table 1. ZEK100-O elemental composition [58]

It has been shown by few authors that, the initial texture of the RE-contained ZEK100-O magnesium alloy exhibit a relatively weaker basal texture and a significant spread of the basal poles along the transverse direction (TD) are found [4] [22] [30] [31] . The electron backscatter diffraction (EBSD) figures of sheet ZEK100 and AZ31B, which is a common type of commercially available magnesium alloy are shown in Figure 3 by Atish K. Ray et al. [62] :

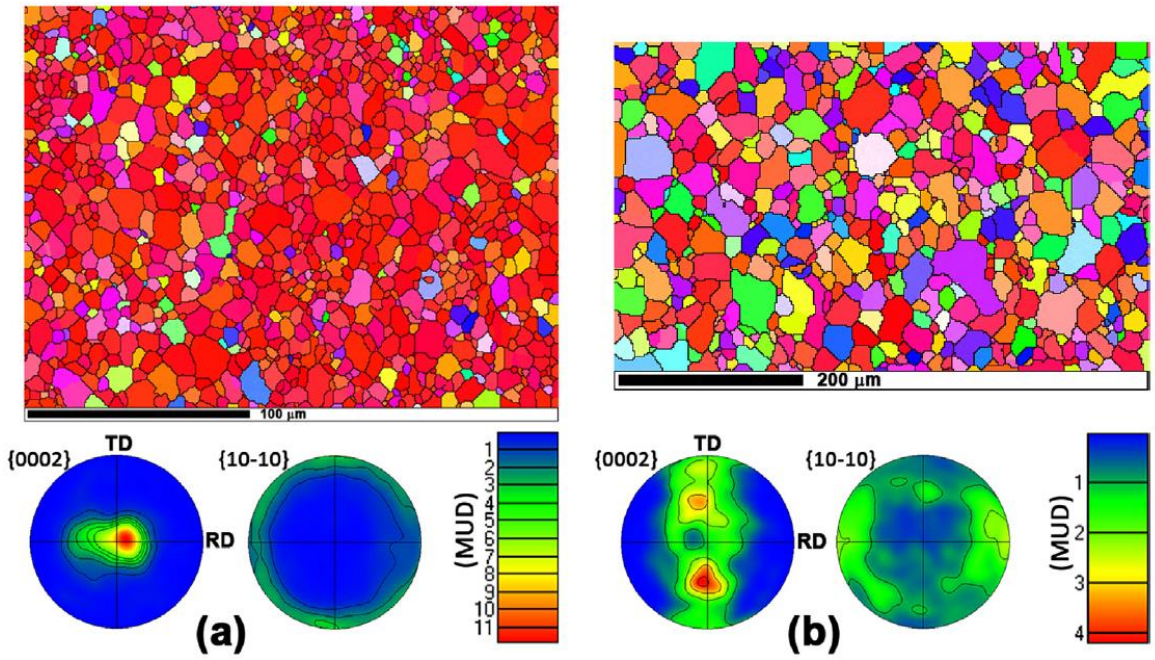

Figure 3. EBSD Initial texture and pole figures of (a) AZ31B and (b) ZEK100 [62]

It can be seen that the basal poles for ZEK100 are scattered in the transverse direction (TD) whereas the majority of the basal poles are normal to the sheet surface for AZ31B. Not to mention that the intensities of the basal poles for ZEK100 is much lower than AZ31B, which indicates a much weaker basal texture found in ZEK100. In addition to the effect of the added rare-earth element neodymium (Nd) in ZEK100 weakens the basal texture [58] , F. Mokdad et al. suggested that the dissolved Zirconium (Zr) in ZEK100 could refine the grains by effectively limit the growth of nucleating magnesium grains via solute segregation while the subsequent constitutional undercooling promoted heterogeneous nucleation events ahead of the solidification front [59] -[61] .

Due to the spread of basal poles of ZEK100 magnesium alloy in the transverse direction (TD), a relatively higher level of planar anisotropy can be expected. It has been experimentally shown by Waqas Muhammad et al. in Figure 4 [22] :

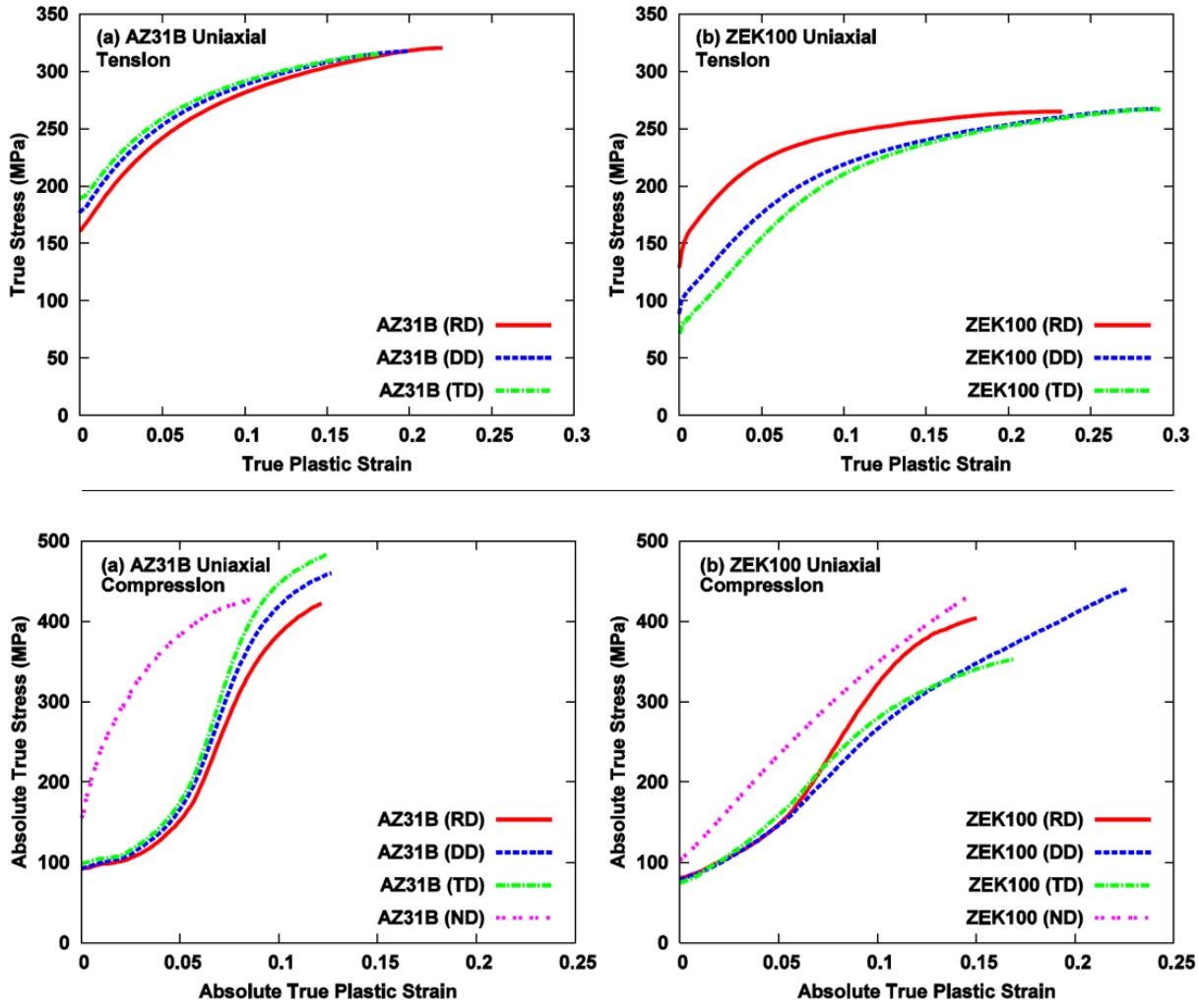

Figure 4. (a) AZ31B and (b) ZEK100 stress vs. plastic strain curve under monotonic tension and compression (Note that DD is the 45% direction in between RD and TD) [22]

A relatively higher planar anisotropy can be observed in ZEK100 under monotonic tension. Furthermore, the concaved shape of the flow curves in tension indicates a slip-dominated deformation whereas the sigmoidal shape of the compressive flow curves are results of the easily activated extension twinning at lower strain followed by the non-basal slip at higher strains due to the significantly lower CRSS value for extension twinning in comparison with non-basal slips under room temperature [23] [63] [64] [65] . It is also worthy to mention that; the flow stress is the highest in RD and lowest in TD for ZEK100.

As mentioned earlier, the extension twinning during the in-plane compression causes an 86.3 degree of re-orientation of the basal poles towards the in-plane loading direction [4] [19] . During in-plane reverse

tension, the previous twinned crystals may undergo a second extension twinning due to the stretch in the c-axis. However, the second extension twinning can proceed on any of the six available twinning planes depending on the critical resolved shear stress where only one of them would reorient the twinned zone back to the parent orientation [22] [66] . Consequently, the twinning and detwinning during cyclic loading lead to the asymmetry of the stress-strain hysteresis loops and the Bauschinger effect especially at higher strain amplitudes [23] [67] [68] .

The Ramberg-Osgood equation [69] accompanied with Masing hypothesis [70] are wildly used to model the stress-strain hysteresis loops for symmetric materials:

$$\varepsilon = \frac{\sigma}{E} + \left(\frac{\sigma}{K'}\right)^{1/n'} \quad (1)$$

$$\Delta\varepsilon = \frac{\sigma}{E} + 2\left(\frac{\Delta\sigma}{2K'}\right)^{1/n'} \quad (2)$$

Only three parameters are needed to model the stress-strain hysteresis loops, the cyclic strength coefficient (K'), cyclic strain hardening exponent (n') and the elastic modulus (E). Equation (1) applies to the first reversal and Equation (2), which doubles the stress and strain ranges applies to all the subsequent reversals as described by the Masing hypothesis [70] . Despite the benefits of using only three parameters to model the stress-strain behaviors, the stress-strain hysteresis loops modeled using Ramberg-Osgood equation is point symmetric, which is incapable to capture the unique asymmetric type of stress-strain responses of magnesium alloys. Furthermore, due to the different deformation mechanisms activated in tension and compression, the shapes of the stress-strain path for upward and downward reversals are different. Dallmeier, J. et al. have shown that a pool result can be found by modeling the stress-strain hysteresis loops of AM50 magnesium alloy using the Ramberg-Osgood equation and Masing hypothesis in Figure 5 [5] .

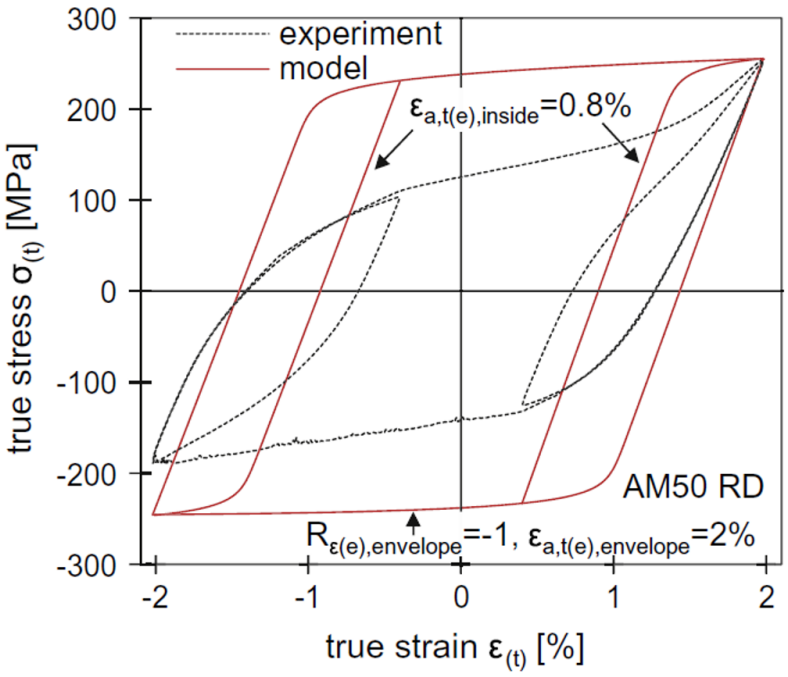

Figure 5. comparison of the Ramberg-Osgood-Masing model with experimentally determined variable amplitude hysteresis loops of AM50 by Dallmeier, J et al. [5]

To closely mimic the experimentally determined asymmetric stress-strain hysteresis loops of wrought magnesium alloys such as ZEK100-O, a phenomenological model has been proposed by Dallmeier, J et al. [5] . The phenomenological model is originally developed upon 1.2 mm thick twin roll cast AM50 magnesium alloy sheet but further proved that it works well on other types of wrought magnesium alloys as well. As described by Dallmeier, J et al., the phenomenological model breaks down the total relative strain to three fundamental components: elastic strain, plastic strain, and pseudo-elastic strain, as shown in Equation (3).

$$\Delta\varepsilon_{total}(\Delta\sigma) = \Delta\varepsilon_{el}(\Delta\sigma) + \Delta\varepsilon_{pl}(\Delta\sigma) + \Delta\varepsilon_{pseudo}(\Delta\sigma) \quad (3)$$

There are 8 parameters needed in total to model the stress-strain hysteresis loops of magnesium alloys by this phenomenological model, as shown in Table 2:

Parameters	Unit	Descriptions
E	MPa	Young's modulus
P	-	Material constant, representing the slope of the pseudo-elastic strain component
$\sigma_{p,up}$	MPa	Pseudo-elastic cut-off stress for ascending reversals
$\sigma_{p,down}$	MPa	Pseudo-elastic cut-off stress for descending reversals
T	-	Amount of plastic strain at the inflection point of the plastic strain component
S	-	Material constant, representing the slope at the inflection point of the plastic strain component
σ_{tw}	MPa	Stress at the inflection point of the plastic strain component of the descending reversal
R_r	-	Ratio between the reduction of both memory factors m_{pl} and m_{pseudo}

Table 2. Parameters been used in the phenomenological model by Dallmeier, J et al. [5]

The parameters $\sigma_{p,up}$ and $\sigma_{p,down}$ can be determined from the upward and downward reversals of an experimentally determined stress-strain hysteresis loop, where $\sigma_{p,up}$ and $\sigma_{p,down}$ are the stress ranges correspond to 20% of deviation in strain from linear elastic behavior from the reversing points. Parameter T, S and $\boldsymbol{\sigma_{tw}}$ are all linked to the inflection point of the stress versus plastic strain curve for the downward reversal. Parameter T is the strain range correspond to the inflection point on the stress versus plastic strain curve from the reversing point for the downward reversal. Parameter S is the slope at the reversing point in the stress versus plastic strain curve and $\boldsymbol{\sigma_{tw}}$ correspond to the global stress value at the inflection point. A visualization of these material constants using an experimentally determined hysteresis loop for AM50 by Dallmeier, J et al. [5] is shown in Figure 6:

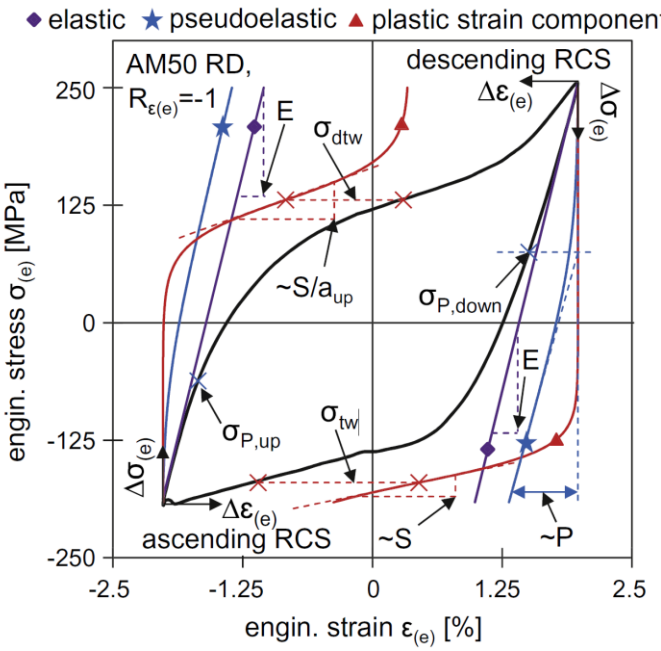

Figure 6. Visualization of material constants using an experimentally determined envelope hysteresis loop with the corresponding calculated strain components (AM50) by Dallmeier, J et al. [5]

And a list of these material parameters for various types of magnesium alloys by Dallmeier, J et al. [5] is shown in Table 3:

Parameters	**Unit**	**Expected ranges**	**AM50**	**ME21**	**AZ31B**	**AZ61A**
E	GPa	40 - 46	45.0	44.0	44.8	43.3
P	-	$5 \cdot 10^{-4} - 5 \cdot 10^{-3}$	$1.4 \cdot 10^{-3}$	$2.5 \cdot 10^{-3}$	$2.0 \cdot 10^{-3}$	$1.5 \cdot 10^{-3}$
$\sigma_{p,up}$	MPa	50 - 300	125	50	75	75
$\sigma_{p,down}$	MPa	50 - 300	175	100	225	125
T	-	0.01 - 0.1	0.037	0.04	0.04	0.05
S	-	15 - 60	35	25	50	50
σ_{tw}	MPa	(-50) - (-200)	-170	-77	-155	-135
R_r	-	0 - 1	0.6	0.05	0.8	0.5

Table 3. Values and expected ranges for various types of magnesium alloys by Dallmeier, J et al. [5]

The elastic strain component shown in Equation (3) is given in Equation (4):

$$\Delta\varepsilon(\Delta\sigma) = \frac{\Delta\sigma}{E} \tag{4}$$

Which is defined by the experimentally determined Young's modulus.

As mentioned earlier that, the deformation mechanisms for magnesium alloys are not only different for upward and downward reversals but also not the same at different stress levels. The alternation between twinning and detwinning also involved during cyclic loading, which gives the stress-strain hysteresis loop a distinct sigmoidal shape especially at a relatively higher stress amplitude [23] [74] . Due to these reasons, hyperbolic tangent functions have been used to model the plastic behaviors and the addition of the shape factor $a_{up/down}$ has been used to mimic the distinct shapes of the ascending and descending reversals. The function being used to model the plastic strain is given by Equation (5-7):

$$\Delta\varepsilon_{pl}(\Delta\sigma) = [U(\Delta\sigma) - U(\Delta\sigma = 0)] \cdot T \cdot m_{pl} \tag{5}$$

$$U(\Delta\sigma) = \frac{1}{2}\left[\tanh\left(\frac{\Delta\sigma - |\sigma_{rp}| + a_{up/down}\cdot\sigma_{tw}}{S} \cdot a_{up/down}\right) + 1\right] \tag{6}$$

$$a_{up/down} = \begin{cases} 1, \text{ downward reversal} \\ \frac{1}{2}\left(\tanh\frac{\Delta\sigma_{max} - |\sigma_{rp\,(dr)}| + \sigma_{tw}}{S} + 1\right), \text{ upward reversal} \end{cases} \tag{7}$$

By having different values of $a_{up/down}$ for upward and downward reversal in Equation (7), the difference in the shape of the upward and downward reversals can be properly modelled. Note that σ_{rp} is the global stress value at the reversing point for the current reversal, $\sigma_{rp\,(dr)}$ is the global stress value at the reversing point for the corresponding downward reversal, $\Delta\sigma_{max}$ is the stress range for the current reversal and m_{pl} is the plastic memory factor.

In addition to elastic and plastic behaviors, it has been observed in most of the magnesium alloys that, the unloading curves in both tensile and compressive regions are non-linear. This phenomenon is called pseudo-elastic behavior and in magnesium alloys, the pseudo-elastic strain is induced by reversible movement of grain boundaries due to internal driving forces [71] -[73] . The pseudo-elastic strain leads to a relatively larger hysteresis loop especially at lower stress amplitudes [71] . The pseudo-elastic strain component ($\Delta\varepsilon_{pseudo}$) has been modelled using a logarithmic function shown in Equation (8):

$$\Delta\varepsilon_{pseudo}(\Delta\sigma) = \ln\left(\frac{e^{\left(\Delta\sigma - \sigma_{p,up/down}\right)/50MPa + 1}}{e^{\left(-\sigma_{p,up/down}\right)/50MPa + 1}}\right) \cdot P \cdot m_{psel} \tag{8}$$

Notice that $\sigma_{p,up/down}$ takes different values for upward and downward reversals and m_{psel} is the pseudo-elastic memory factor.

One more relation correlates the pseudo-elastic memory factor (m_{psel}) with plastic memory factor (m_{pl}) shown in Equation (9):

$$R_r = \frac{1-m_{psel}}{1-m_{pl}} \quad (9)$$

Since all the parameters shown in Table 2 are fixed for the entire simulation for certain types of magnesium alloy, the only parameters change from one reversal to another are the pseudo-elastic memory factor (m_{psel}) and plastic memory factor (m_{pl}). By substitute Equation (4-8) into Equation (3), the relation between the relative stress ($\Delta\sigma$) and relative total strain ($\Delta\varepsilon$) can be established, except with the pseudo-elastic memory factor (m_{psel}) and plastic memory factor (m_{pl}) remain unknown. However, it is known that the reversing points of each reversal will land on the cyclic stress-strain curve (CSSC) for a stabilized fully reversed (R_{strain}=-1) strain-controlled test. Therefore, given the strain range ($\Delta\varepsilon_{max}$) for the envelope stress-strain hysteresis loop, the stress range ($\Delta\sigma_{max}$) can be determined from the experimental CSSC. Substitute the known stress range ($\Delta\sigma_{max}$) and strain range ($\Delta\varepsilon_{max}$) for each reversal into the relation between the relative stress ($\Delta\sigma$) and relative total strain ($\Delta\varepsilon$) and consider Equation (9), two equations with two unknows (m_{pl} & m_{psel}) can be established and the individual values for m_{pl} and m_{psel} then can be determined by solving the system of equations. Finally, known the values of m_{pl} and m_{psel}, the direct relation between the relative stress ($\Delta\sigma$) and relative total strain ($\Delta\varepsilon$) is established.

In a situation where the current reversal starts deviating from the envelope hysteresis loop as shown in Figure 7:

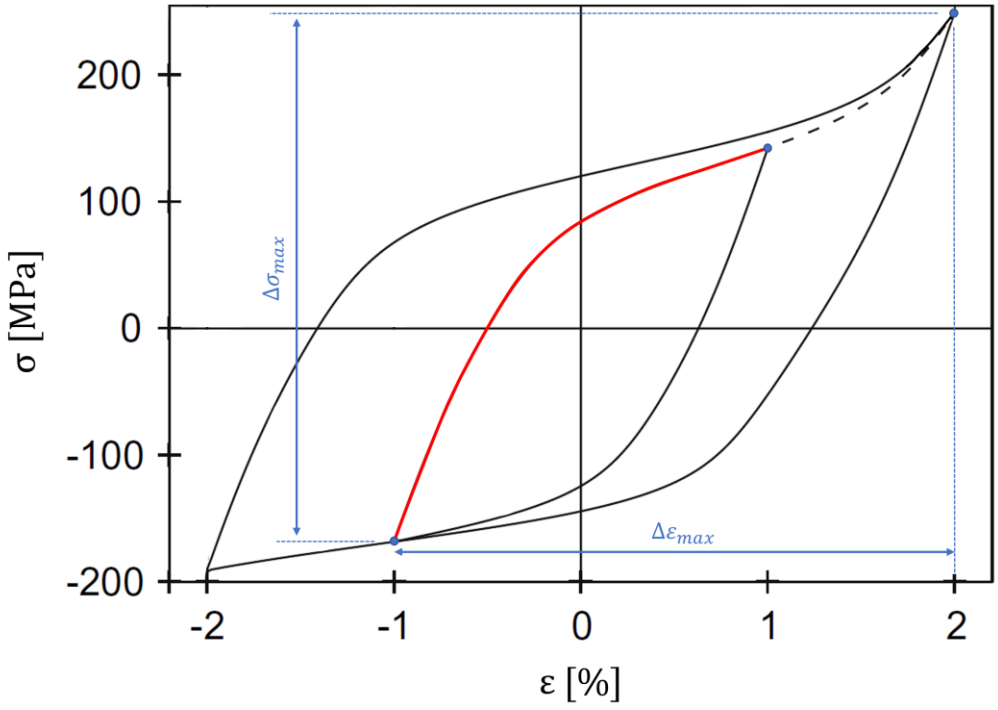

Figure 7. Determination of m_{pl} and m_{psel} values when the current reversal deviating from the envelope hysteresis loop (The stress-strain curve shown in red) [5]

The stress range is not readily available for the stress-strain curve shown in red. However, it is known that, by virtually extending the stress-strain curve towards the top-right corner, the loop will be closed and the material memory will be full-filled when it reaches 2% of strain. Furthermore, the global stress and strain values at -1% of strain and 2% are known from the previous calculations at this point. Therefore, instead of finding the stress range corresponds to the red stress-strain curve which is not available at this moment, the stress and strain range of the -1% to 2% hysteresis loop ($\Delta\sigma_{max}$ and $\Delta\varepsilon_{max}$) is taken to calculate the corresponding m_{pl} & m_{psel} values. Finally, the established relative stress and strain relation for the upward -1% to 2% then can be trimmed down and only the portion from -1% to 1% is taken.

The validations of the model on AM50 for stabilized constant and variable amplitudes by Dallmeier, J et al. [5] are shown in Figure 8:

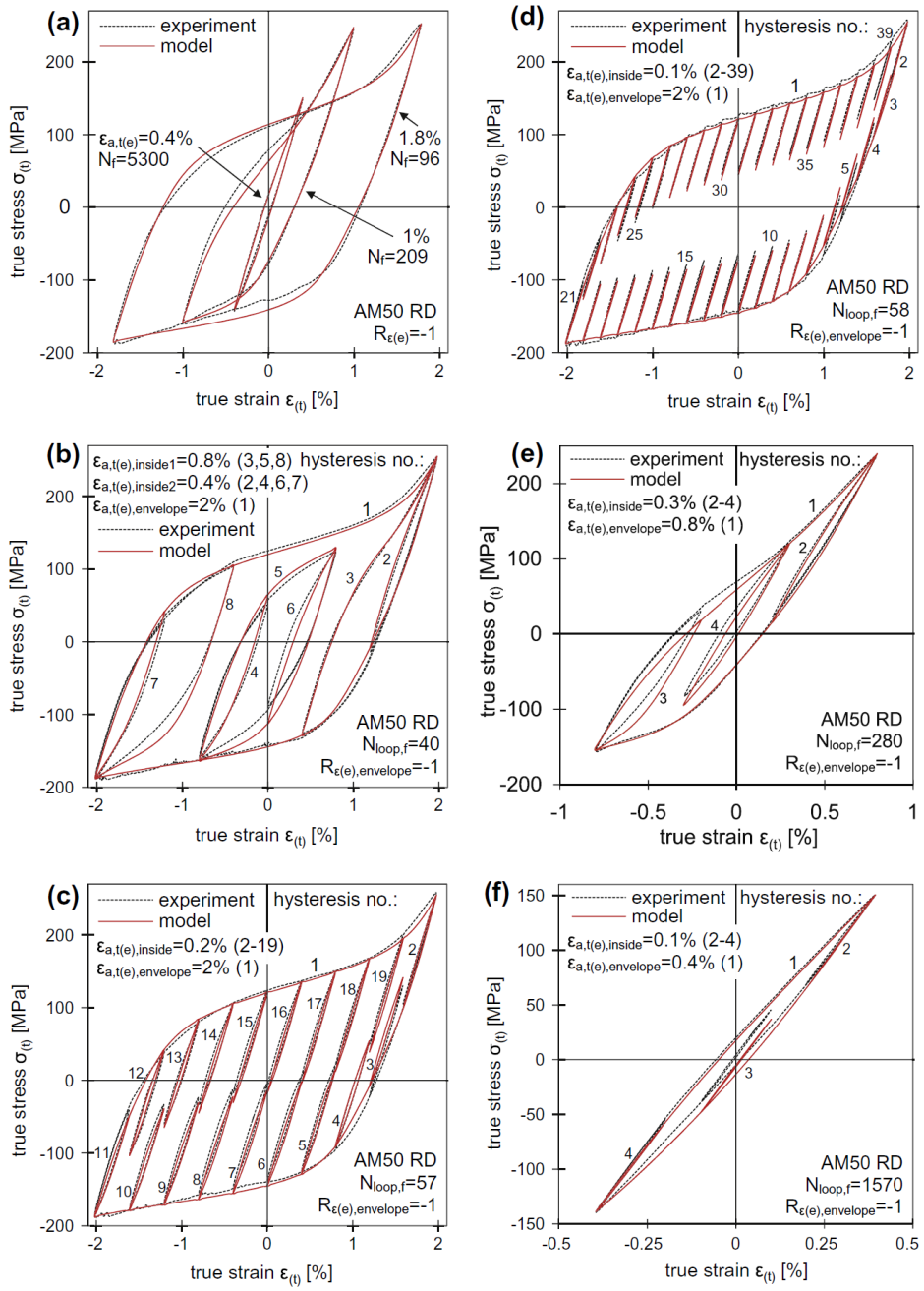

Figure 8. Validations of the model on AM50 for constant and variable amplitudes by Dallmeier, J et al. [5]

A good agreement between the phenomenological model and experimental results can be found across the board on AM50.

To be able to properly design and evaluate the fatigue lives of load bearing components using magnesium alloys, the effects of the stress concentrations (holes, keyways, etc.) to the localized stress-

strain responses under monotonic or cyclic loading need to be investigated, since the failure of components usually initiates at these points.

It would be straightforward if the local stress-strain responses at the notch root are purely elastic. In this case, the local stresses and strains can be directly evaluated using the theoretical elastic stress concentration factor (K_t):

$$\frac{\sigma}{S} = \frac{\varepsilon}{e} = K_t \tag{10}$$

Where σ is the local stress and ε is the local strain at the notch root; S is the nominal stress and e is the nominal strain away from the notch.

However, the existing stress concentrations may induce localized plastic yielding despite the nominal stresses applied are well below the yield limit. The elastoplastic analysis is needed to determine the non-linear stress-strain responses at the notch root by the far-field stresses. The elastoplastic stress and strain fields can be assessed by using non-linear finite element method. However, these types of numerical simulations are usually very expensive and time-consuming especially when fatigue life assessment is concerned, while components are subjected to arbitrary load histories. Neuber proposed an analytical method in 1968 to approximate the stresses and strains at the notch root based on the study of prismatic bodies with hyperbolic notches under out-of-plane steer, and it is later known as the Neuber's rule [75] . The Neuber's rule stated that, the geometrical mean of stress concentration factor (K_σ) and strain concentration factor (K_ε) is equal to the theoretical elastic stress concentration factor (K_t):

$$K_t = \sqrt{K_\sigma K_\varepsilon} \tag{11}$$

$$K_\sigma = \frac{\sigma}{S} \tag{12}$$

$$K_\varepsilon = \frac{\varepsilon}{e} \tag{13}$$

$$e = \frac{S}{E} \tag{14}$$

By substitute Equation (12-14) into Equation (11) and re-arrange:

$$\sigma\varepsilon = \frac{(SK_t)^2}{E} \tag{15}$$

Equation (15) is often referred to as the Neuber's hyperbola. Since there are two unknowns in this Equation (ε and σ), another relation between the local stress and strain at the notch root is also needed, which is given by the stress-strain curve.

As an example, as seen in Figure 9, the plate with a circular notch in the middle is under uniaxial nominal stress (S) and the stress-strain curve at the notch root in the y-direction is given as a Ramberg-Osgood equation as shown in Equation (16):

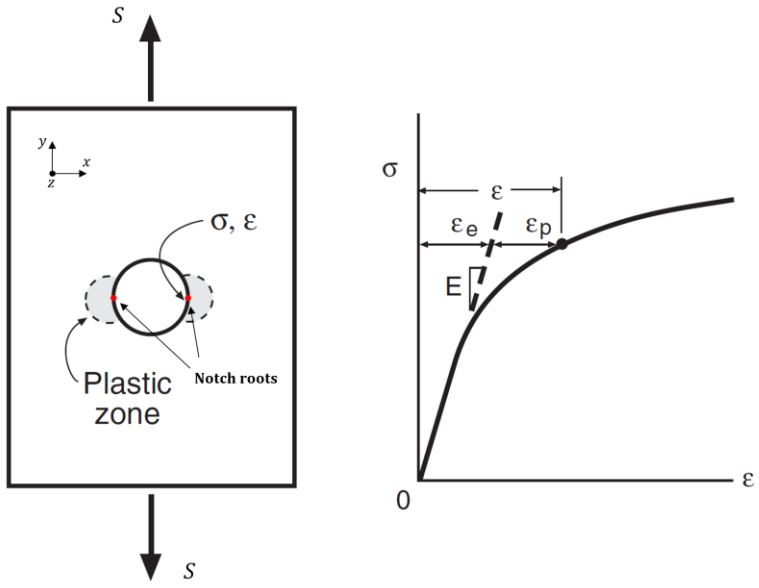

Figure 9. Circular notch under uniaxial tensile load with Ramberg-Osgood stress-strain curve example [6]

$$\varepsilon = \frac{\sigma}{E} + \left(\frac{\sigma}{K}\right)^{1/n} \tag{16}$$

Where K is the monotonic strength coefficient and n is the monotonic strain hardening exponent. By Neuber's rule, the stress (σ) and strain (ε) at the notch root under the applied nominal stress S can be calculated by solving Equation (17):

$$\begin{cases} \sigma\varepsilon = \frac{(SK_t)^2}{E} \\ \varepsilon = \frac{\sigma}{E} + \left(\frac{\sigma}{K}\right)^{1/n} \end{cases} \tag{17}$$

And a graphical illustration is shown in Figure 10:

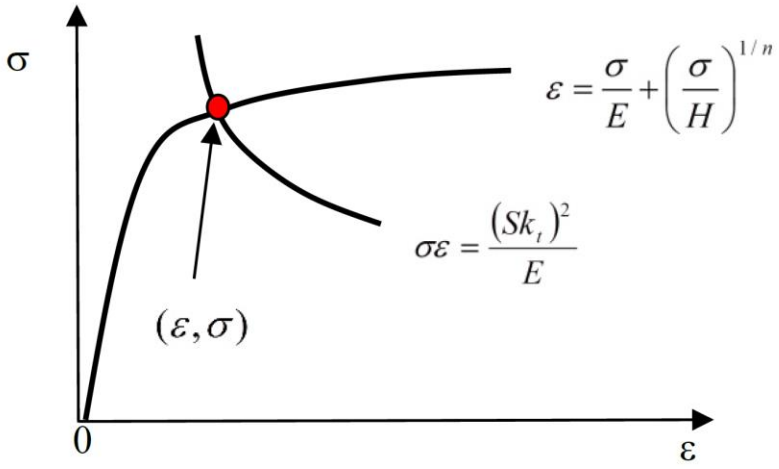

Figure 10. Graphical illustration of Neuber's rule [76]

Although the original Neuber's rule is valid only for uniaxial situations, T. Seeger and M. Hoffmann extended the Neuber's rule to multiaxial stress states in case of proportional loading by replacing an equivalent nominal stress equal to the reference stress [77] . Seeger et al. extended the application of Neuber's rule beyond the general yielding of the material [78] . Topper, T et al. extended the Neuber's rule for cyclic loading scenarios by replacing the nominal stress (S) and strain (e) with the nominal stress (ΔS) and strain ranges (Δe), at the same time replacing the notch stress (σ) and strain (ε) with the notch stress ($\Delta\sigma$) and strain ($\Delta\varepsilon$) ranges. In addition to that, the authors also proposed to replace the theoretic stress concentration factor (K_t) with the fatigue notch factor (K_f) to improve fatigue life predictions and to take the effect of the stress gradient into consideration [79] . However, it has been criticized for re-accounting the notch root plasticity effects [80] .

As an alternative approach to the Neuber's rule, Molski and Glinka proposed the equivalent strain energy density method (ESED), later known as the Glinka's rule. It was derived upon the hypothesis that, the localized plastic zone at the vicinity of the notch root is controlled by the surrounding elastic stress field. The Glinka's rule stated that, in the presence of localized small-scale plastic yielding, the gross linear elastic behavior of the material surrounding the notch also controls the deformations in the plastic zone, thus, the energy density W_σ in the plastic zone is equal to that calculated on the basis of the elastic solution (W_S) [81] :

$$W_\sigma = W_S \tag{18}$$

$$W_\sigma = \int_0^{\Delta e_{ij}} \Delta S_{ij}\, d\Delta e_{ij} = \frac{(K_t S)^2}{2E} \tag{19}$$

$$W_S = \int_0^{\Delta \varepsilon_{ij}} \Delta \sigma_{ij}\, d\Delta \varepsilon_{ij} \tag{20}$$

A graphical illustration of Glinka's rule is shown in Figure 11:

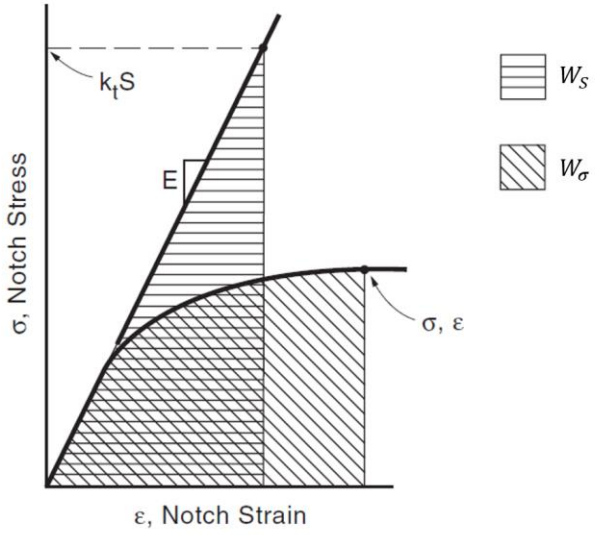

Figure 11. Graphical illustration of Glinka's rule (ESED) [6]

Later in 1986, Glinka proposed the strain energy density correction factor (C_p) to take the stress re-distribution due to plastic yielding at the vicinity of the notch root into consideration to improve the prediction for ESED [82] .

The derivation of the C_p factor is based on the fact that; the actual stresses is lower than those derived from the linear elastic analysis within the plastic zone at the vicinity of the notch root when localized yielding occurs. However, the equilibrium condition still holds for the notched body and a stress re-distribution occurs in the neighbourhood of the notch tip resulting in an increase of the plastic zone size as shown in Figure 12 [82] .

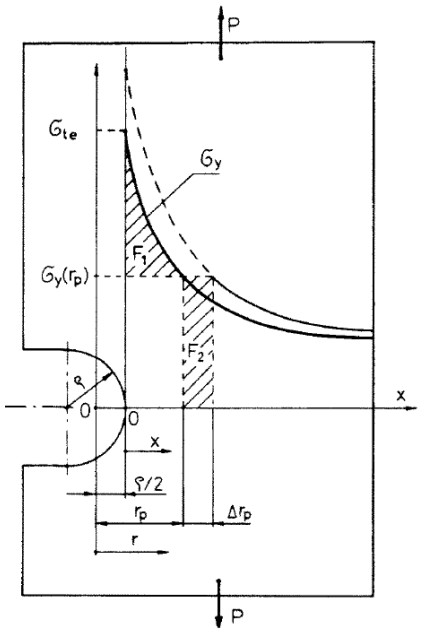

Figure 12. Plastic yielding and the elastic stress redistribution ahead of a notch tip [82] .

Due to plastic yielding, the amount of force F_1 cannot be carried through by the material inside the plastic zone r_p. In order to satisfy the equilibrium condition, the amount of force has to be carried by the material beyond the initially determined plastic zone (r_p) by an increment of Δr_p in which $F_1 = F_2$ [82] . The first approximation of the plastic zone size ahead of the notch root (r_p) for uniaxial tension or compression is given by Equation (21):

$$\sigma_y = \frac{k_t S}{2\sqrt{2}}\left[\frac{\rho}{r_p} + \frac{3}{4}\left(\frac{\rho}{r_p}\right)^3\right]^{1/2} \tag{21}$$

Where σ_y is the yield stress, ρ is the notch radius and S is the applied nominal stress.

The C_p correction factor for uniaxial tension or compression is given in Equation (22):

$$C_p = 1 + \left(\rho/r_p\right)\left[\frac{2\left(r_p/\rho\right)^{1/2} - \left(\rho/r_p\right)^{1/2}}{\left(\rho/r_p\right)^{1/2} + \frac{1}{2}\left(\rho/r_p\right)^{3/2}} - \left(\frac{r_p}{\rho} - \frac{1}{2}\right)\right] \tag{22}$$

$$W_\sigma = C_p W_S \tag{23}$$

Where the C_p factor directly applied to the energy density on the basis of the linear elastic solution in Equation (23).

A study by Kilambi and Tipton has shown that the Neuber's rule relies on the material constitutive relation and the model of loading while the Glinka's rule is limited to a small plastic zone ahead of the notch root surrounded by predominantly elastically deformed material [83] . A comparison between the Neuber's and Glinka's prediction is shown in Figure 13:

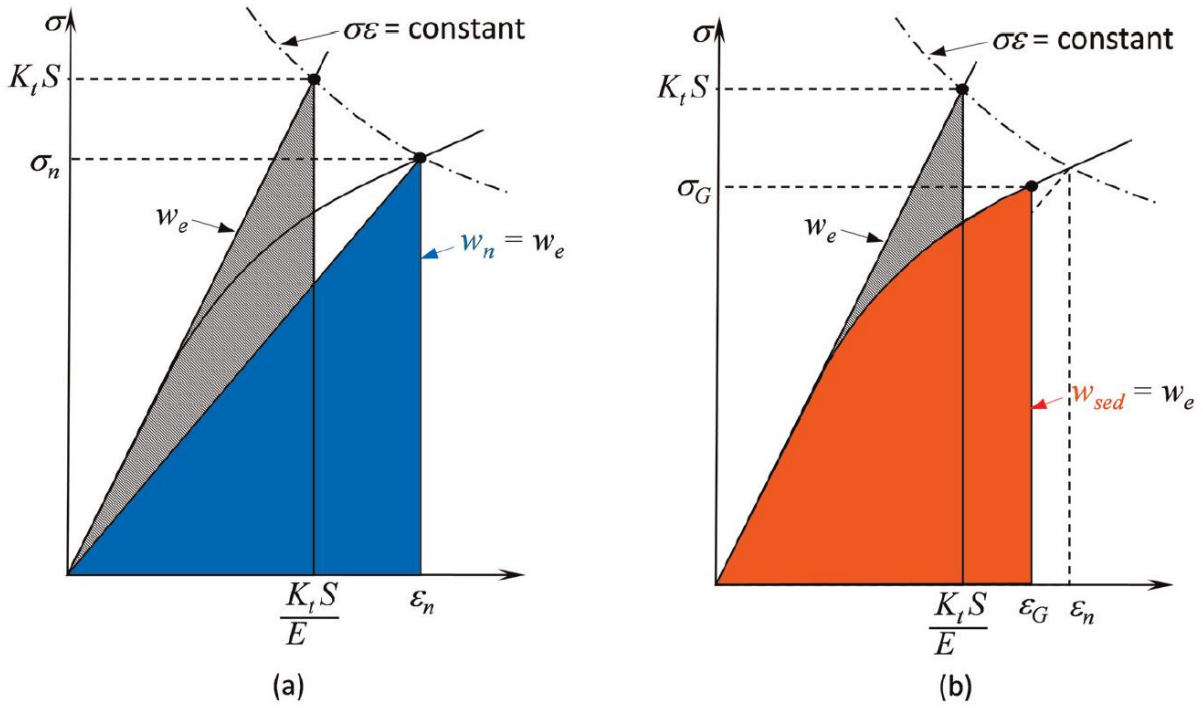

Figure 13. Comparison between the prediction using (a) Neuber's and (b) Glinka's (ESED) [83]

It can be seen that, both Neuber's and Glinka's (ESED) methods are energy based. The Neuber's rule sets the strain energy density within the blue triangle area equal to the strain energy density determined on the basis of the elastic solution while Glinka's rule sets the actual elastoplastic strain energy density equal to the strain energy density determined on the basis of the elastic solution. Moftakhar et al. suggested that, the generalized Neuber's rule, which represents the equality of the total strain energy

density at the notch tip gives an upper bound estimation for the elastoplastic notch tip stresses and strains while the Glinka's rule (ESED) serves as the lower bound of the stresses and strains prediction [84] . A thermodynamic analysis has been carried out by Ye, D et al. [85] -[86] further support that, the Neuber's rule prediction serves as the upper bound whereas Glinka's (ESED) prediction serves as the lower bound. In addition, the thermodynamic linkage between Neuber's rule and Glinka's rule has been revealed. The authors stated that, For Glinka's rule, the theoretical work applied to the material at the notch root due to the nominal remote stress is transformed into the real total strain energy absorbed by the material and the heat dissipated at the notch root due to plastic deformation. The Neuber's rule, on the other hand, is a particular case of Glinka's rule (ESED), while the heat dissipation due to plastic deformation at the vicinity of the notch root is neglected [85] . Therefore, Glinka's rule tends to underpredict the notch stress (σ) and notch strain (ε) based on the assumption that all the energy contribute to plastic deformation at the vicinity of notch root is fully converted to heat. In contrast, Neuber's rule serves as another extreme that, assuming no heat dissipation due to plastic deformation at the vicinity of the notch root. Since heat dissipation during the plastic yielding is inevitable, as a result, Neuber's rule will always overestimate the local stresses (σ) and strains (ε).

Chapter 3: Experimental Work

3.1. Material identification

3.1.1 Initial microstructure

The material investigated in this study is rolled and annealed ZEK100 magnesium alloy sheet with a thickness of 6.6 mm. The initial microstructure by optical micrographs on a virgin sample in all three planes (ND-RD, ND-TD, and RD-TD) are shown in Figure 14:

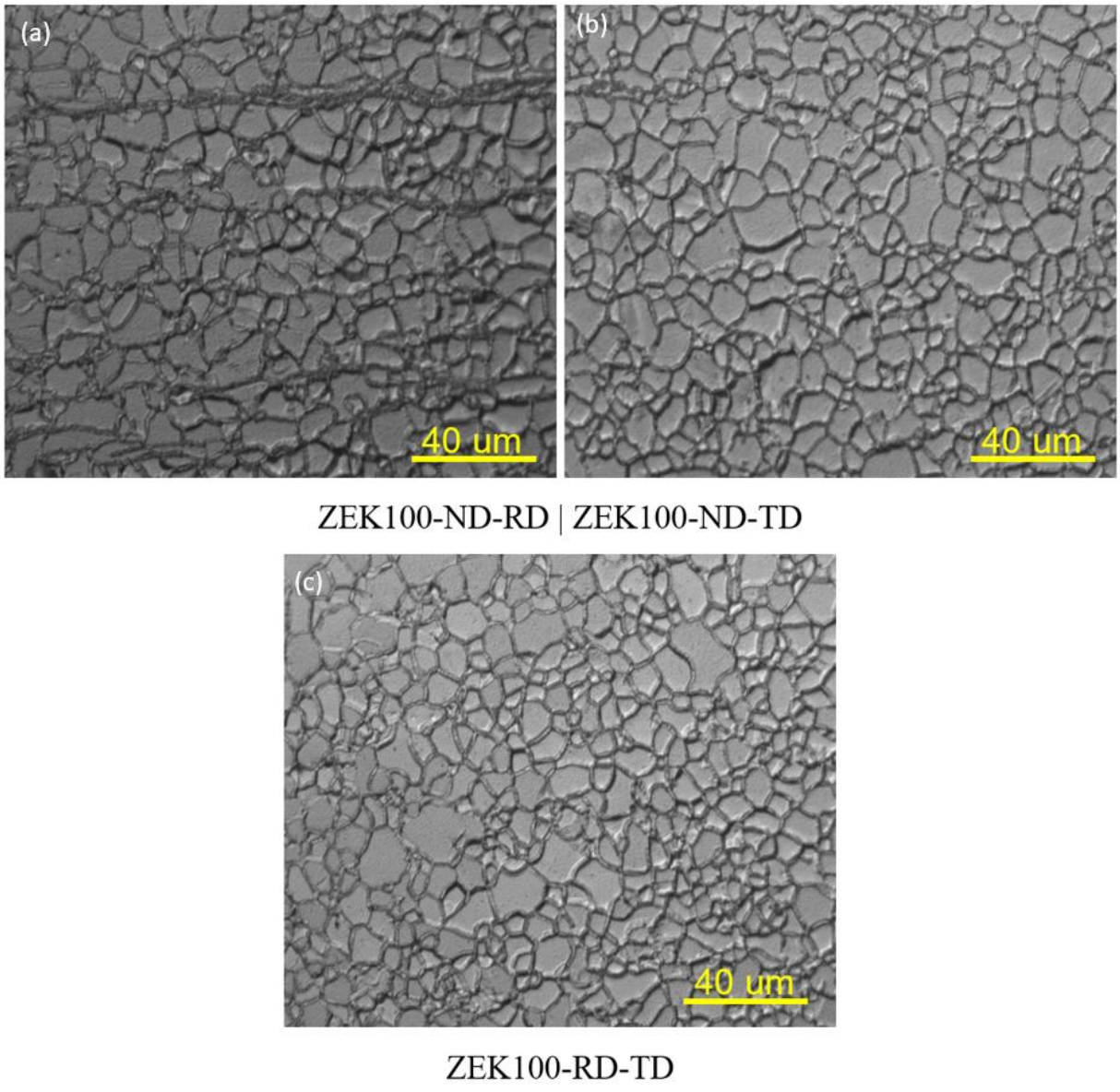

Figure 14. Optical micrographs of the ZEK100-O magnesium alloy in (a). ND-RD plane (b). ND-TD plane (c). RD-TD plane

No significant distinction is observed among the micrographs in all three planes and it is also observed that the microstructure is free of twinning. The average grain size determined by the average grain intercept method is 7.2 μm.

3.1.2 Initial texture

The (0002) and $(10\bar{1}0)$ pole figures for ZEK100-O are shown in Figure 15:

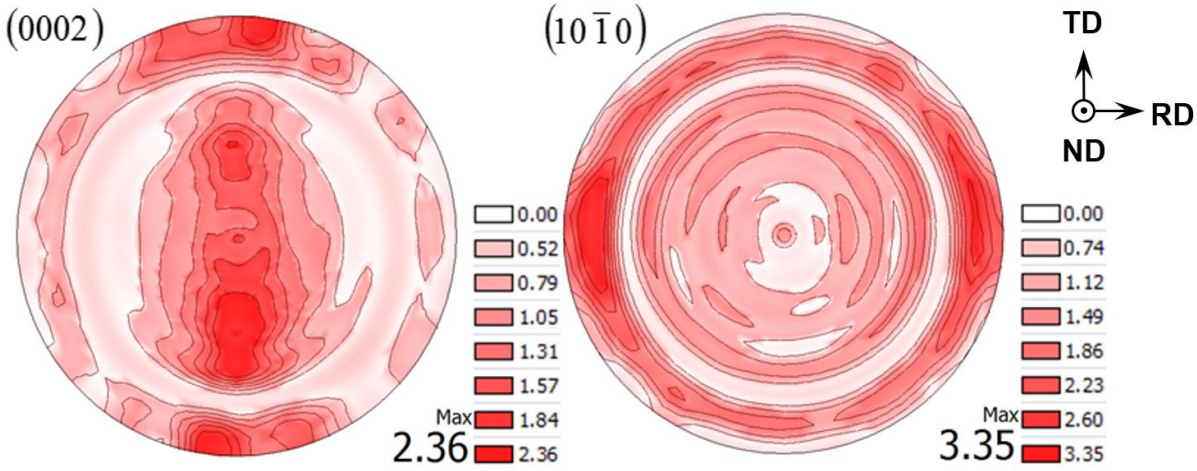

Figure 15. (0002) *and* $(10\bar{1}0)$ *pole figures for ZEK100-O magnesium alloy*

As seen in the pole figure, the majority of the basal poles (0002) are scattered within an angle of around 30 degrees in the normal direction, which is in agreement with the literature [4] [22] [30] [31] . As suggested in the literature, this is the result of the neodymium atoms segregate to the grain boundaries and affect the grain boundary motion, which alters the recrystallization and grain growth. The solute clusters cause strain heterogeneity and influence the nucleation and growth process of recrystallization [58] . Due to the relatively weaker texture of ZEK100-O, less tension-compression asymmetry can be expected. In addition, the spread of basal poles in the transverse direction (TD) promotes a higher level of planar anisotropy.

3.2. Quasi-static tensile properties

3.2.1 Specimen geometry

The quasi-static behaviors of ZEK100-O in tensile are evaluated in the rolling direction of the material. The specimen geometry for the tension tests is shown in Figure 16:

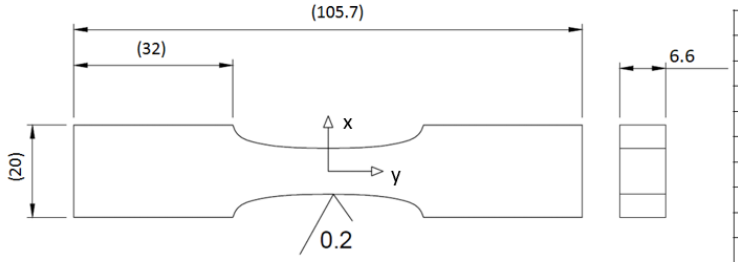

y (mm)	x (mm)	y (mm)	x (mm)
0.00	5.00	13.95	5.81
1.14	5.00	15.23	6.05
2.28	5.01	16.53	6.35
3.42	5.02	17.80	6.74
4.56	5.04	18.91	7.28
5.70	5.07	19.60	7.84
6.85	5.11	20.00	8.29
8.00	5.17	20.40	8.89
9.15	5.25	20.85	10.00
10.33	5.33	52.85	10.00
11.51	5.45	52.85	0.00
12.72	5.61		

Figure 16. Design of smooth specimen. This design was created at FATSLAB. One of its features is an improved chance of crack formation near centre of specimen vs specimens with a rectangular reduced section.

The curved gage length improves the chance of the crack formation close to the center, yet, the slight stress concentration will not affect the uniformity of stress distribution across the cross-section area, as shown in Figure 17:

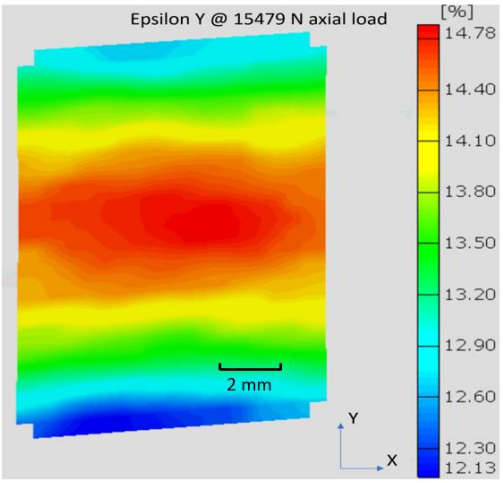

Figure 17. Axial strain field under quasi-static tension- ZEK100 (The strain field is captured using DIC and processed with the ARAMIS software).

3.2.2 Quasi-static tension tests setup

The monotonic tensile tests were conducted using the smooth specimens in which the y-direction shown in Fig. 2 is aligned with the test direction of the material. DIC was used to capture the strain field in the middle section as shown:

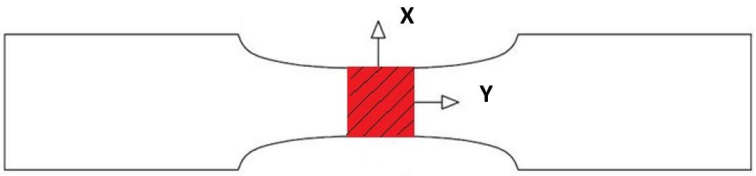

Figure 18. DIC field of view (Shaded area has been chosen inside the ARAMIS software for the properties calculations).

As shown in Figure 18, the strain field within the shaded area (10 mm × 10 mm) is used to calculate the properties of the material. Two more repetitions were done to confirm the results and the properties for ZEK100 is taken as the average of these three tests.

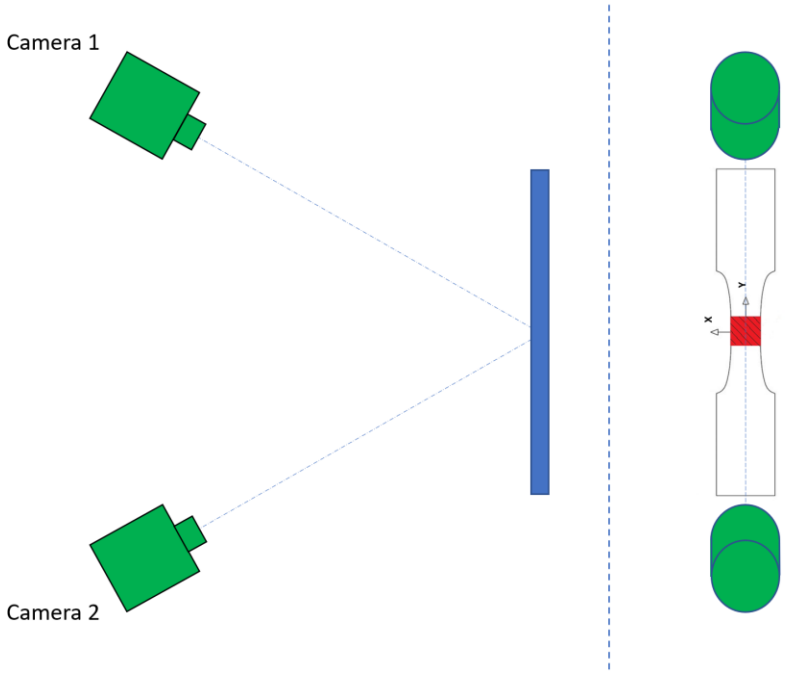

Figure 19. Quasi-static tension test DIC camera setup.

The camera setup for the monotonic tensile tests is shown in Figure 19, where both the cameras are enabled. The cameras are placed in the plane of symmetry (y-z plane) and focused at the middle section

of the test specimen where the distance between the sample and each camera is approximately the same. A picture of the test setup is also shown in Figure 20.

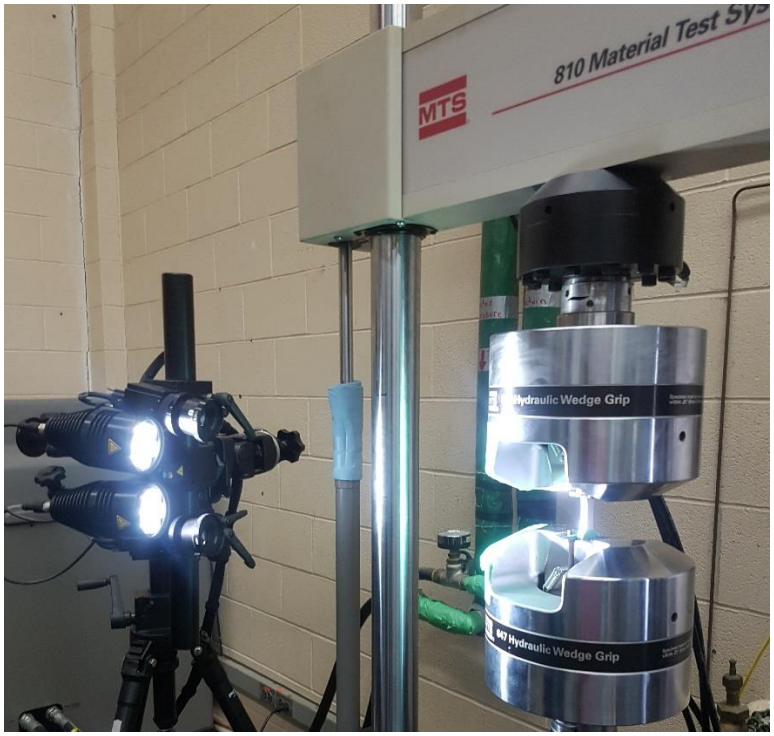

Figure 20. Quasi-static tension test setup.

3.2.3 Quasi-static tension test results

Three tests have been done to obtain the properties of ZEK100 in the rolling direction and the quasi-static stress-strain (engineering) curve is shown in Figure 21. Severe necking is observed after reaching the ultimate tensile strength and the final fracture is in a ductile manner. A picture of the sample after the final failure is shown in Figure 22.

The Quasi-static properties are calculated inside the ARAMIS software and a plot of the average axial strain (Epsilon Y (Area (large)) (Average)) within the shaded area in the longitudinal direction (loading direction) for ZEK100 is shown in Figure 23. The red curve is a linear fit within the first few data points below 50 MPa for the E- modulus calculation and the green curve is originated from 0.2% of strain on the horizontal axis and parallel to the red line for the 0.2% offset yield strength calculation.

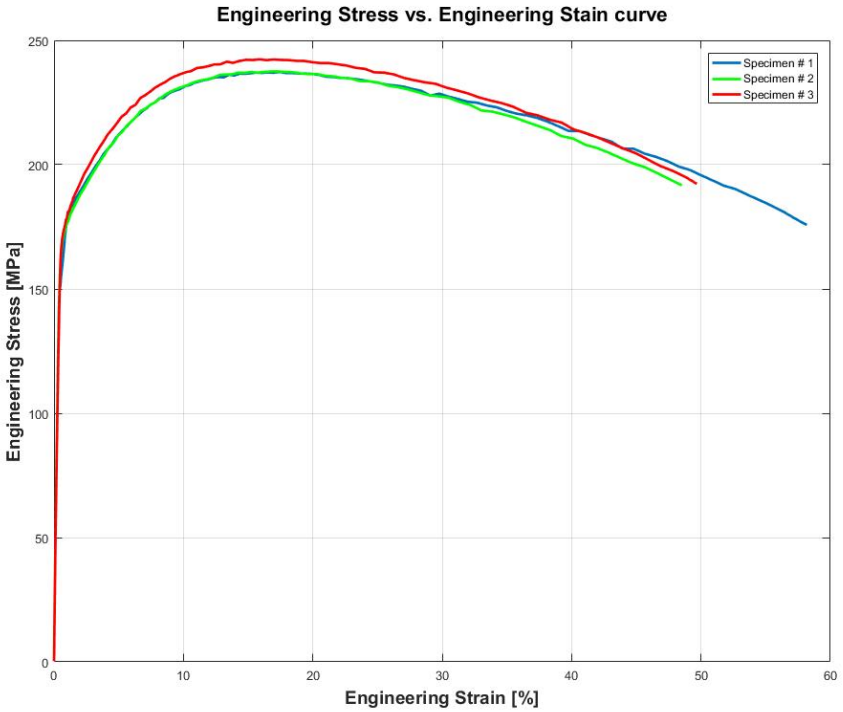

Figure 21. Tensile engineering stress vs. strain curves for all three tests (ZEK100).

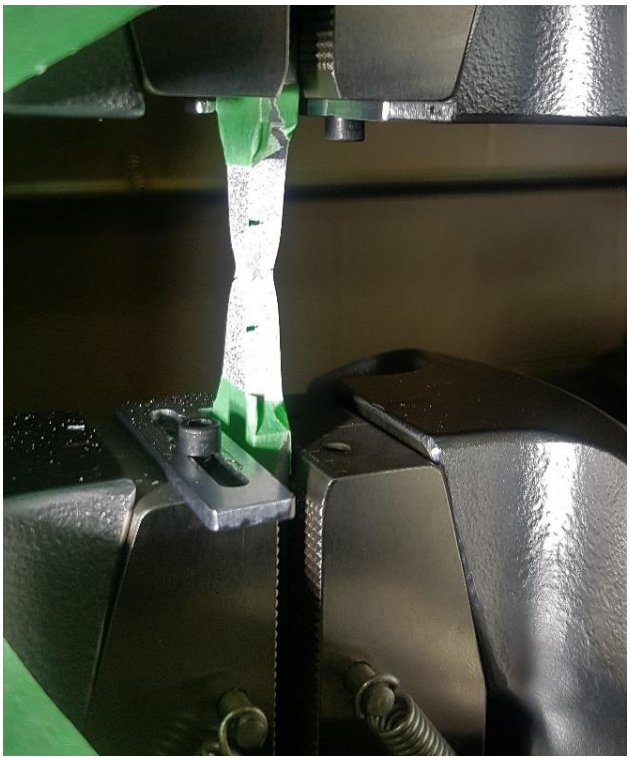

Figure 22. Quasi-static tensile test sample showing the necking- ZEK100-O.

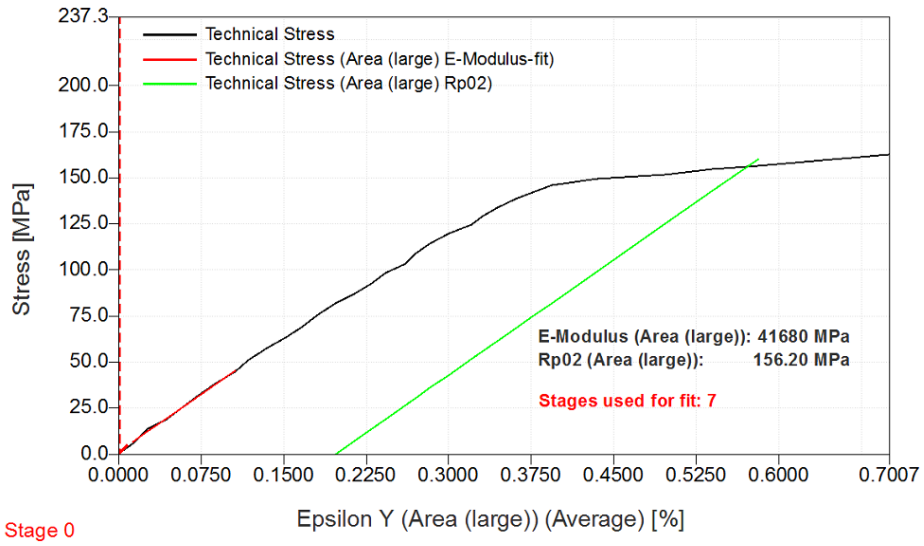

Figure 23. Initial portion of engineering Stress vs. strain curve of ZEK100 to calculate elastic modulus and 0.2% offset yield stress.

The tensile properties calculated for ZEK100 in the rolling direction is summarized in Table 4:

		Specimen #1	Specimen #2	Specimen #3	Average Value	Sample Standard Deviation
E, Modulus [GPa]		41.68	42.56	44.85	43.03	1.64
UTS [MPa]	**Engineering**	237.33	237.52	242.38	239.08	2.86
	True	287.71	277.45	280.84	282.00	5.23
TYS (0.2% offset) [MPa]		156.20	166.39	167.52	163.37	6.24
Uniform Elongation [%]		16.87	16.25	15.33	16.15	0.78
Reduction in Area (RA) [%]		56.56	54.48	56.06	55.70	1.09
True Fracture Strain (ln(1/(1-RA))) [%]		87.08	85.68	89.43	87.40	1.90

Table 4. ZEK100 monotonic tension material properties

Notice that the true fracture strain is about 87.4%, which translate to a very high ductility of this material. As suggested in the literature, this is the result of the weakened basal texture due to the addition of the rare-earth element neodymium [30] -[32] .

3.3. Quasi-static compression properties

2.3.1 Specimen geometry

The quasi-static compression tests have been done with cubic specimens to prevent buckling and the geometry of the compression sample is shown in Figure 24:

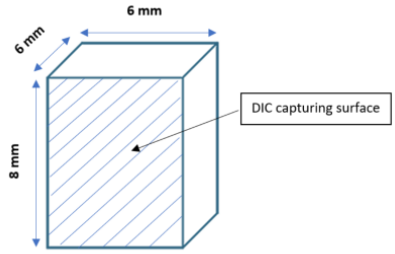

Figure 24. Compression test specimen geometry.

The compression test specimens are well-machined to a dimension of 8mm × 6mm × 6mm and the angle between each side is precisely machined to 90 degrees to ensure the best accuracy. One side of the specimen is painted with the speckle patterns for the DIC to capture the strain field within that area.

3.3.2 Quasi-static compression tests setup

The setup for the quasi-static compression tests is shown in Figure 25, a single camera with extension tube has been used to capture the strain field on one side of the compression sample. The camera is perpendicular to the face of the sample where the speckle pattern was painted.

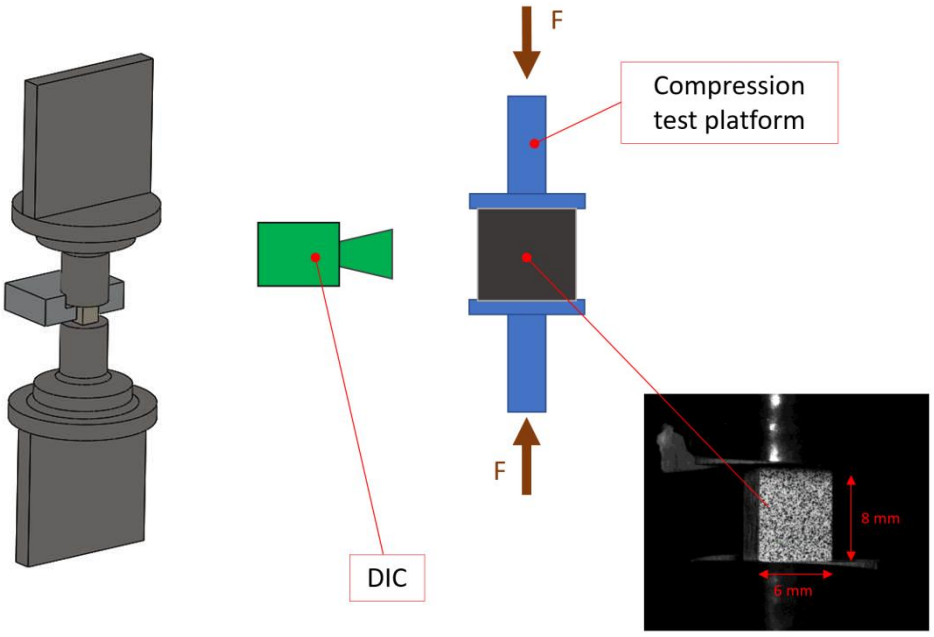

Figure 25. Monotonic compression test setup.

The cubic samples were placed at the center of the compression test platform where the axial compression force is applied. The properties were evaluated by averaging the strain across a small section located at the center of the speckle pattern shown in Figure 26:

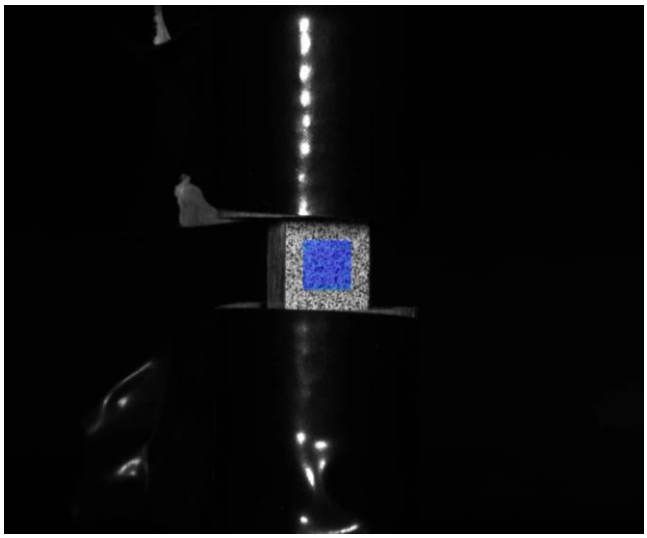

Figure 26 Compression setup view from DIC.

3.3.3 Quasi-static compression test results

The blue area on top of the speckle pattern is selected inside the ARAMIS software where the properties are evaluated. Two samples were tested in each direction to confirm the results and the stress-strain curves for both rolling and transverse directions are shown in Figure 27, TD and RD represent transverse and rolling directions, respectively:

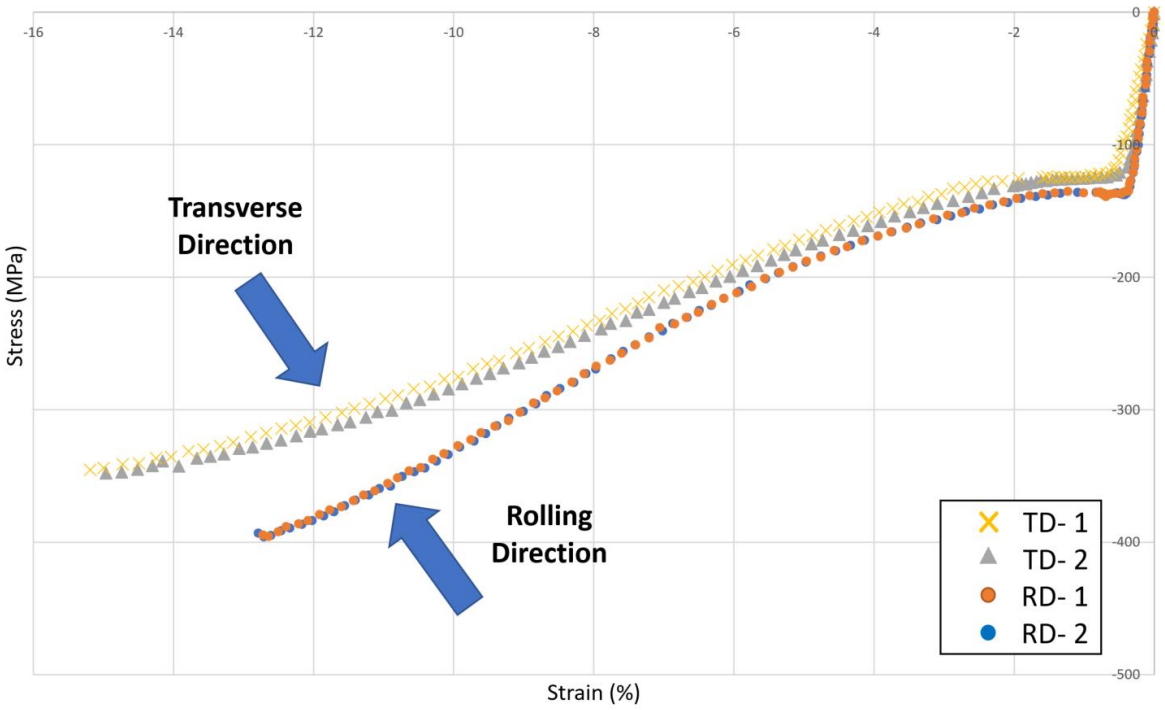

Figure 27. Monotonic stress-strain curves of ZEK100 in uniaxial compression in rolling, and transverse directions.

All the curves terminate at the stress right before the sample fails. It is apparent that the property in transverse and rolling directions are different and ZEK100 is slightly stronger in rolling direction due to the presence of anisotropy of the material. Here is a comparison between the monotonic tensile and compressive stress-strain curves in a different direction:

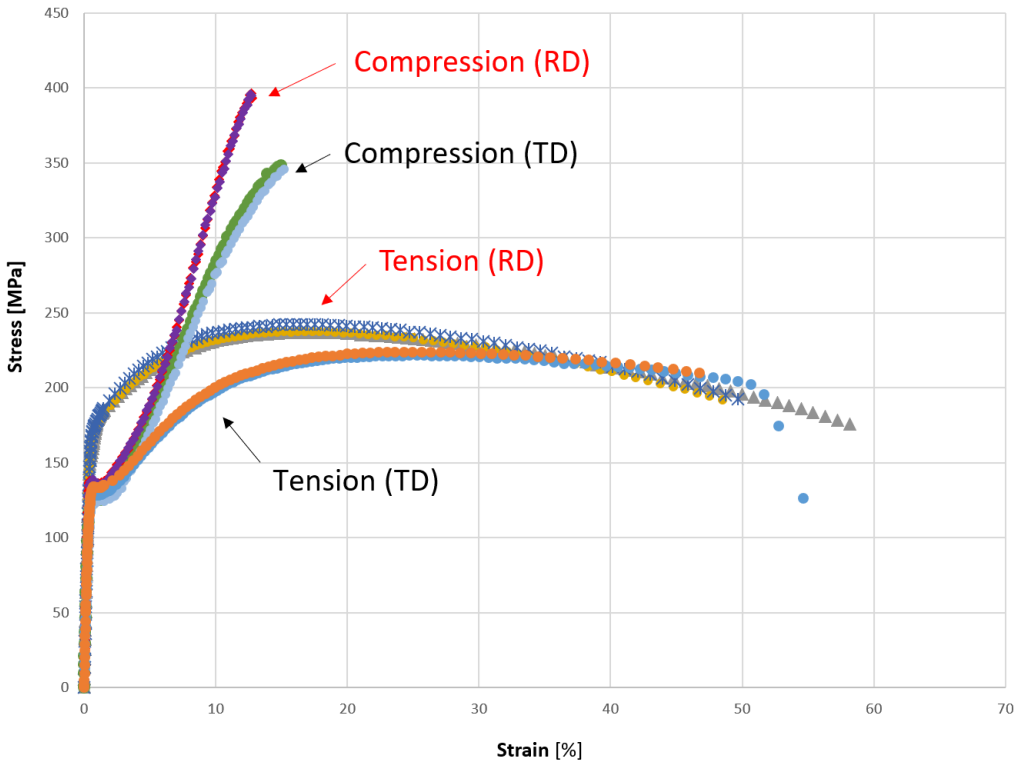

Figure 28 Comparison between monotonic tensile and compressive flow curves of ZEK100.

The compressive properties in both rolling and transverse direction is summarized in Table 5:

	Rolling Direction	Transverse Direction
Yield strength (0.2% offset)	-136.9 MPa	-122.5 MPa
Ultimate compressive strength	-396.0 MPa	-352.2 MPa
Ultimate compressive strain	12.68 %	16.1 %

Table 5. ZEK100 monotonic compression material properties

It can be observed that the tensile yield strength is higher than compressive yield strength in the rolling direction. However, the ultimate compressive strength is much higher compared with the ultimate tensile strength. A picture of the fractured specimen is shown in Figure 29:

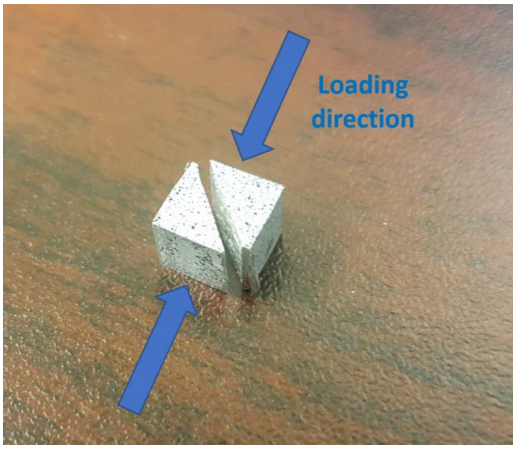

Figure 29. Fractured quasi-static compression specimen.

Noticed that a 45-degree fracture surface is observed on every single sample for ZEK100, where the shear stress is at its maximum.

3.4. Cyclic properties

3.4.1 Specimen geometry and test setup

The specimens used for the cyclic properties' characterization is exactly the same as what has been used in the quasi-static tensile characterization as shown in Figure 16. However, instead of the speckle pattern, a 10mm width gauge length is pre-marked to mount the extensometer precisely in the middle, shown in Figure 30:

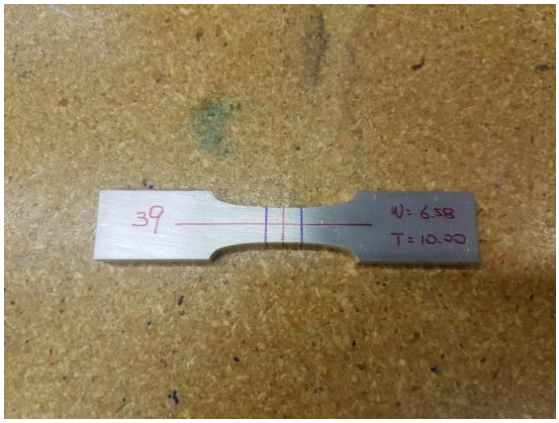

Figure 30. Smooth cyclic test sample (the marked blue lines are where the extensometer knife edges are contacting the specimen)

As illustrated in Figure 31, the extensometer is mounted in the mid-section of the sample with a gauge length of 10 mm. The extensometer was mounted on the bare sample with adhesive or on top of a thin layer of acrylic coating held by rubber bands.

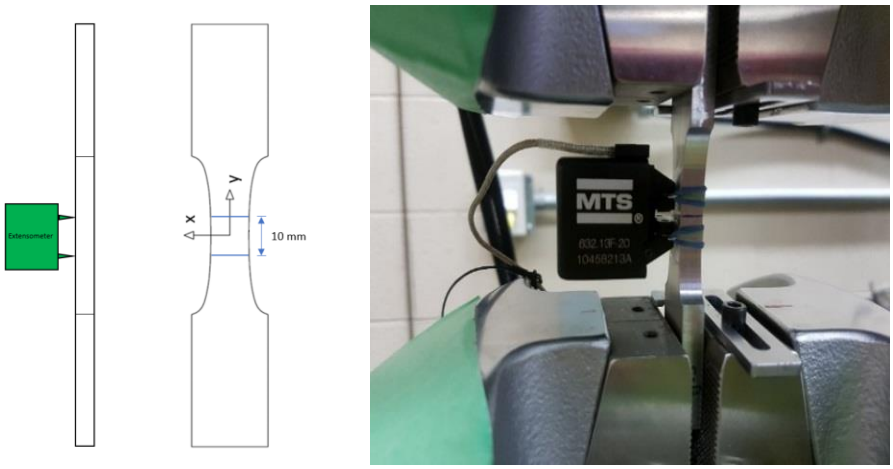

Figure 31. Strain-controlled test setup for Cyclic properties characterization

The failure criteria for all the tests are either 15% load drop or final fracture if the test was switched to load control. The crack or final fracture has to be within the extensometer gauge length to be considered as a valid test.

3.4.2 Constant amplitude fully-reversed (R_ε=-1) and strain-controlled cyclic results

Fully reversed strain-controlled tests were conducted on ZEK100 in the rolling direction for various strain amplitude from 0.3% to 2.3%. The second-cycle hysteresis loops for various strain amplitudes are shown in Figure 32 and the stabilized stress-strain hysteresis loops are shown in Figure 33.The comparisons of the second-cycle and stabilized stress-strain hysteresis loops for each applied strain amplitude from 0.3% to 2.3% are shown in Figure 34 to Figure 42.

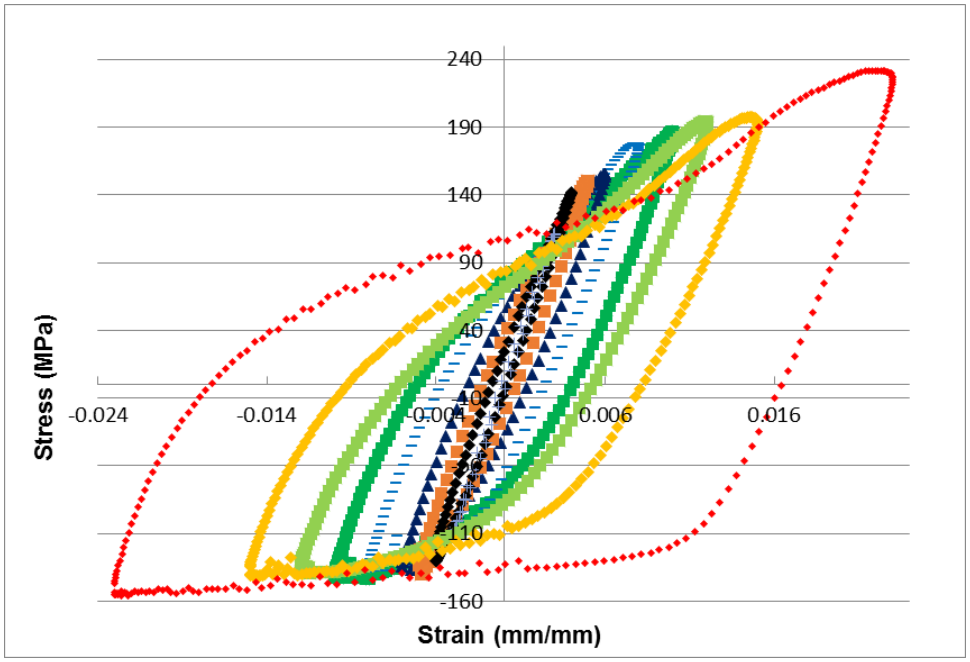

Figure 32 Second-cycle hysteresis loops of ZEK100-O.

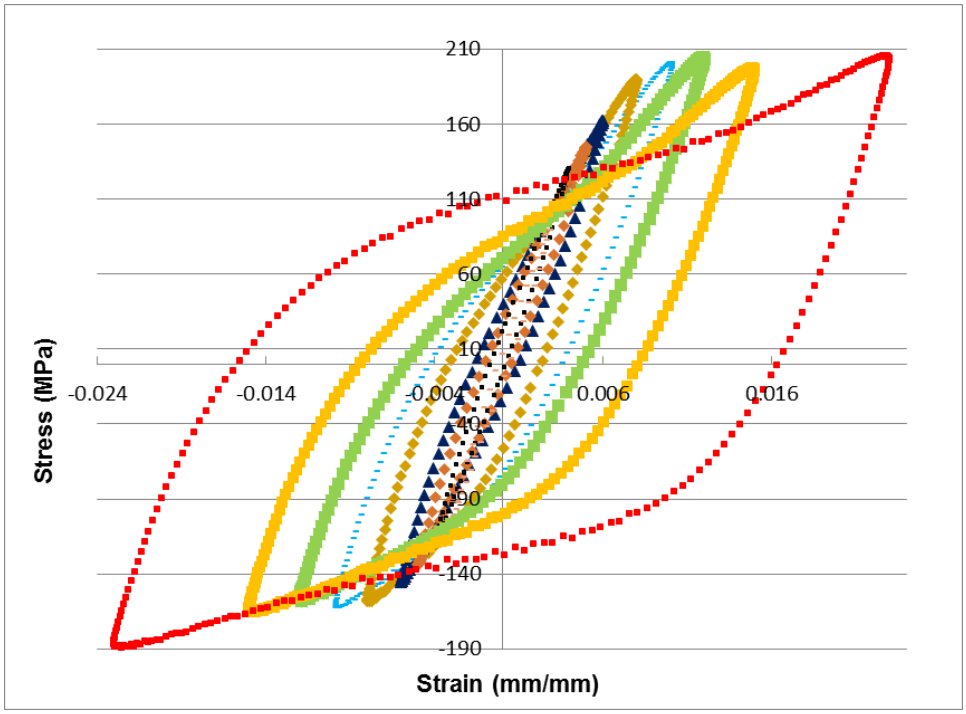

Figure 33. Half-life hysteresis loops of ZEK100-O.

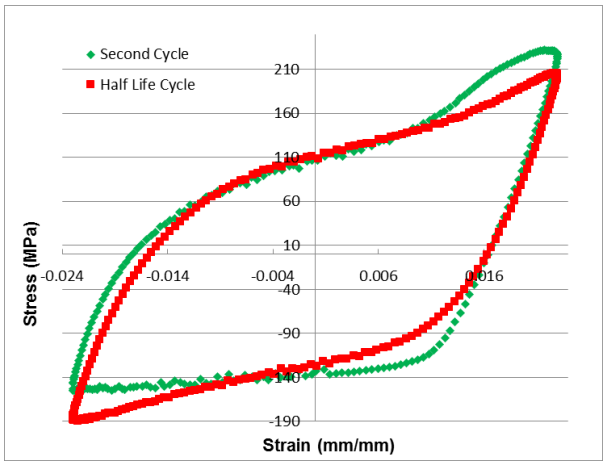

Figure 34 Second cycle and stabilized stress-strain hysteresis at 2.3% strain amplitude (ZEK100).

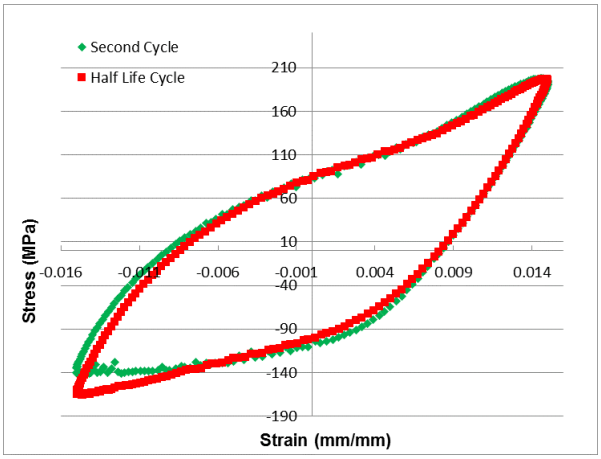

Figure 35 Second cycle and stabilized stress-strain hysteresis at 1.5% strain amplitude (ZEK100)

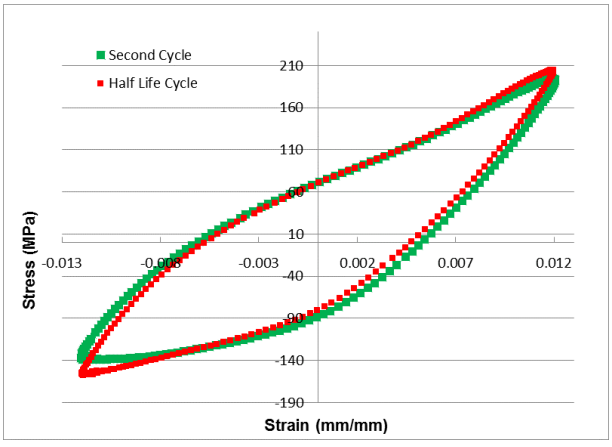

Figure 36 Second cycle and stabilized stress-strain hysteresis at 1.2% strain amplitude (ZEK100).

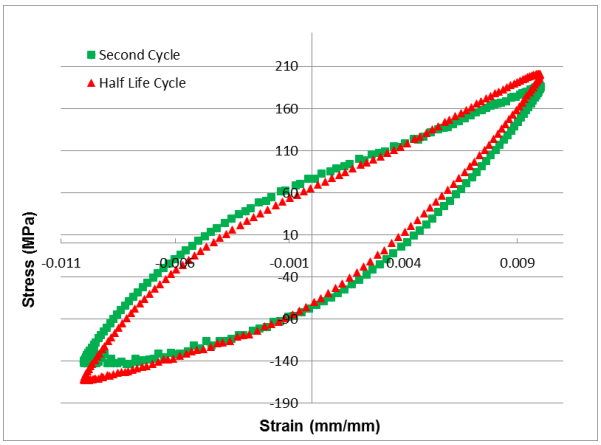

Figure 37 Second cycle and stabilized stress-strain hysteresis at 1.0% strain amplitude (ZEK100).

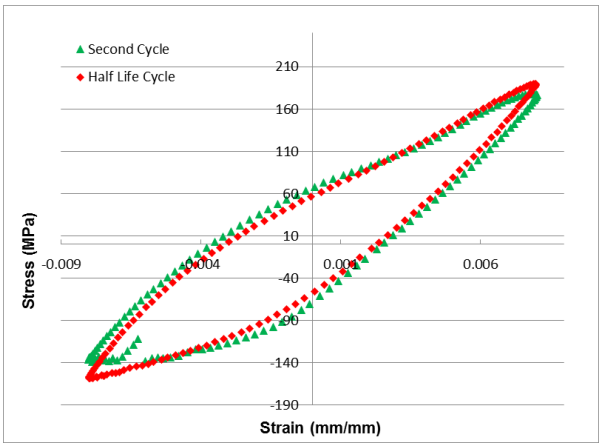

Figure 38 Second cycle and stabilized stress-strain hysteresis at 0.8% strain amplitude (ZEK100).

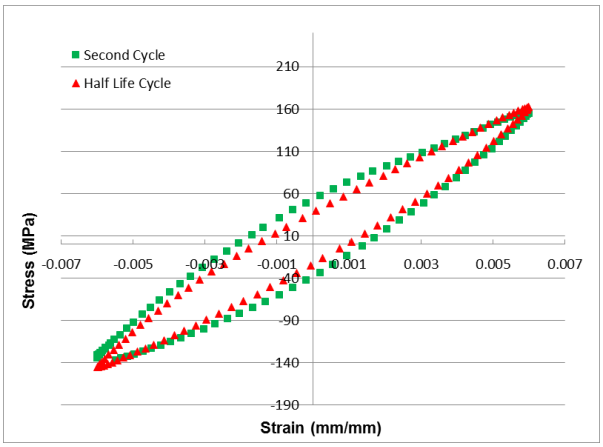

Figure 39 Second cycle and stabilized stress-strain hysteresis at 0.6% strain amplitude (ZEK100).

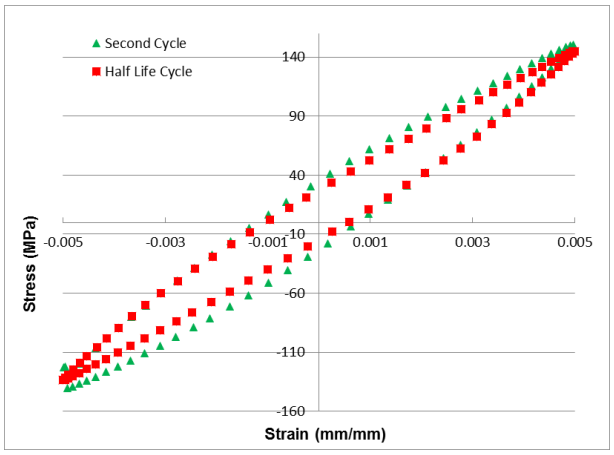

Figure 40 Second cycle and stabilized stress-strain hysteresis at 0.5% strain amplitude (ZEK100).

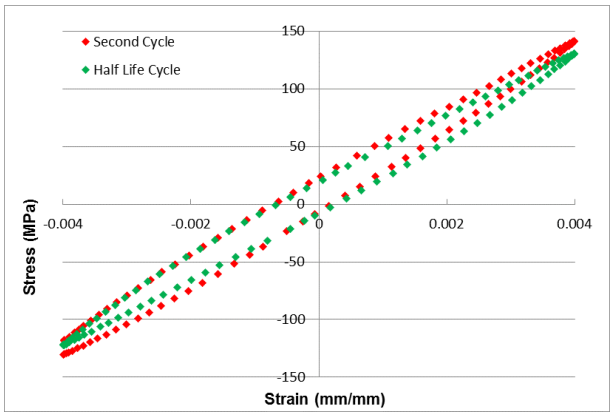

Figure 41 Second cycle and stabilized stress-strain hysteresis at 0.4% strain amplitude (ZEK100).

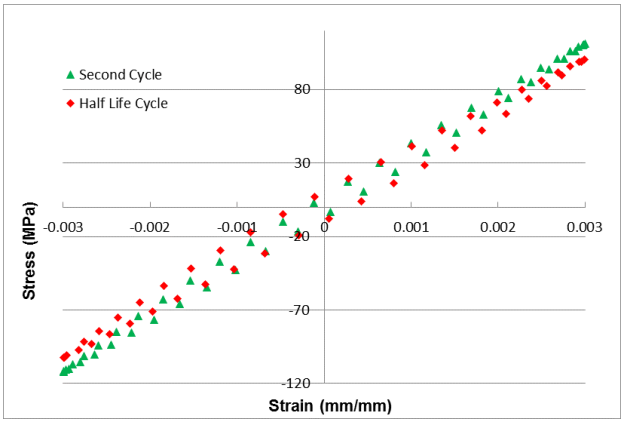

Figure 42 Second cycle and stabilized stress-strain hysteresis at 0.3% strain amplitude (ZEK100).

The sigmoidal shape of the stress-strain hysteresis loops, especially the upward reversal, can be observed in the relatively higher strain amplitude cases (> 0.5%) due to twinning/de-twinning.

A relatively weak tension-compression asymmetry is also observed even at relatively high strain amplitudes to due to the weakened basal texture, as discussed in chapter 1. For both 2.3% and 1.5% stress-strain hysteresis loops, the relaxation behavior is seen by comparing the second cycle and the half-life cycle.

A plot of the stress amplitude versus cycle plot is shown in Figure 43:

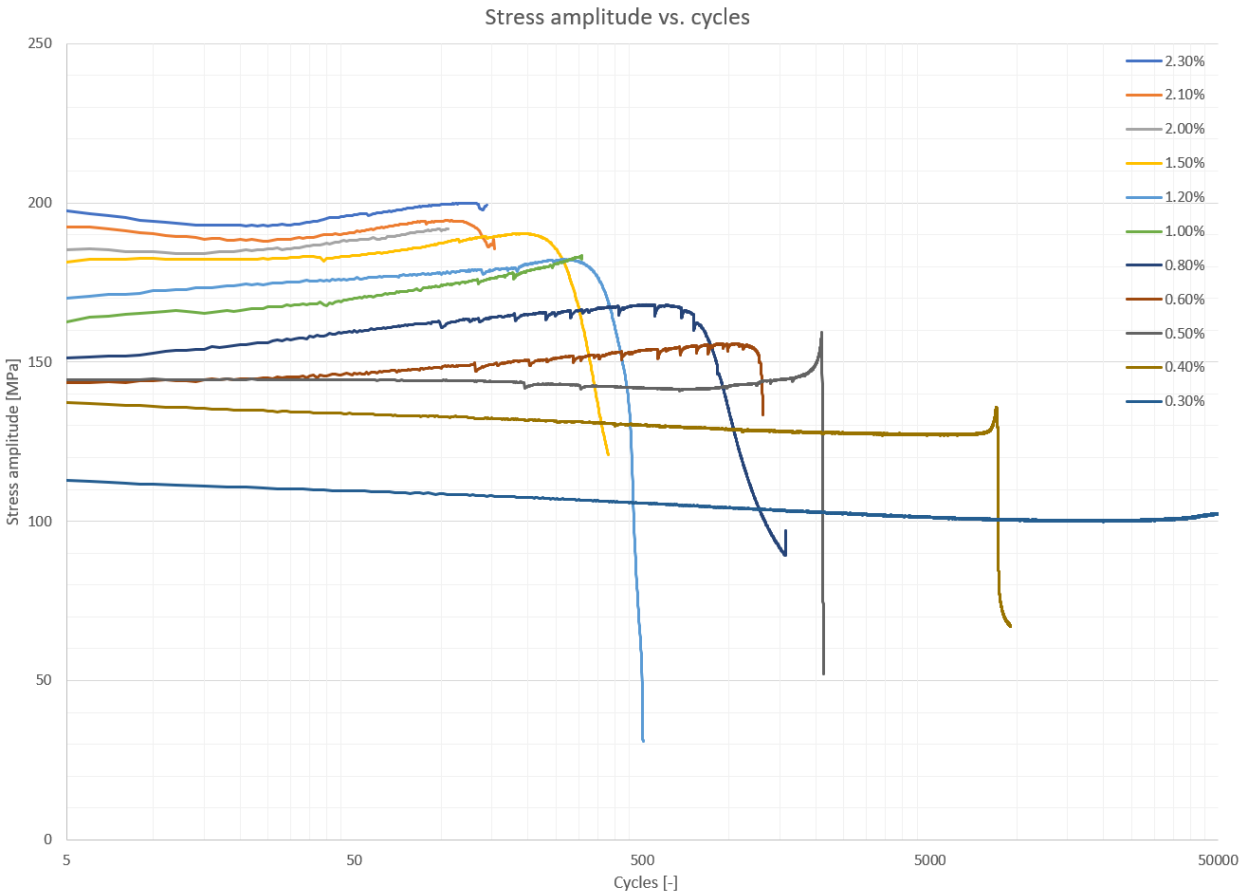

Figure 43. Stress amplitude vs. cycles plot for ZEK100-O (strain-controlled R=-1)

Hardening behavior is observed above 0.5% of strain amplitude whereas softening behavior is observed at and below. However, for both 1.5% and 2.3% strain amplitudes, the material seems to be softening at the beginning and then start to harden after some cycles for the strain amplitude equal and above 2.0%.

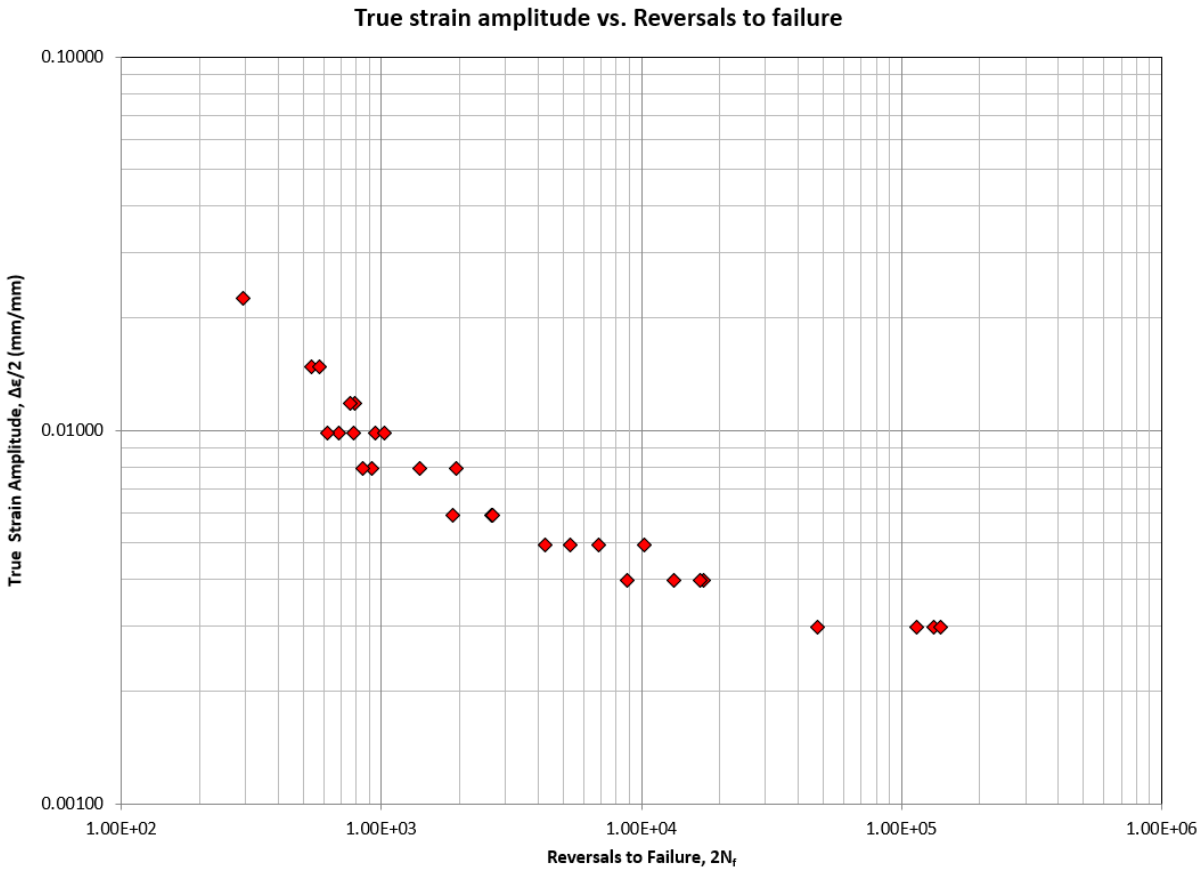

Figure 44. True strain amplitude vs. Reversals to failure (ZEK100-O R=-1 strain-controlled tests)

The strain amplitude vs. life curve for the fully-reversed strain-controlled tests is shown in Figure 44, which will be later used to find the parameters for the fatigue models.

3.4.3 Mean strain effects

In order to study the mean-strain effect on ZEK100-O magnesium alloy, a series of strain-controlled tests have been done with different stain amplitudes ranged from 0.40% to 1.0% while kept R ratio equals 0. The stress-strain hysteresis loops are shown in Figure 45 to Figure 48:

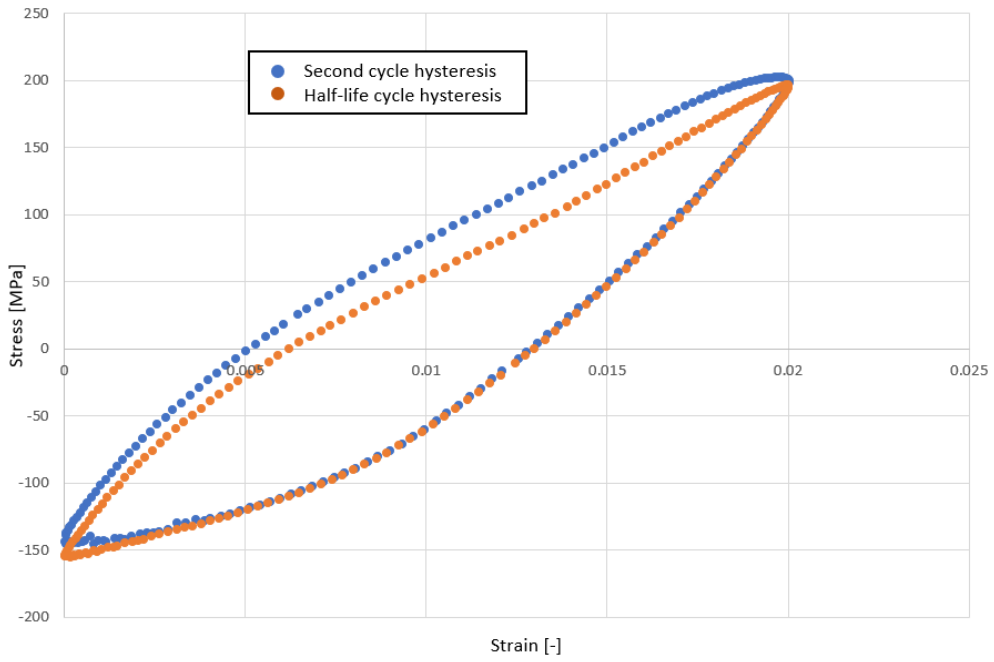

Figure 45. Strain-controlled R=0 test @ 1.00% strain amplitude- ZEK100-O

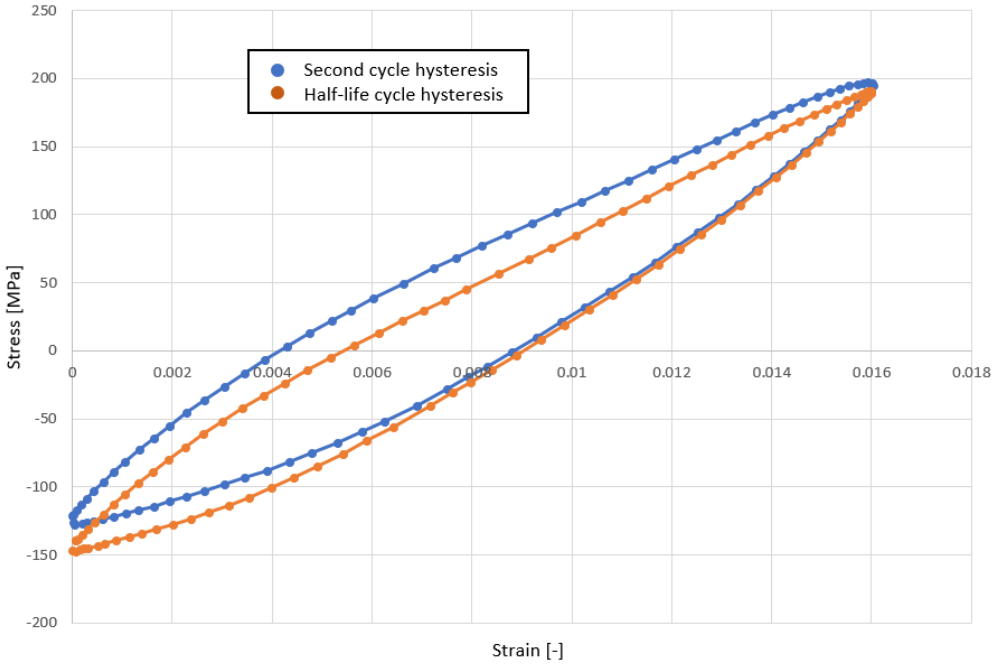

Figure 46. Strain-controlled R=0 test @ 0.80% strain amplitude- ZEK100-O

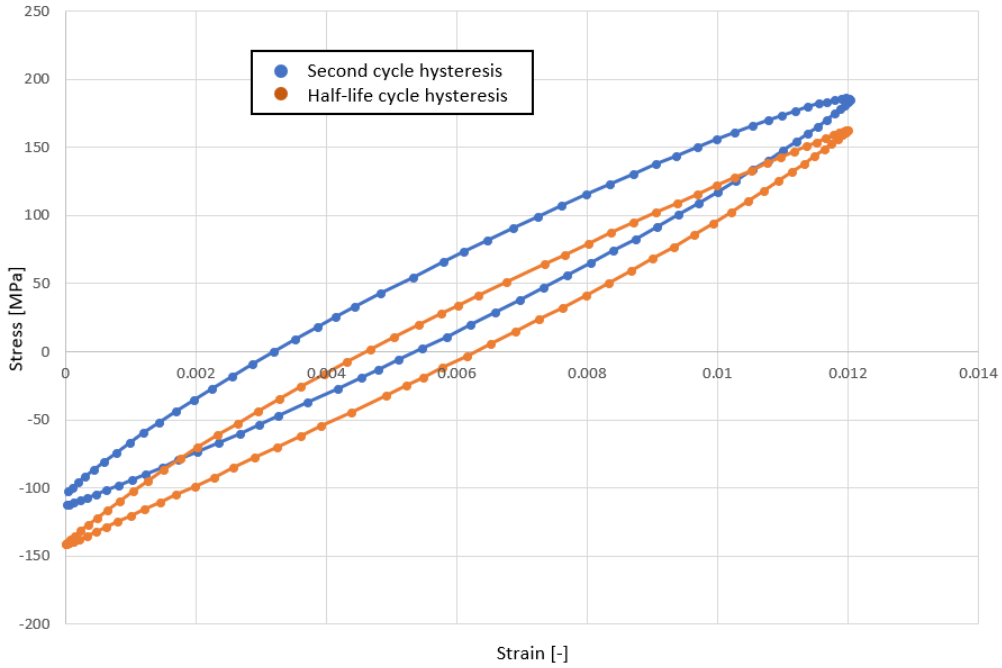

Figure 47. Strain-controlled R=0 test @ 0.60% strain amplitude- ZEK100-O

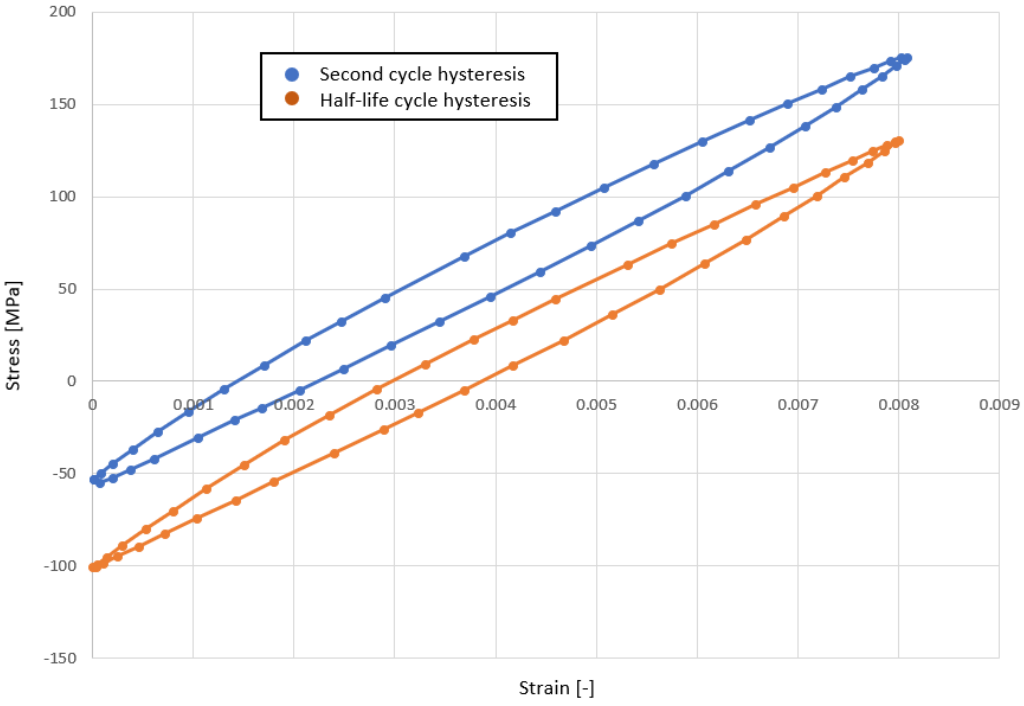

Figure 48. Strain-controlled R=0 test @ 0.40% strain amplitude- ZEK100-O

Relaxation behavior has been observed in all cases from 0.40% to 1.0%, however, it is more pronounced at lower strain amplitudes. A comparison of the stress-strain hysteresis loops between fully-reversed (R=-1) and R=0 for 1.0% and 0.4% is shown in Figure 49 and Figure 50:

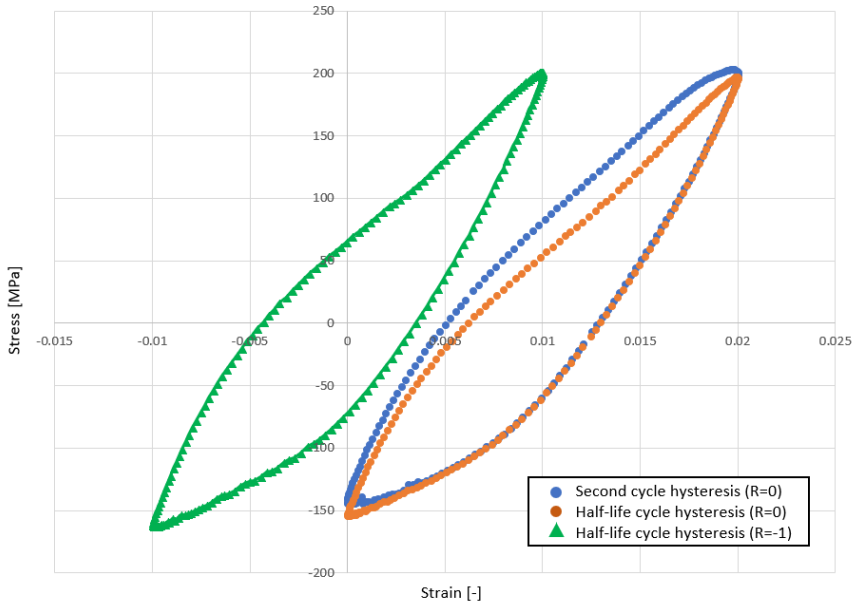

Figure 49. Strain-controlled R=0 and R=-1 tests comparison @ 1.00% strain amplitude- ZEK100-O

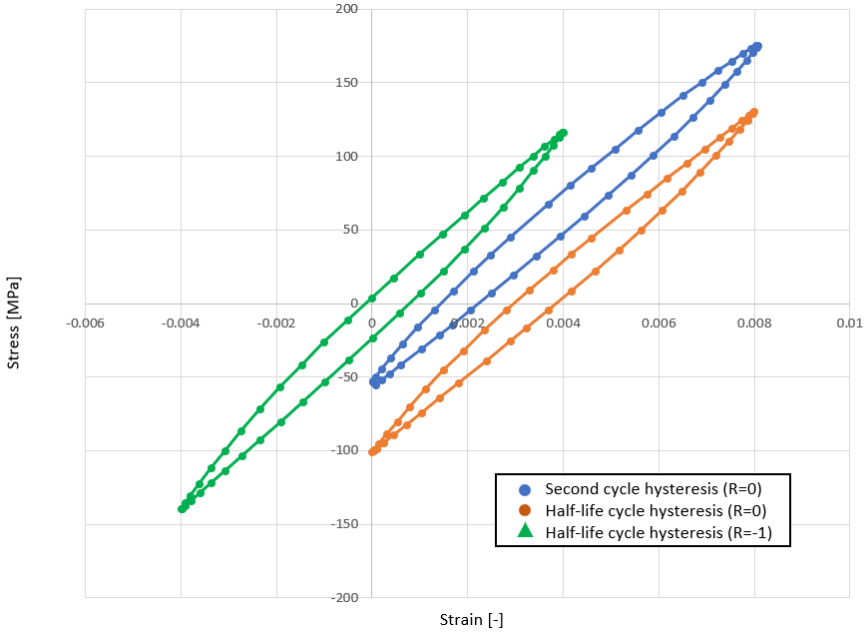

Figure 50. Strain-controlled R=0 and R=-1 tests comparison @ 0.40% strain amplitude- ZEK100-O

Noticed that the R=0 stabilized stress-strain hysteresis loop at 1% of strain amplitude closely resembles the shape of the stabilized hysteresis with R_ε=-1, however, the hysteresis loop shifted to the right-hand side due to the R_ε ratio. At 0.4% of strain amplitude, the lower reversing point for the R_ε=0 stress-strain hysteresis loop corresponds to a relatively higher compressive stress compare with the loop for R_ε=-1, whereas the maximum stresses at the top reversing point remain similar for both R_ε=0 and R_ε=-1 hysteresis loops. Due to the similarity of the stress-strain hysteresis loops, the damage has been down for each completed cycle for R_ε=0 and R_ε=-1 should similar. Therefore, it is likely that the mean strain will not have a great effect to the fatigue life of ZEK100-O magnesium alloy. By looking at the strain amplitude versus life curve shown in Figure 51, it seems like that, the R_ε=0 results actually have slight improved fatigue lives over the R_ε=-1 tests, however, additional tests are needed to make this conclusion.

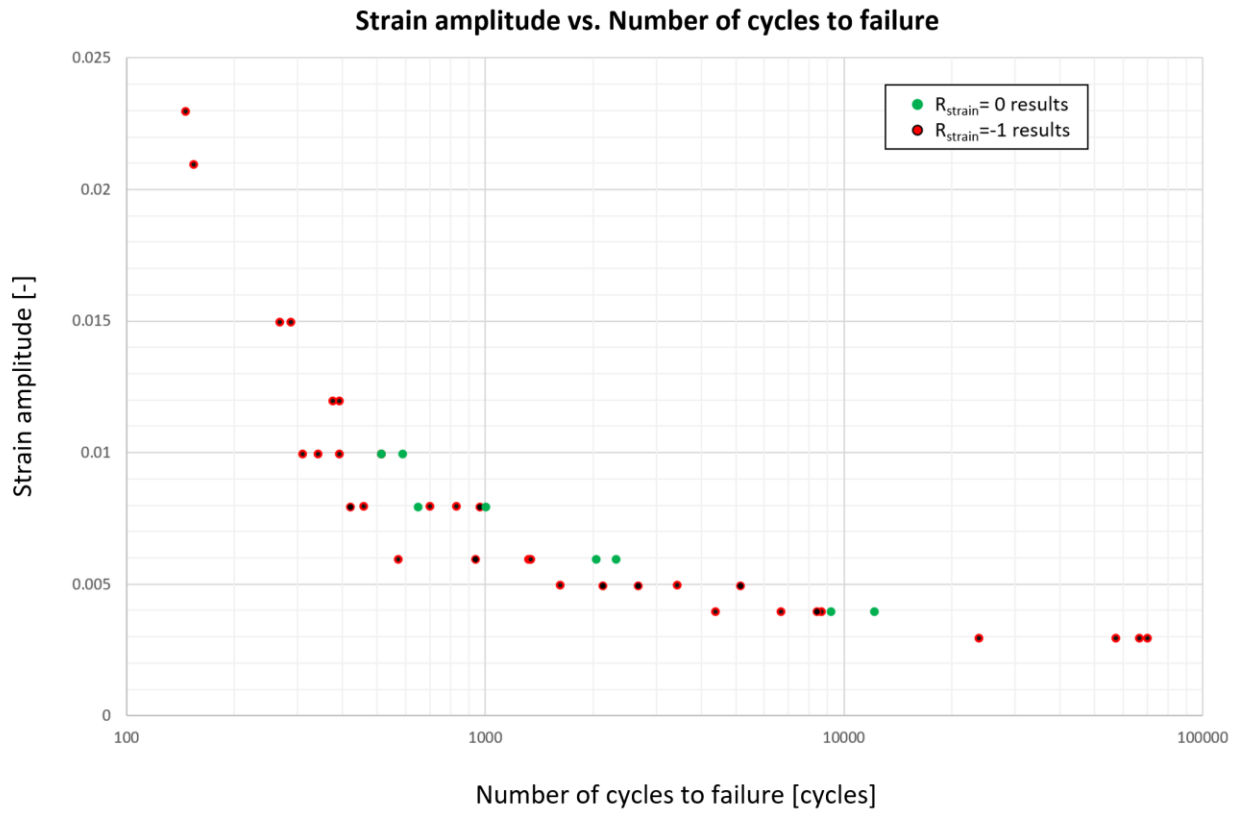

Figure 51. Strain amplitude vs. life curve for both R_ε=0 and R_ε=-1 tests

The experimental lives for R_ε=0 tests are summarized in:

Strain amplitude [%]	Experimental life*
1.0	584
	508
0.8	644
	996
0.6	2292
	2025
0.4	12032
	9124

Table 6. Summary of the fatigue lives of the R_ε=0 fatigue tests (failure criterial: 15% of load drop or fracture)- ZEK100-O

3.4.4 Mean stress effects

Stress controlled-tests at R ratio equals -1 and 0 were conducted to study the mean stress effect on fatigue life for ZEK100-O magnesium alloy. Although these tests were stress-controlled, the extensometer was attached to get the stress-strain responses. The R_σ=0 tests have been done at three different stress amplitudes (80 MPa, 100 MPa and 110 MPa) and the results are shown in Figure 52 - Figure 54:

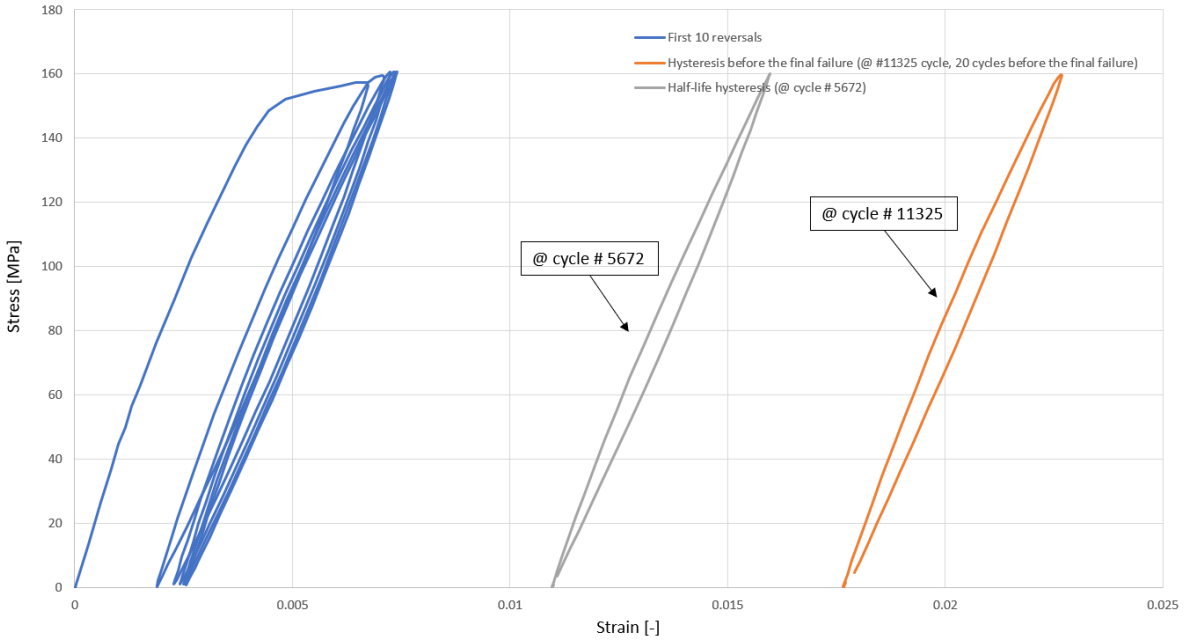

Figure 52. The R_σ=0 tests on smooth specimen with stress amplitude of 80 MPa (ZEK100-O)

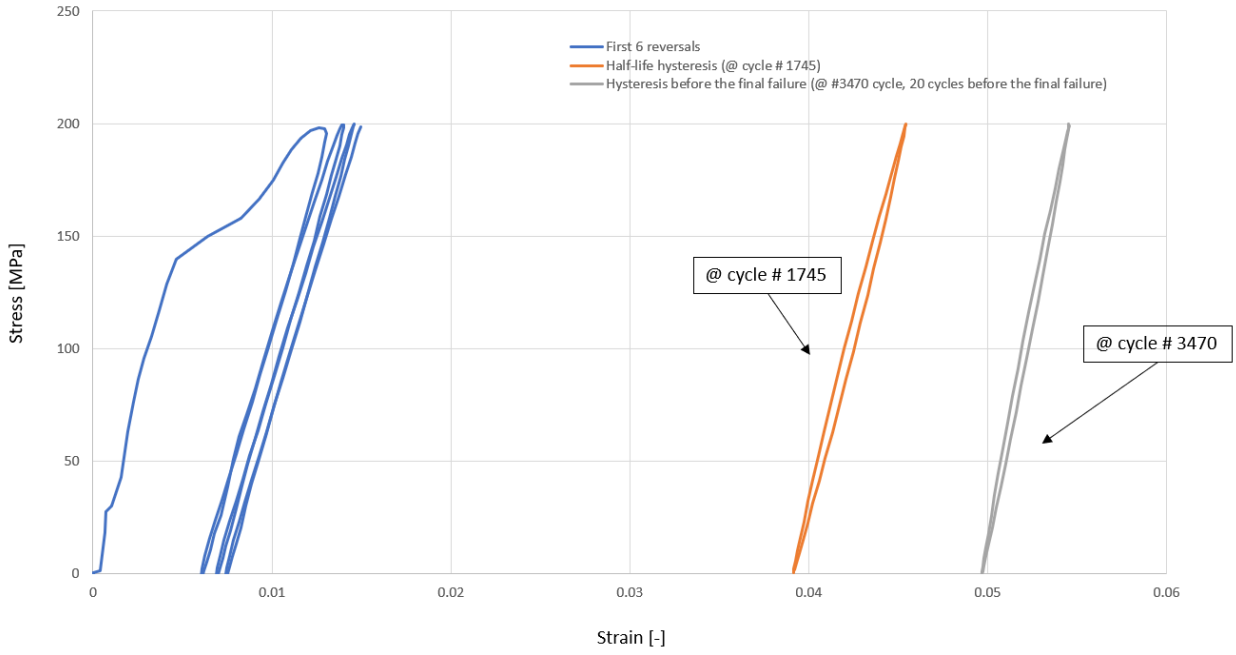

Figure 53. The R_σ=0 tests on smooth specimen with stress amplitude of 100 MPa (ZEK100-O)

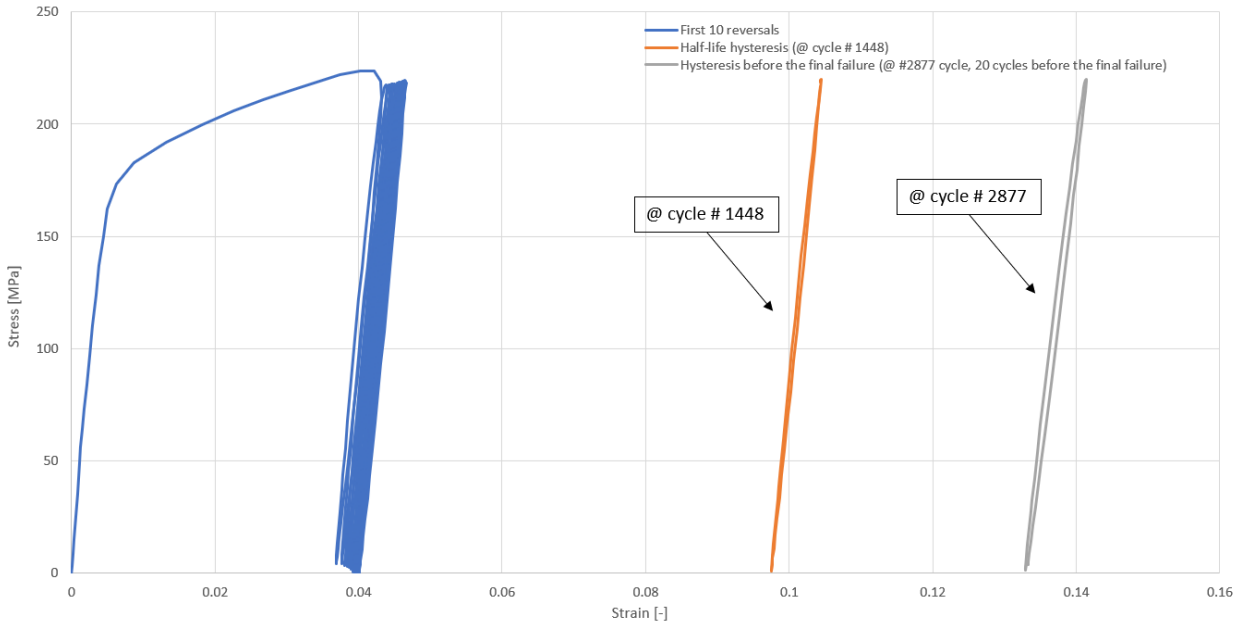

Figure 54. The R_σ=0 tests on smooth specimen with stress amplitude of 110 MPa (ZEK100-O)

Significant amount of plastic deformation is observed for the first reversal for all three tests in comparison with the subsequent reversals. Although the ratcheting strains were built up through the progression of these tests, the shape of the stress-strain hysteresis loops for each completed cycle is almost the same after a number of cycles at each stress amplitude level.

A summary of the fatigue lives for all the stress-controlled R_σ=0 and R_σ=-1 tests is given in Table 7:

Stress Amplitude	R_σ=-1 life		R_σ=0 life		
80 MPa	N/A (Expected to be run-out)		11345 cycles	11990 cycles	12816 cycles
100 MPa	73582 cycles	54586 cycles	3324 cycles		3489 cycles
110 MPa	22981 cycles	25554 cycles	2989 cycles		2897 cycles

Table 7. Fatigue lives for all the stress-controlled R_σ=0 and R_σ=-1 tests

It is apparent that the positive mean stresses are greatly detrimental to the fatigue life of ZEK100-O. The fatigue life at the stress amplitudes of 100 MPa and 110MPa have been reduced by an order of magnitude due to the positive mean stresses. The R_σ=-1 fatigue life for 80 MPa is expected to be more than 10 million cycles, which is at least 3 orders of magnitude greater than the fatigue life for the R_σ=0 counterpart at around 12 thousand cycles.

The stress versus life curves for R_σ=0 and R_σ=-1 tests are given in Figure 55:

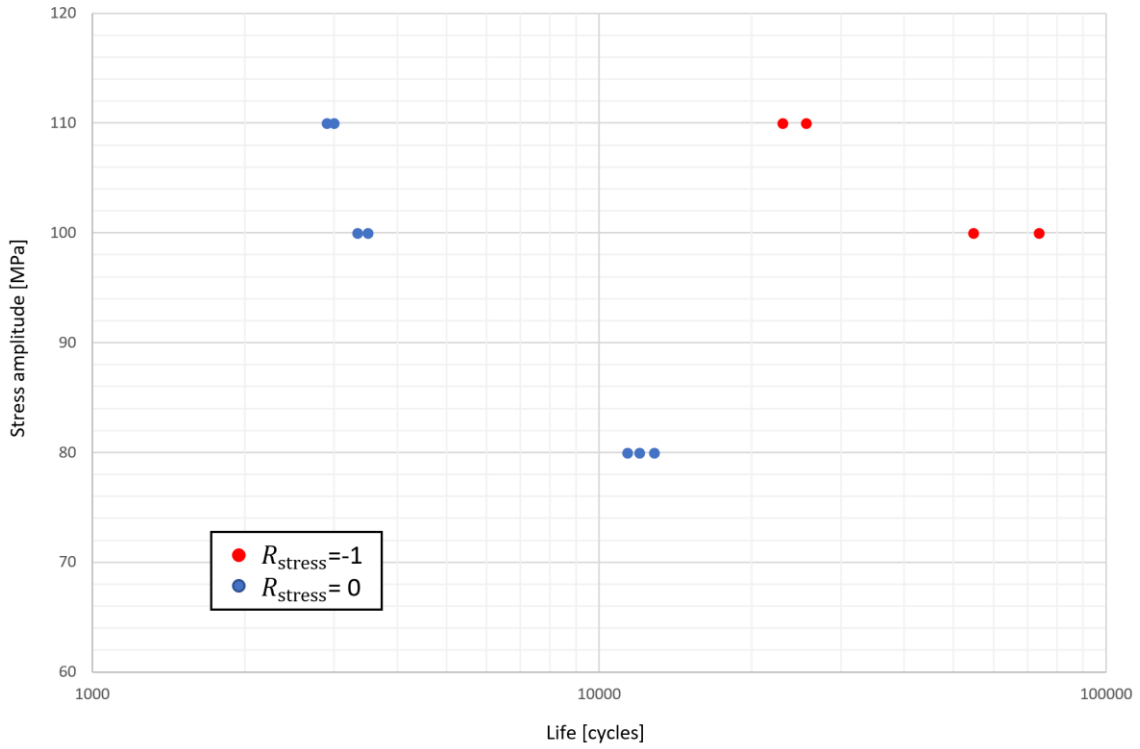

Figure 55. Strain-life curve for all the stress-controlled R_σ=0 and R_σ=-1 test

These results will be later used to evaluate the mean-stress effect predictions of the fatigue models in chapter 5.

3.4.5 Variable amplitude strain-controlled cyclic results

Several strain-controlled variable amplitude tests on ZEK100-O magnesium alloy have been done. These results will be used to examine the validity of Miner's rule on this material and to check the goodness of the phenomenological model. The strain histories and their corresponding stabilized stress-strain hysteresis loops are shown in Figure 56 to Figure 59:

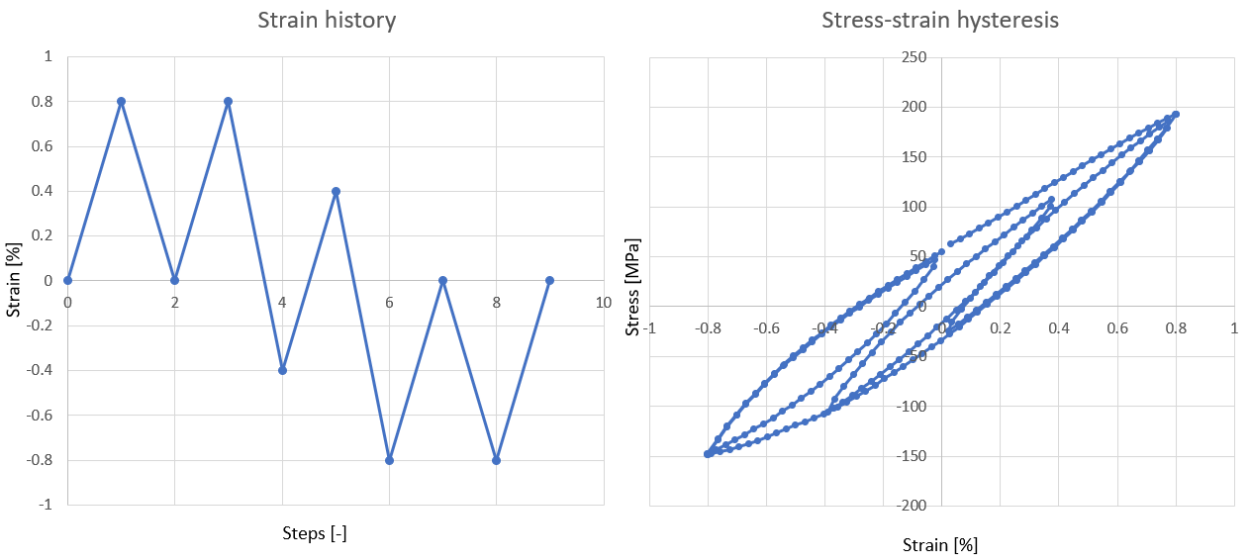

Figure 56. Variable amplitude strain-controlled test #1 (545 blocks of the given load history applied to failure- 15% load drop) - ZEK100-O

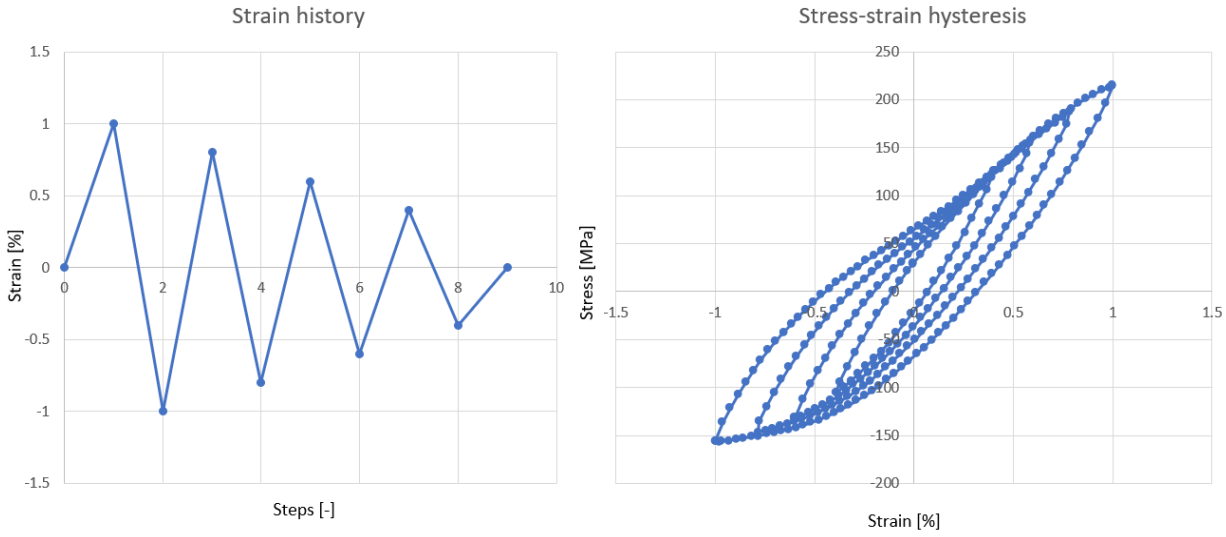

Figure 57. Variable amplitude strain-controlled test #2 (206 blocks of the given load history applied to failure- 15% load drop) - ZEK100-O

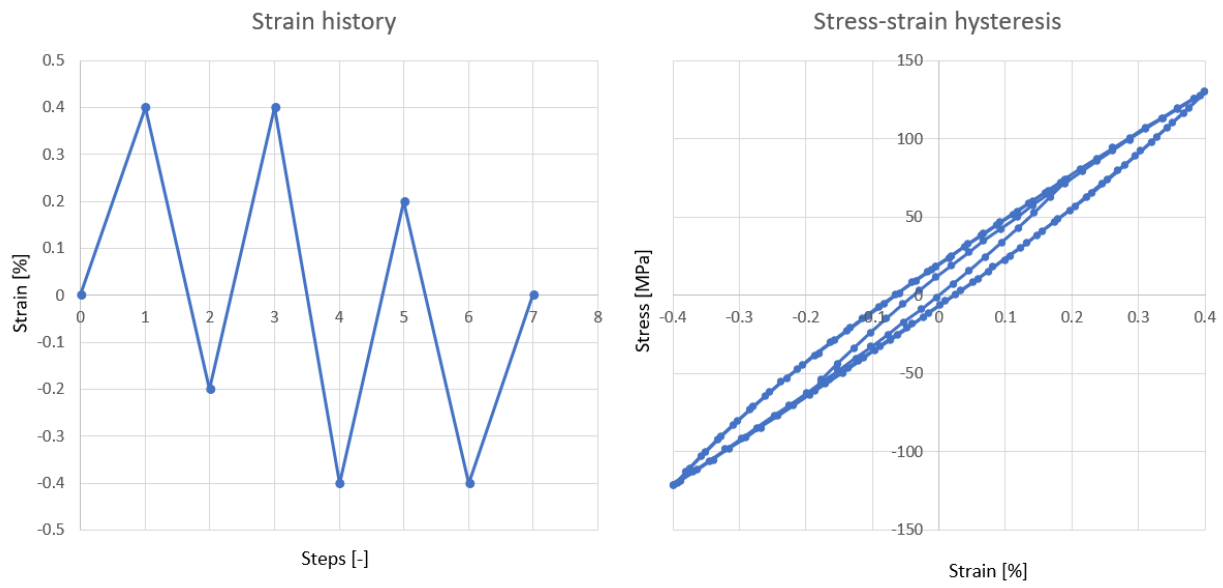

Figure 58. Variable amplitude strain-controlled test #3 (4130 blocks of the given load history applied to failure- 15% load drop) - ZEK100-O

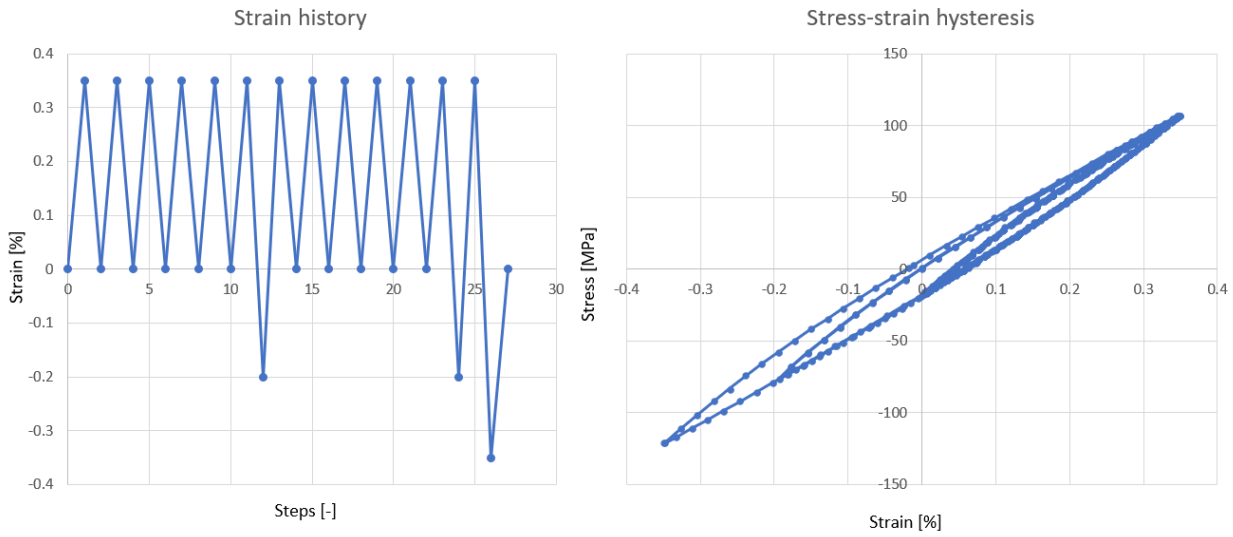

Figure 59. Variable amplitude strain-controlled test #4 (3900 blocks of the given load history applied to failure- 15% load drop) - ZEK100-O

The failure criterion for these variable amplitude tests is similar to the failure criteria for the constant amplitude tests, which is defined by 15% of load drops for the envelope hysteresis loop or final fracture.

The fatigue lives for the variable amplitude tests are measured by number of blocks of the given load histories applied.

3.5. Cyclic properties of the notched specimens

3.5.1 Specimen geometry and test setup

The geometric of the notched sample is shown in Figure 60:

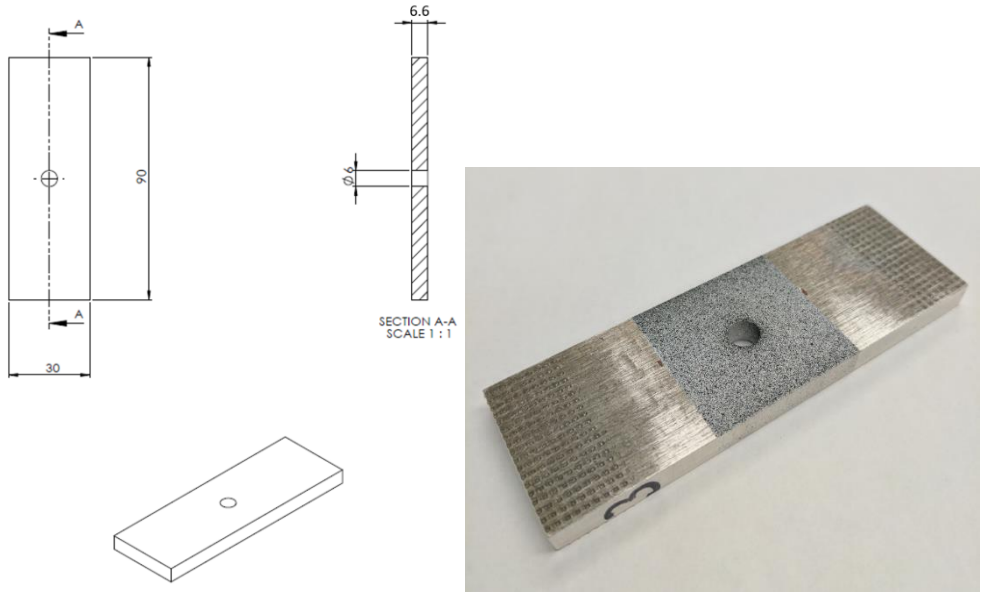

Figure 60 Notched specimen with applied speckle pattern for digital image correlation (DIC) analysis.

Based on the geometry of this specimen, the elastic stress concentration factor at the notch root (K_t) is 2.5 relative to the net nominal stress. Similar to the test setup for quasi-static compression tests, a single DIC camera was used to capture the strain field at the vicinity of the notch root on the surface of the notched specimen. The field of view of the DIC camera is shown in Figure 61 and the corresponding directions associated:

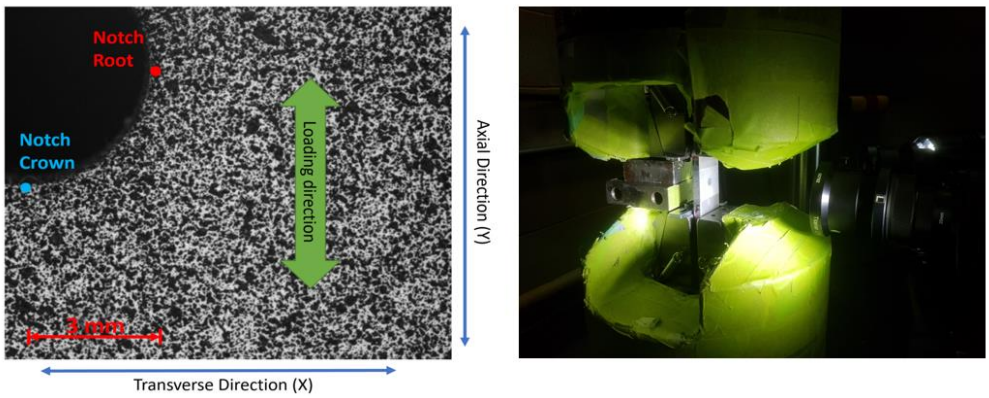

Figure 61. DIC field of view (left) and the notched test setup (right).

3.5.2 Constant nominal stress amplitude results

Constant nominal stress amplitude and fully-reversed ($R_{\text{stress (nominal)}}$=-1) load-controlled tests were carried out with four different amplitudes based on the compressive yield limit of ZEK100-O.

Supplemental notch tests on AZ31B-H24 rolled sheet, which is a common type of commercially available rolled, strain hardened and partially annealed magnesium alloy, with two different nominal stress amplitudes have also been conducted for the sake of examining the generality of the model predictions and fatigue life estimations associated on different types of wrought magnesium alloys in chapter 4 and chapter 5.

ZEK100-O notched specimens were tested under 50%, 60%, 70% and 80% of compressive yield equivalent nominal stress (Correspond to 68.45, 82.14, 95.83 and 109.52 MPa, respectively) due to the fact that the compressive yield limit is lower than its tensile counterpart. These load levels were chosen to induce sufficient amount of plasticity at the vicinity of the notch root while preventing general yielding happen.

Since the material within the plastic zone at the vicinity of the notch root is nether stress controlled nor strain controlled, to study whether the material is going to stabilize or not, a strain progression test is carried out and the results are shown in Figure 62:

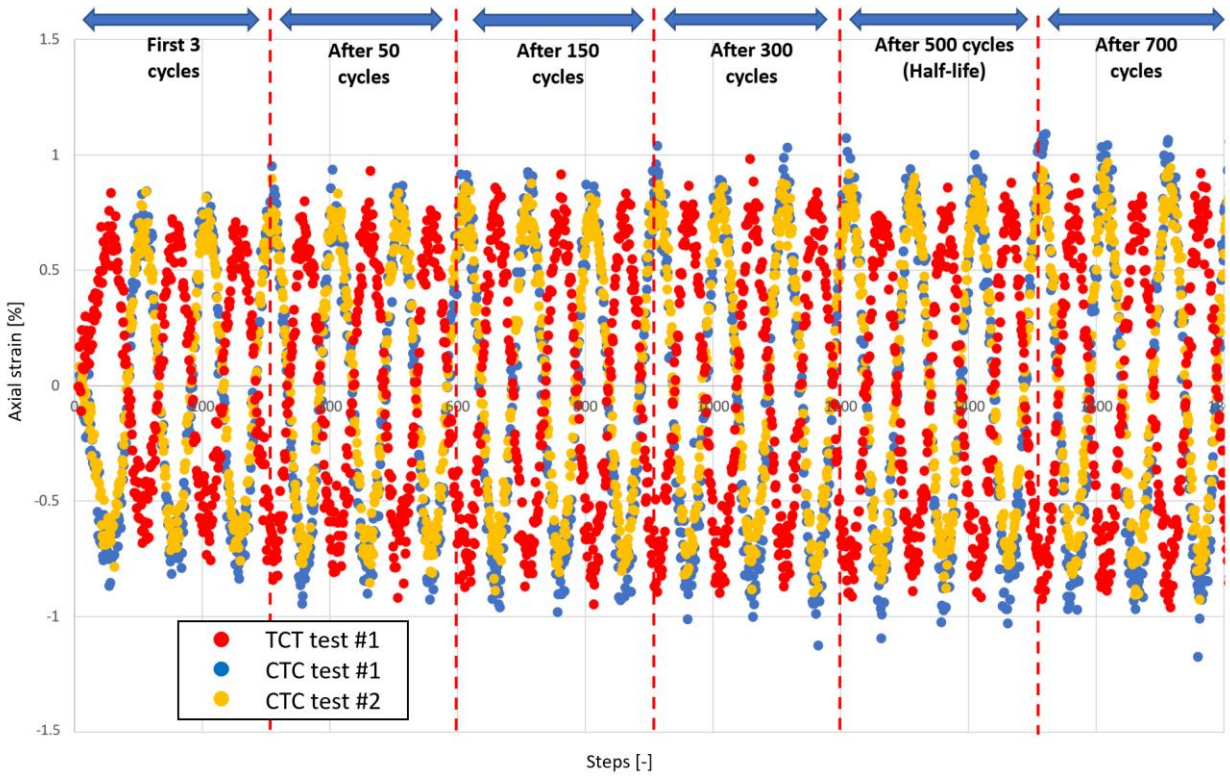

Figure 62. Axial strain progression at the notch root test for ZEK100-O at 80% of compressive yield equivalent fully-reversed nominal stress (3 Cycles were captured each time start at the beginning, after 50 cycles, 150 cycles, etc. Three different tests are shown; two of them started with compression-tension-compression and a single test started with tension-compression-tension)

Three cycles were captured start at the beginning and after 50, 150, 300, 500, 700 cycles for the sake of consistency. In addition, three different tests are presented; one test started with tension-compression-tension and the other two started with compression-tension-compression. It can be seen that the axial strain at the notch root has already been stabilized after 50 cycles for both TCT and CTC tests and no noticeable difference can be observed in terms of the measured notch strains after that. Besides, the loading pattern (TCT or CTC) does not have a noticeable effect to the cyclic notch strain responses for the test results presented.

To capture the axial strain responses at each load level, three cycles were captured after stabilization for consistency and the axial (y) strain field at the maximum tensile and compressive load are also shown in Figure 63-Figure 66:

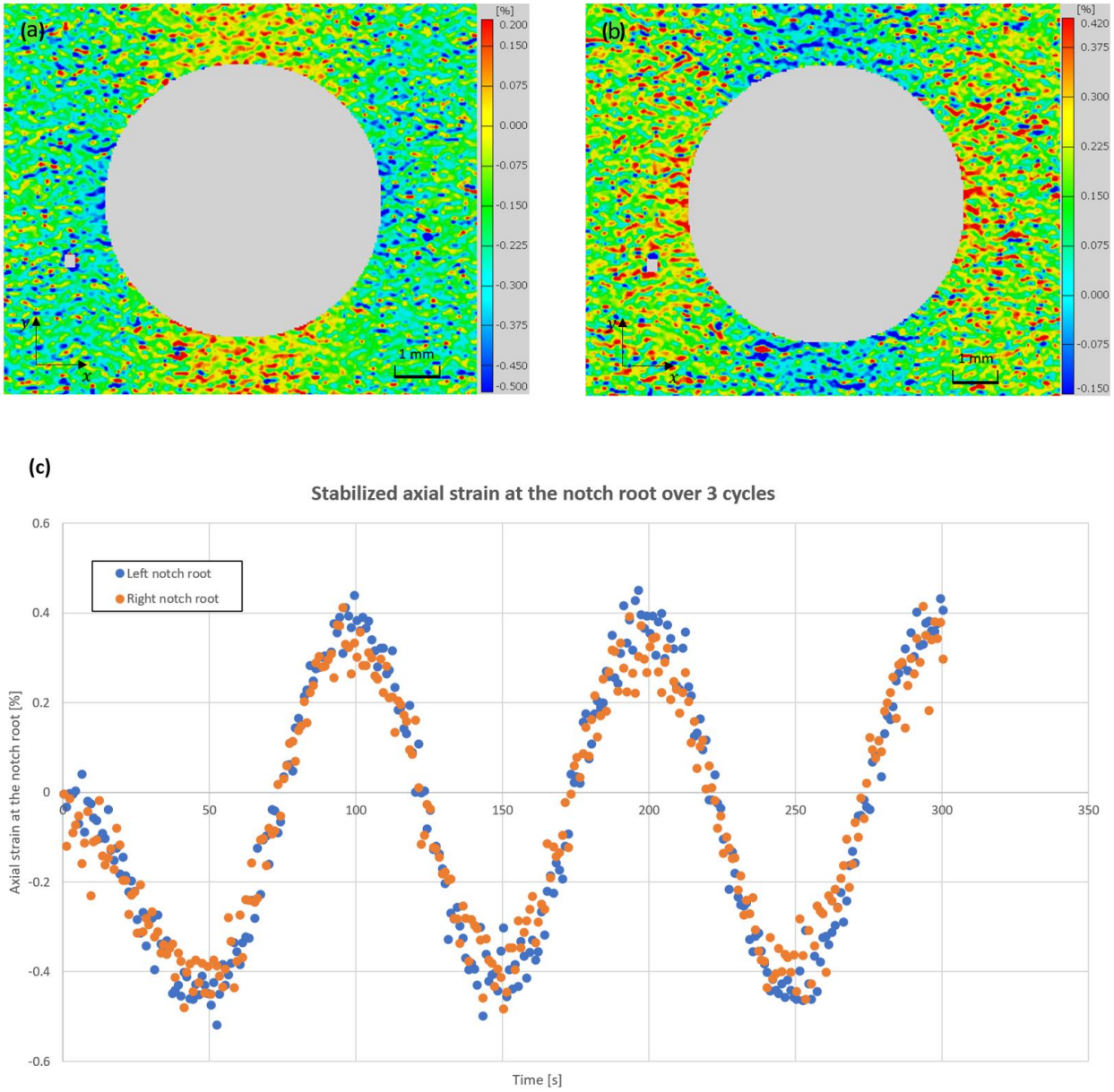

Figure 63. Stabilized strain field at (a) maximum compressive load (b) maximum tensile load and (c) axial strain at the notch root progression over 3 cycles- ZEK100-O @ 50% of compressive yield equivalent nominal stress (68.45 MPa) Note that the scales in (a) and (b) are different

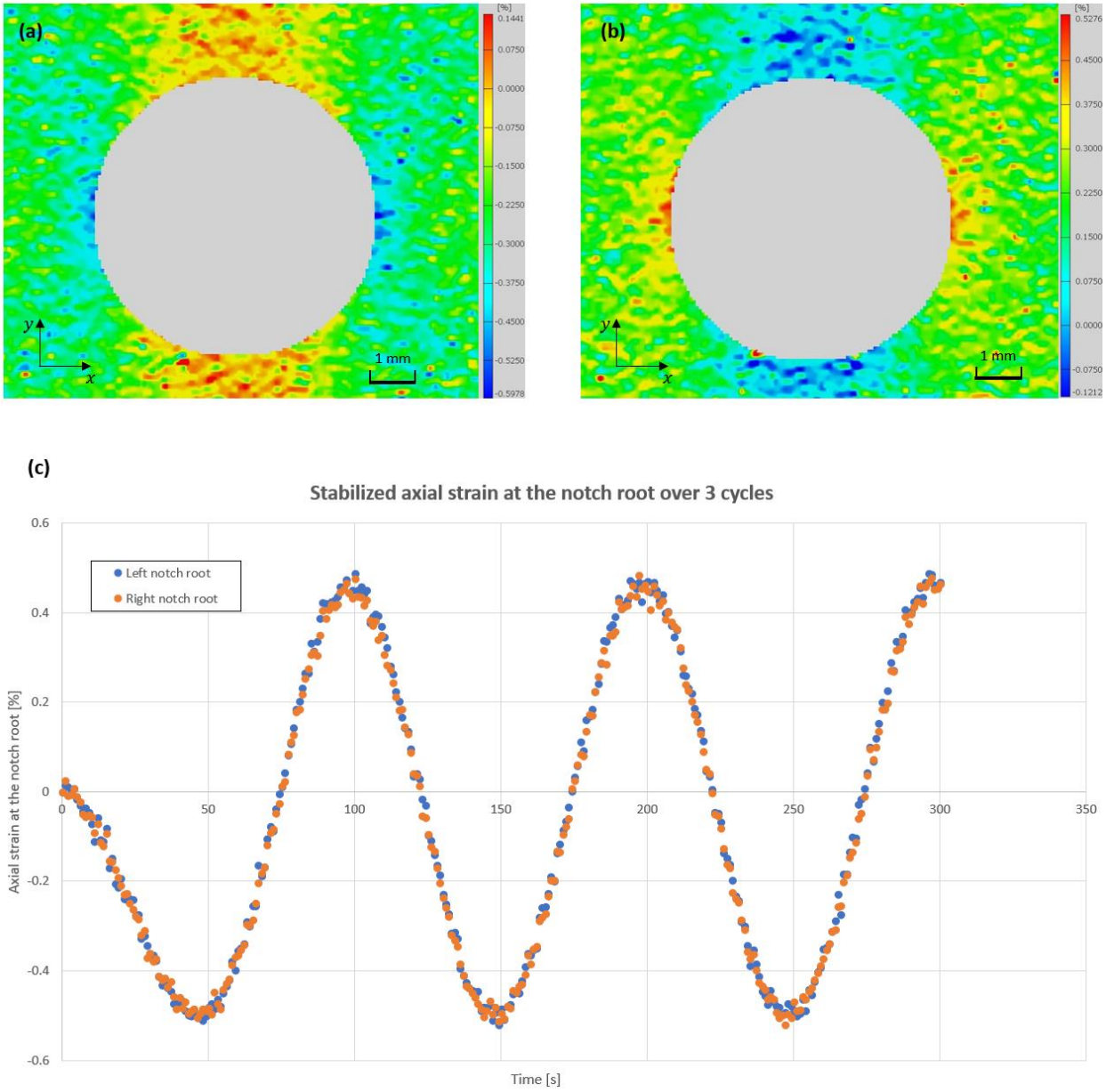

Figure 64. Stabilized strain field at (a) maximum compressive load (b) maximum tensile load and (c) axial strain at the notch root progression over 3 cycles- ZEK100-O @ 60% of compressive yield equivalent nominal stress (82.14 MPa) Note that the scales in (a) and (b) are different

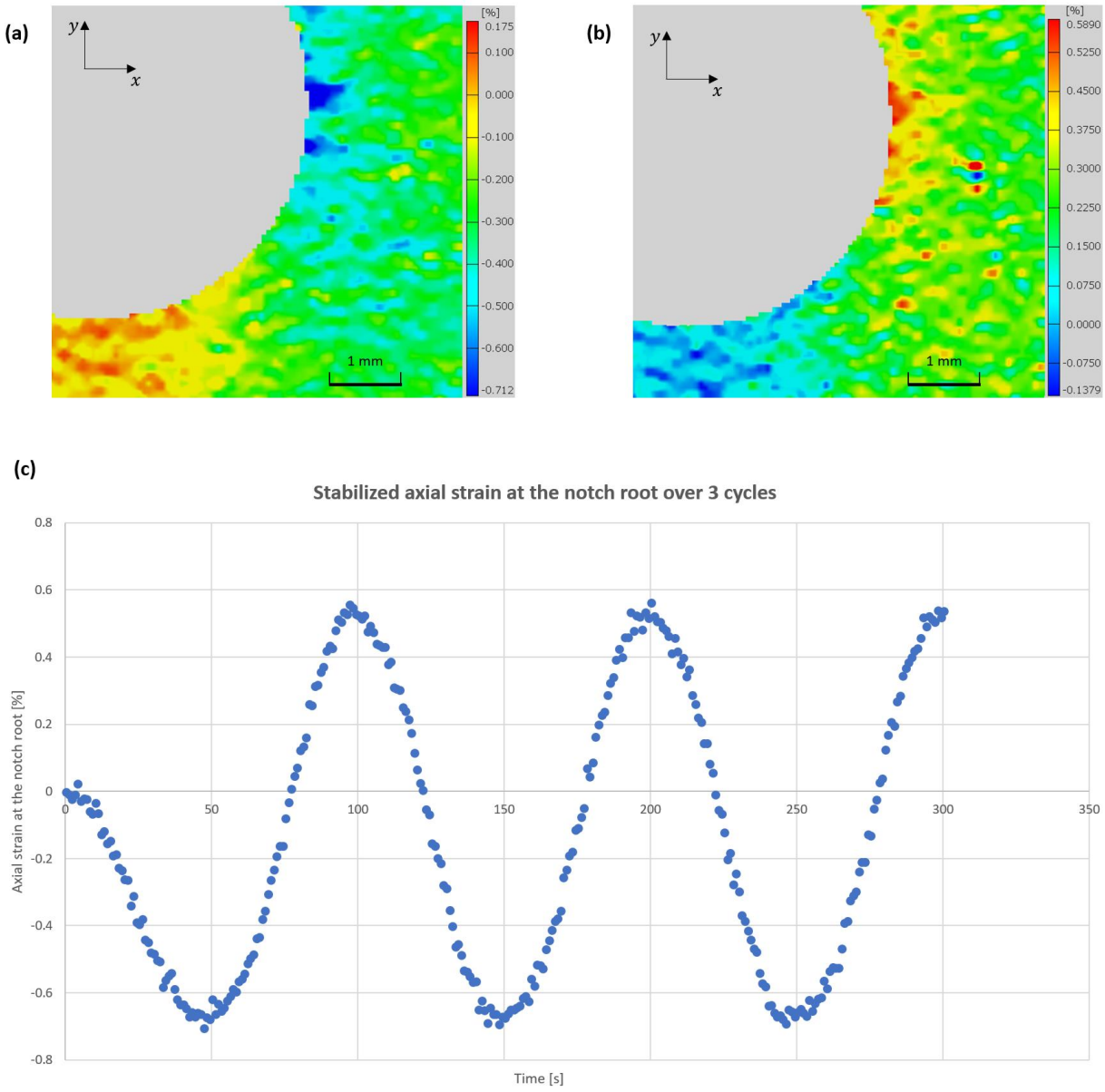

Figure 65. Stabilized strain field at (a) maximum compressive load (b) maximum tensile load and (c) axial strain at the notch root progression over 3 cycles- ZEK100-O @ 70% of compressive yield equivalent nominal stress (95.83 MPa) Note that the scales in (a) and (b) are different

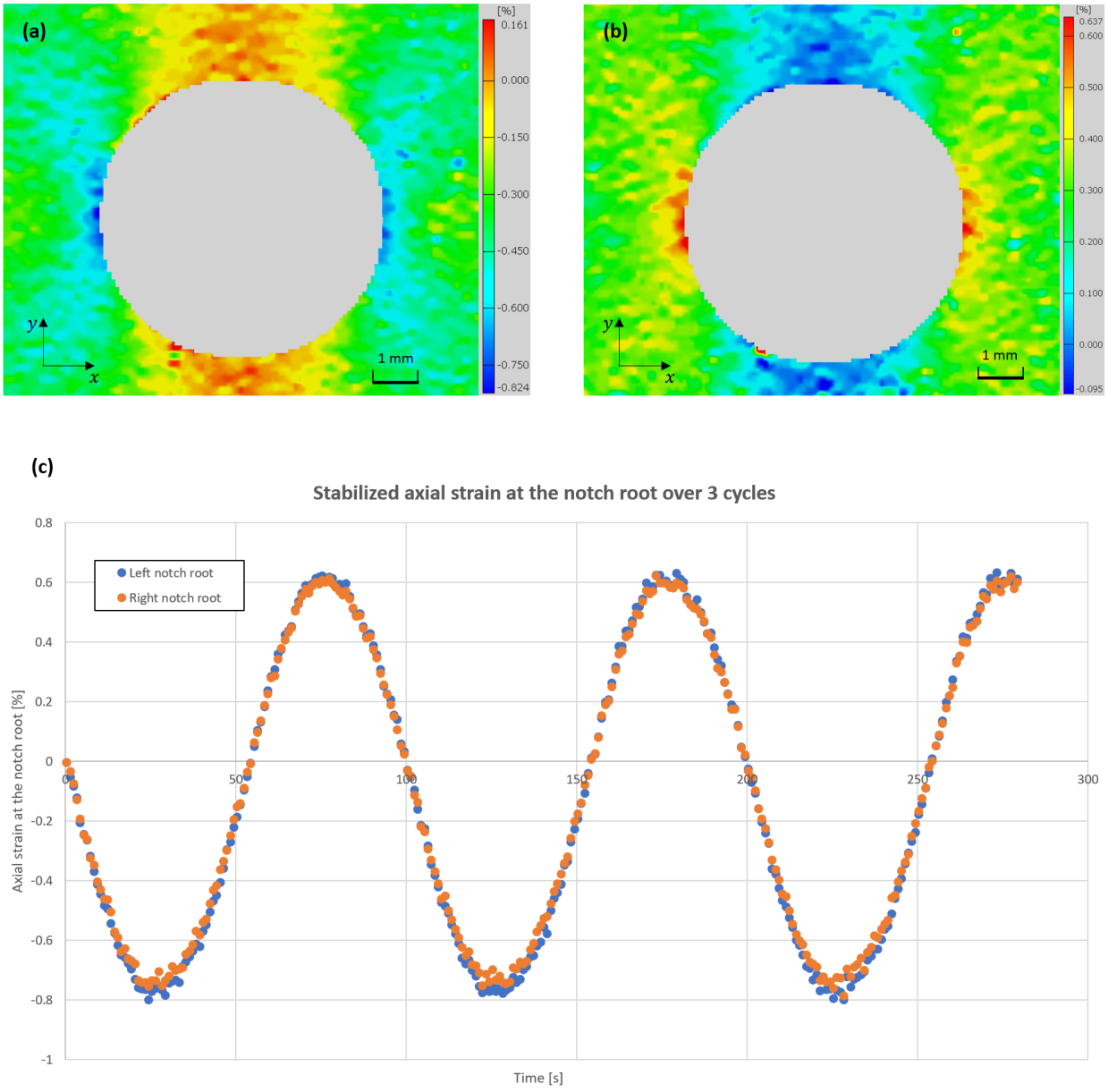

Figure 66. Stabilized strain field at (a) maximum compressive load (b) maximum tensile load and (c) axial strain at the notch root progression over 3 cycles- ZEK100-O @ 80% of compressive yield equivalent nominal stress (109.52 MPa) Note that the scales in (a) and (b) are different

Due to the limitations of the measurement technique (DIC), substantial amount of noise was introduced due to the inconsistency of speckle patterns, lighting conditions, etc. especially when the strain to be measured is relatively low, as seen in Figure 63 - (a), (b).

A summary of the notch strains measured at the peak tensile and compressive nominal stresses as well as the fatigue life (if available) is shown in Table 8:

Nominal stress level	Notch axial strain at maximum tensile load [%]	Notch axial strain at maximum compressive load [%]	Fatigue Life* (Cycles)
50% CYS equivalent load (68.45 MPa)	0.36	-0.42	N/A
60% CYS equivalent load (82.14 MPa)	0.46	-0.49	~ 4500
70% CYS equivalent load (95.83 MPa)	0.53	-0.66	N/A
80% CYS equivalent load (109.52MPa)	0.62	-0.74	~ 1000

Table 8. Axial notch strains measured at peak tensile and compressive nominal stresses at 50, 60, 70 and 80 percent of compressive yield equivalent fully-reversed nominal stresses- ZEK100-O (The failure criteria for the fatigue life determination is defined by the first surface crack of a length exceed 100 μm)

Two of the crack initiation tests at 60% and 80% percent of compressive yield equivalent fully-reversed nominal stresses are also shown in Figure 67-Figure 68:

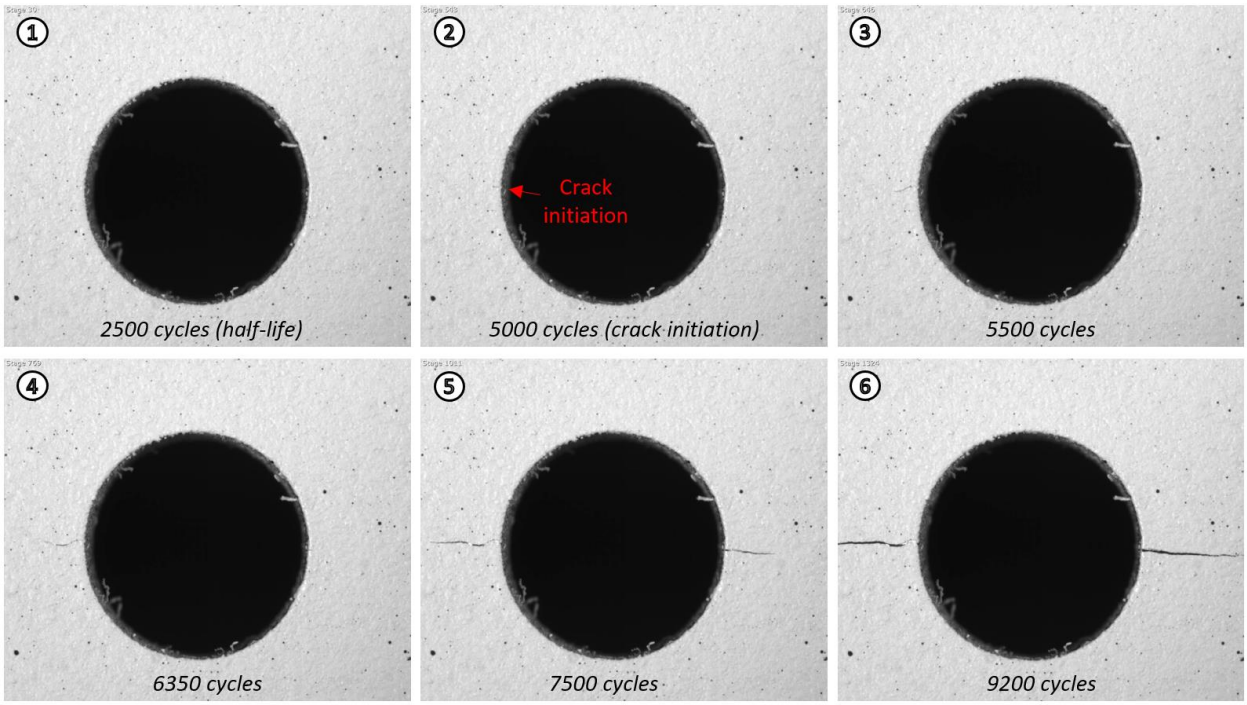

Figure 67. Crack initiation test for 60% of fully-reversed compressive yield equivalent nominal stress (82.14 MPa) - ZEK100-O

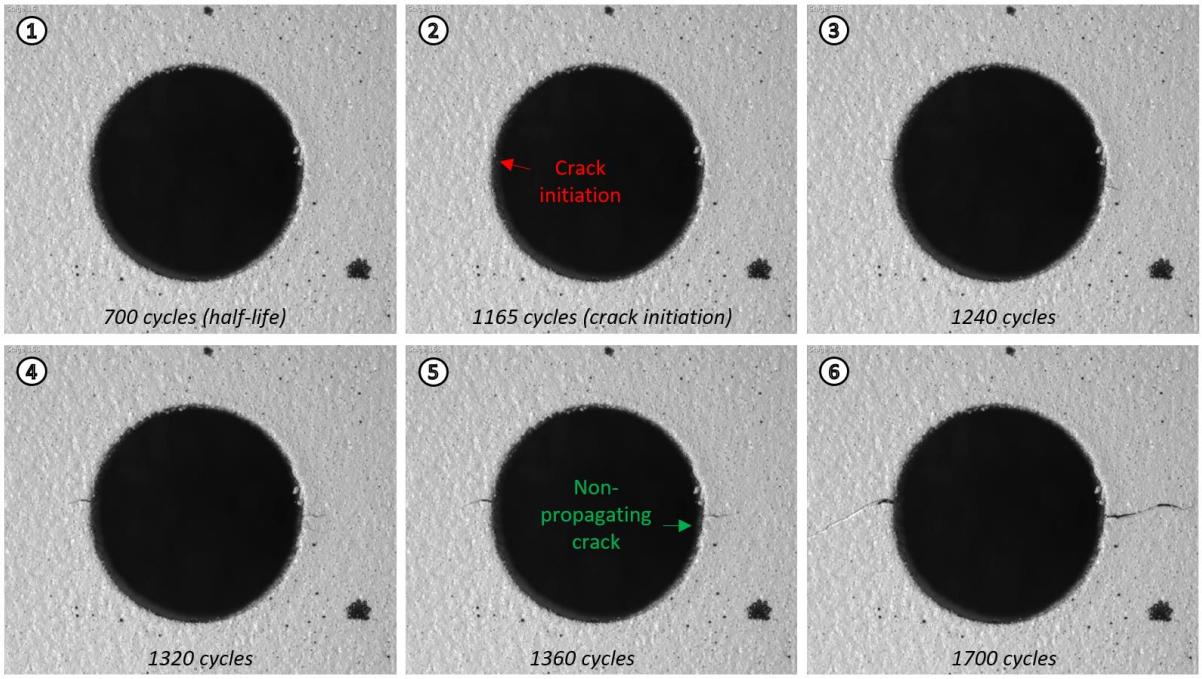

Figure 68. Crack initiation test for 80% of fully-reversed compressive yield equivalent nominal stress (109.52 MPa) - ZEK100-O

The fatigue crack initiation lives for all the constant amplitude notched tests on ZEK100-O are summarized in Table 9:

Test #	Stress amplitude (normalized to the compressive yield) and loading sequence	Crack initiation life (Crack length of ~ 100μm)
1	80%/ CTC	900 cycles
2	60%/ CTC	4500 cycles
3	80%/ TCT	710 cycles
4	80%/ CTC	1165 cycles
5	60%/ CTC	5065 cycles
6	80%/ CTC	900 cycles

Table 9. Fatigue crack initiation life summary on ZEK100-O magnesium alloy (The failure criteria for the fatigue life determination is defined by the first surface crack of a length exceed 100 μm)

Same tests at 60% (94.84 MPa) and 80% (126.45 MPa) of compressive yield equivalent fully-reversed nominal stresses have also been carried out on AZ31B-H24 magnesium alloy.

The strain progression tests on AZ31B- H24 at 80% of compressive yield equivalent fully-reversed nominal stresses are shown in Figure 69:

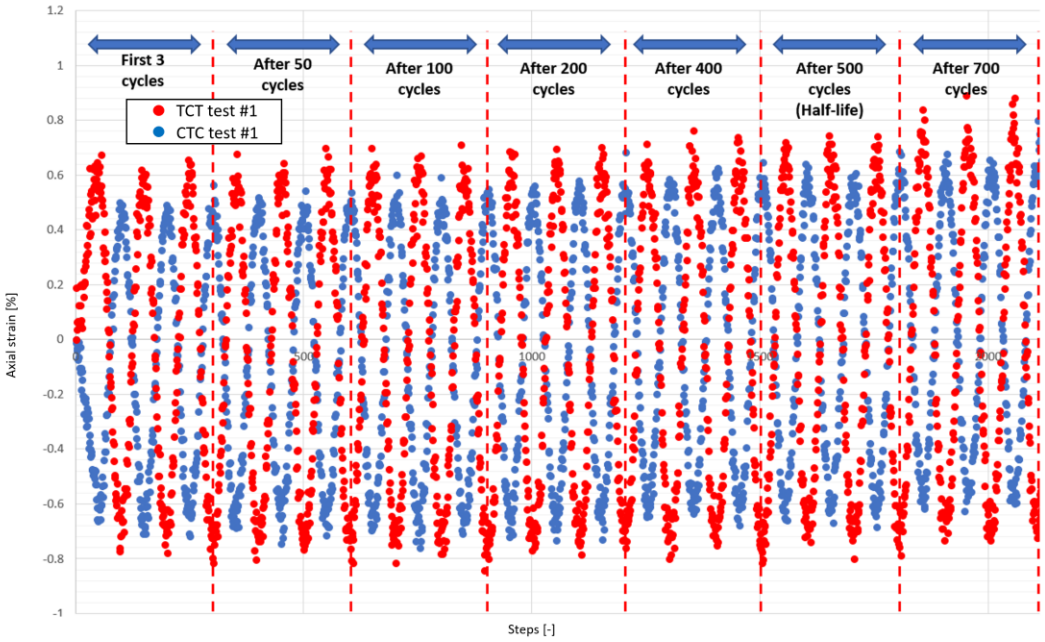

Figure 69. Axial strain progression at the notch root test for AZ31B-H24 at 80% of compressive yield equivalent fully-reversed nominal stress (3 Cycles were captured each time start at the beginning, after 50 cycles, 100 cycles, etc. Two different tests are shown; one test started with compression-tension-compression and another test started with tension-compression-tension)

It can be seen that both tests on AZ31B-H24 stabilized after the first 50 cycles and no obvious difference in axial strain measurement at the notch root over the cycles can be spotted. The TCT results seem to have higher strains over the cycles in both tension and compression in this case, however, no conclusion can be drawn without additional experiments.

The axial notch strain measurements as well as strain fields at peak tension/ compression at 60% and 80% compressive yield equivalent fully-reversed nominal stresses (94.84 MPa) are shown in Figure 70 and Figure 72. The corresponding crack initiation tests are shown in Figure 71 and Figure 73:

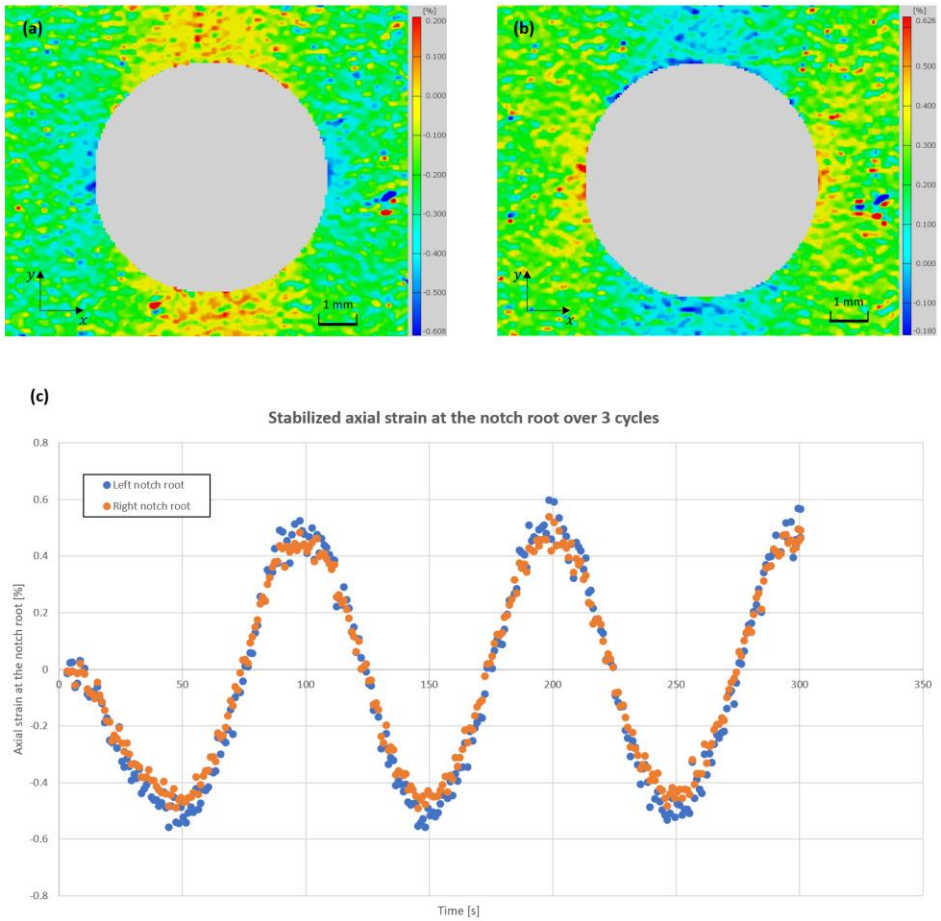

Figure 70. Stabilized strain field at (a) maximum compressive load (b) maximum tensile load and (c) axial strain at the notch root progression over 3 cycles- AZ31B-H24 @ 60% of compressive yield equivalent nominal stress (94.84 MPa) Note that the scales in (a) and (b) are different

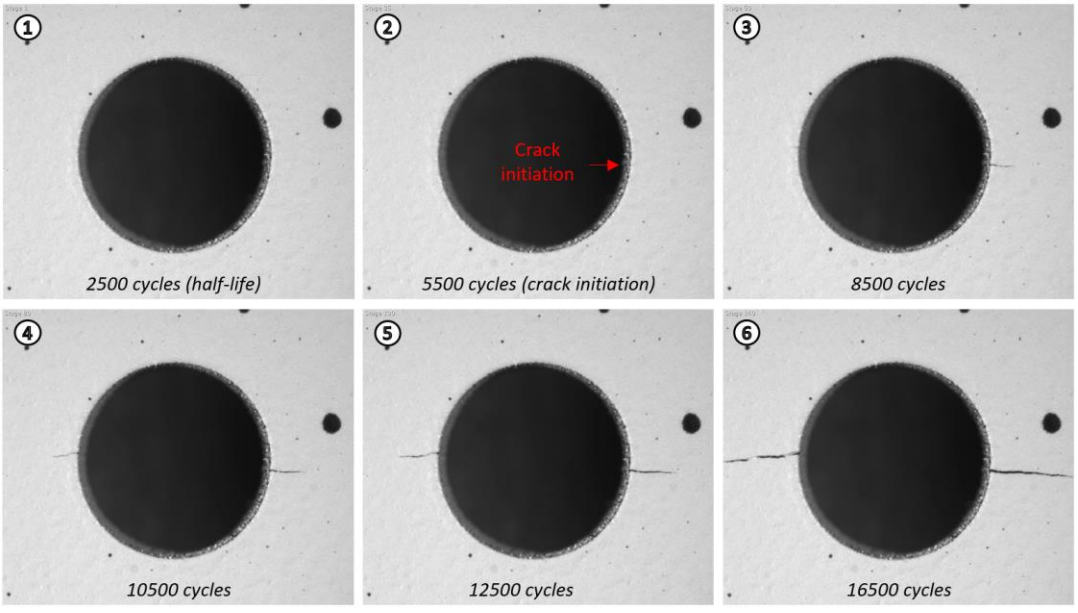

Figure 71. Crack initiation test for 60% of fully-reversed compressive yield equivalent nominal stress (94.84 MPa) – AZ31B-H24

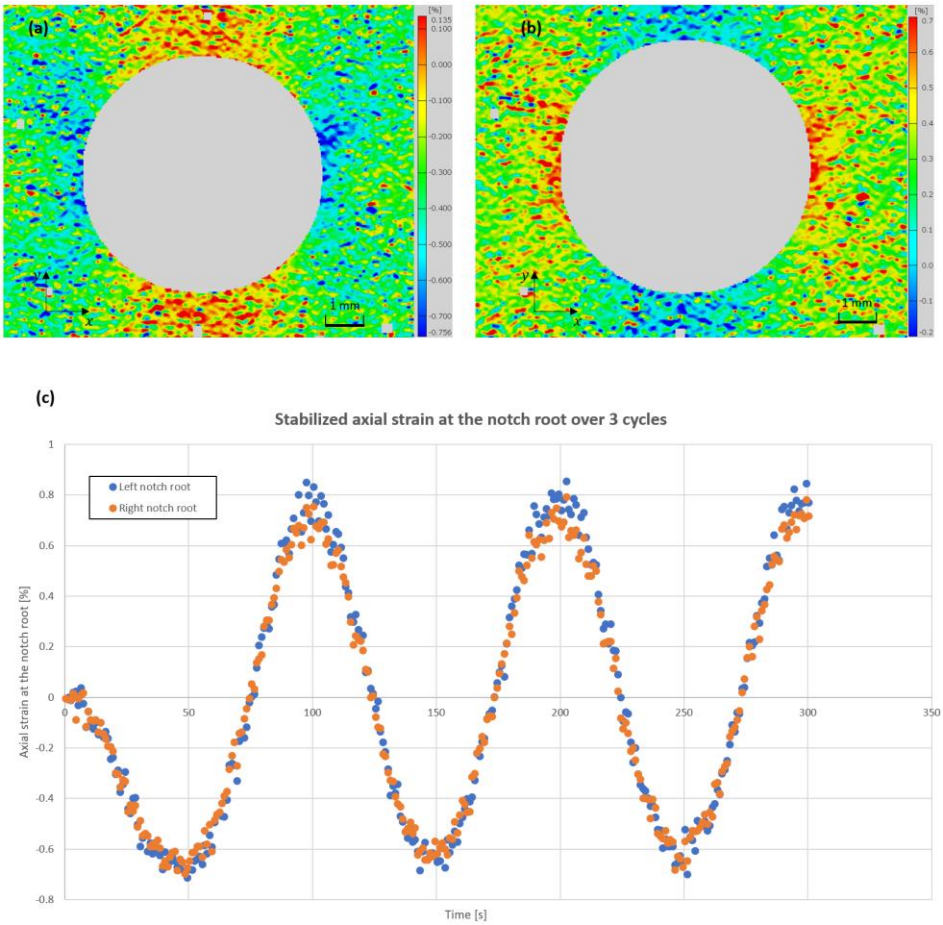

Figure 72. Stabilized strain field at (a) maximum compressive load (b) maximum tensile load and (c) axial strain at the notch root progression over 3 cycles- AZ31B-H24 @ 80% of compressive yield equivalent nominal stress (126.45 MPa) Note that the scales in (a) and (b) are different

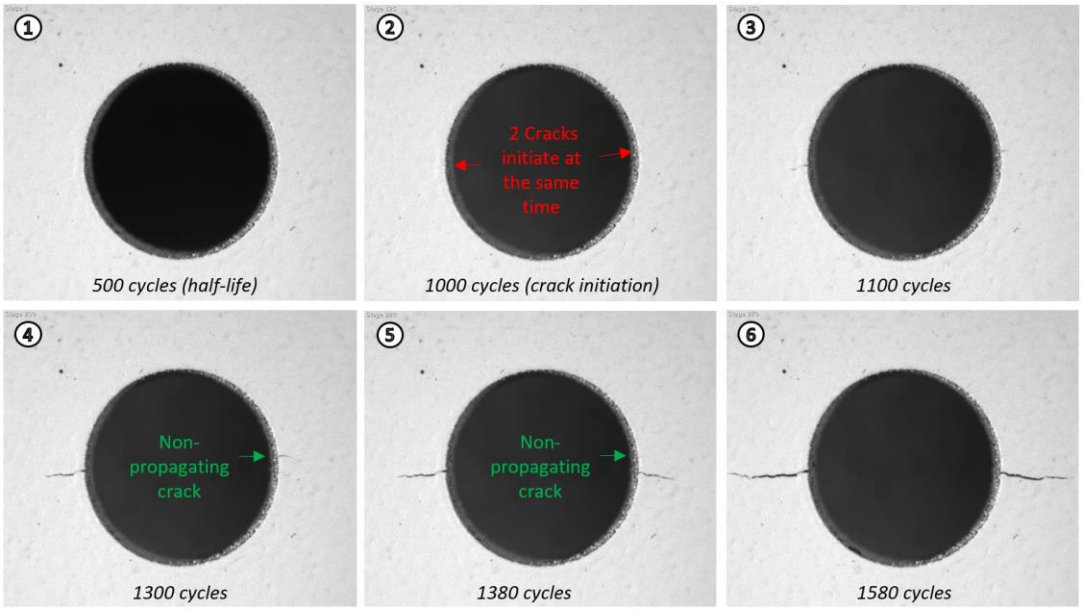

Figure 73. Crack initiation test for 80% of fully-reversed compressive yield equivalent nominal stress (126.45 MPa) – AZ31B-H24

The fatigue crack initiation lives for all the constant amplitude notched sample tests on AZ31B-H24 are summarized in Table 10:

Test #	Stress amplitude (normalized to the compressive yield) and loading sequence	Crack initiation life (crack length of ~ 100μm)
1	60%/ CTC	5300 cycles
2	60%/ CTC	5500 cycles
3	80%/ TCT	1000 cycles
4	80%/ CTC	1380 cycles
5	80%/ CTC	900 cycles
6	80%/ CTC	1120 cycles

Table 10. Fatigue crack initiation life summary on AZ31B-H24 magnesium alloy (The failure criteria for the fatigue life determination is defined by the first surface crack of a length exceed 100 μm)

3.5.3 Variable nominal stress amplitude results

The purposes of the variable nominal stress amplitude tests on notched specimens are two folds. First, the strain responses at the notch root under variable amplitude load will be used to compare with the model prediction in terms of stress-strain response prediction. Besides, the crack initiation life for these tests will be used to validate the life prediction using the fatigue models. For this reason, two types of tests were conducted to serve for each purpose. For the first type of tests, DIC was used to capture the axial strain field around the notch root after the stabilization for the given two nominal stress histories:

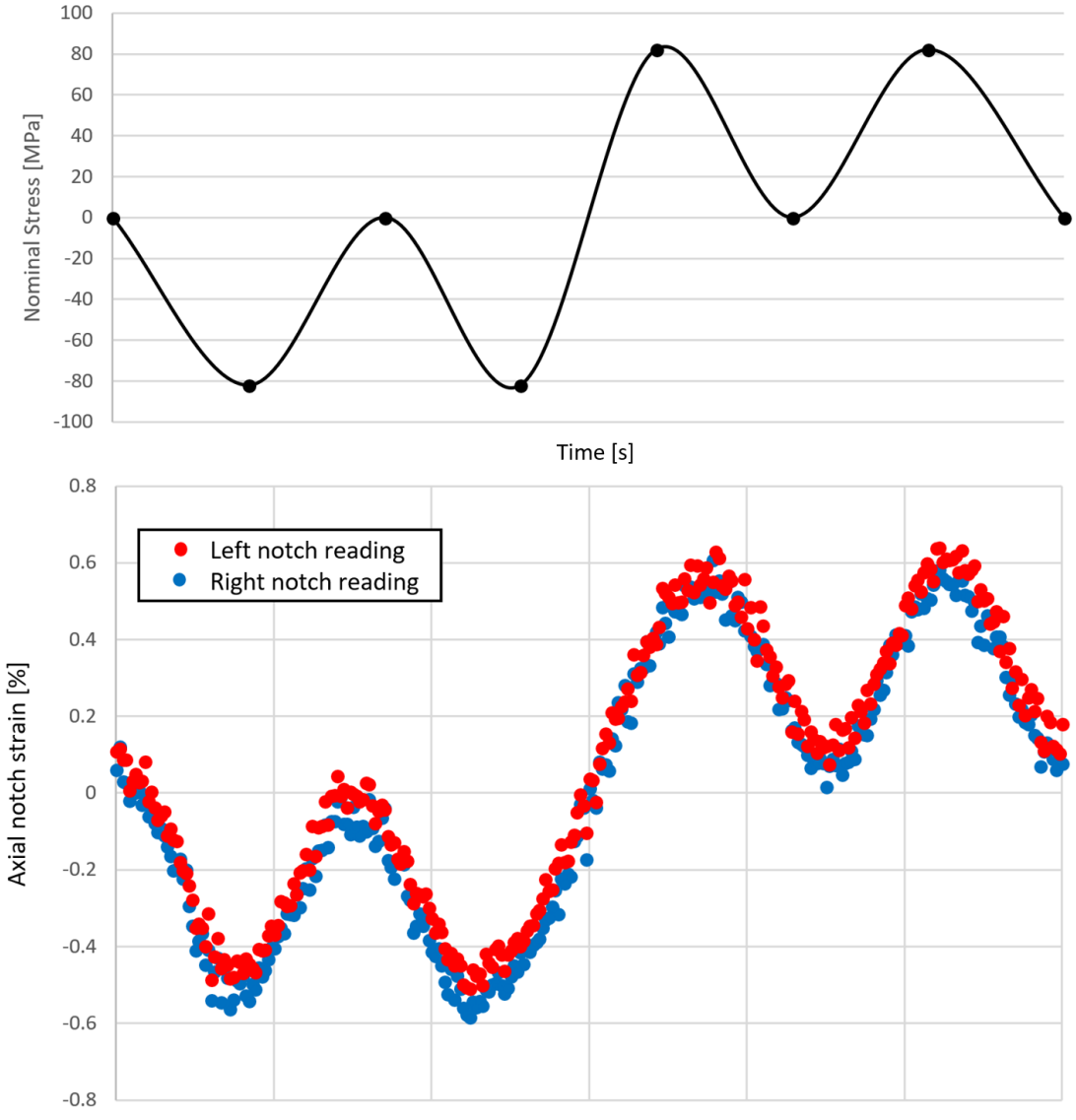

Figure 74. Variable nominal stress amplitude test on notched specimen #1- ZEK100-O (The nominal stress history is shown on the top and the axial strain at the notch root is shown at the bottom)

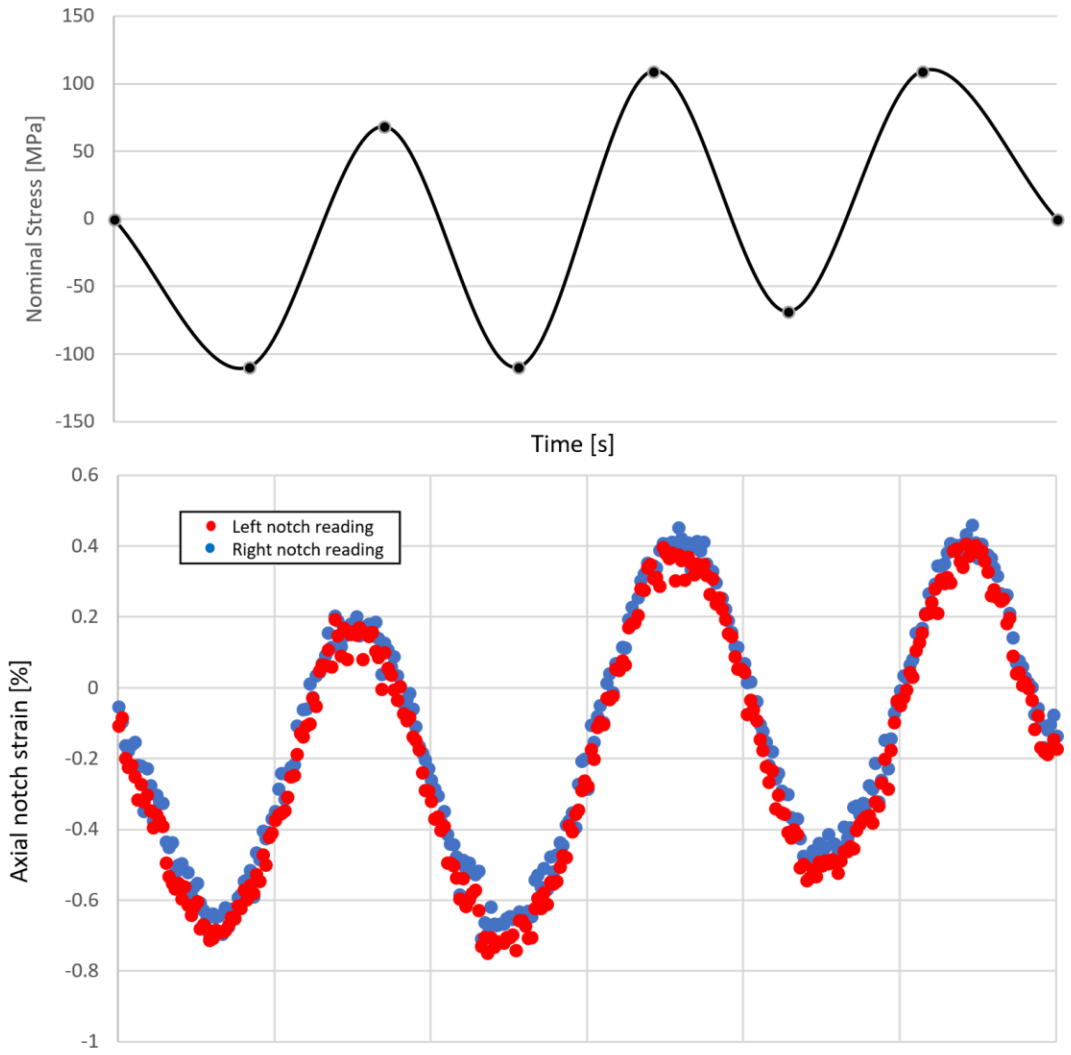

Figure 75. Variable nominal stress amplitude test on notched specimen #2- ZEK100-O (The nominal stress history is shown on the top and the axial strain at the notch root is shown at the bottom)

To get the crack initiation lives for the variable amplitude test on notched specimens, the strain field around the notch was not captured, instead, one side of the specimens were painted in white and the DIC was used to detect the crack initiation by capturing the images at the peak tensile load for each cycle, when the crack is opened. Three different nominal stress histories were tested as shown in Figure 76:

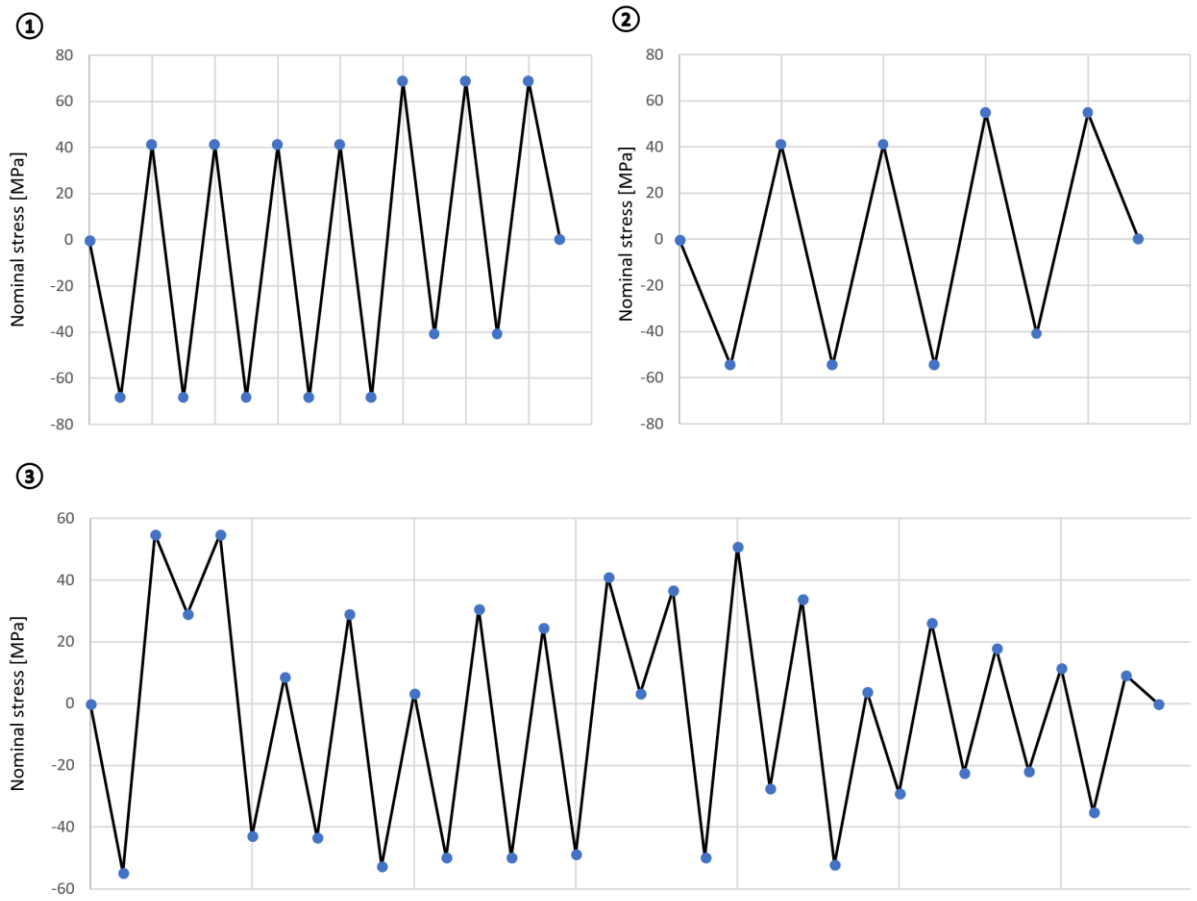

Figure 76. Nominal stress histories for variable nominal stress amplitude crack initiation tests on notched specimen- ZEK100-O

The experimental crack initiation lives correspond to the nominal stress histories provided in Figure 76 are given in Table 11:

Strain history #	Experimental life (# of blocks)
1	3980
2	23800
3	24100

Table 11. Experimental crack initiation lives correspond to the nominal stress histories provided in Figure 76 (The failure criteria for the fatigue life determination is defined by the first surface crack of a length exceeding 100 μm)

Chapter 4: Stress-strain response modelling

4.1 Phenomenological model calibration

As described in chapter 2 and shown in Table 2 and Table 3, the phenomenological stress-strain model for wrought magnesium alloys by Dallmeier, J et al. [5] requires 8 parameters in total as well as the cyclic stress-strain curve (CSSC) to model the stress-strain responses. Other than Young's modulus and the parameter R_r, which is a parameter used to increase the robustness of the model prediction, 6 other material parameters are still needed to be determined. It has been found that, all of these 6 parameters can be calculated from a single stabilized strain-controlled and fully-reversed stress-strain hysteresis loop with visible twinning exhaustion. A MATLAB routing has also been written to automatically determine these parameters given one stabilized stress-strain hysteresis loop for that material. By testing on different types of wrought magnesium alloys with the MATLAB code (AM30, AM50, ZEK100, AZ31B, etc.), the stabilized hysteresis loop of 2% strain amplitude seems to be sufficient to obtain those 6 parameters for the input and the procedure it follows will be discussed below.

Three of these parameters are tied to the inflection point on the stress versus plastic strain curve shown in Table 12:

Parameters	Unit	Descriptions
T	-	Amount of plastic strain at the inflection point of the plastic strain component
S	-	Material constant, representing the slope at the inflection point of the plastic strain component
σ_{tw}	MPa	Stress at the inflection point of the plastic strain component of the descending reversal

Table 12. Parameters used in the phenomenological model by Dallmeier, J et al. [5] which are tied to the inflection point on the stress versus plastic strain curve

Based on the total deformation plasticity theory, the plastic strain is given as:

$$\varepsilon_{ij}^{p} = \varepsilon_{ij} - \varepsilon_{ij}^{e} \tag{24}$$

Where ε_{ij}^{p} is the plastic strain component, ε_{ij} is the total strain and ε_{ij}^{e} is the elastic strain component.

And in the case of uniaxial tension/ compression:

$$\Delta\varepsilon^{p} = \Delta\varepsilon - \frac{\Delta\sigma}{E} \tag{25}$$

The downward reversal of the input 2% strain amplitude stress-strain hysteresis loop from the input is first isolated and placed in a relative coordinate system shown in Figure 77:

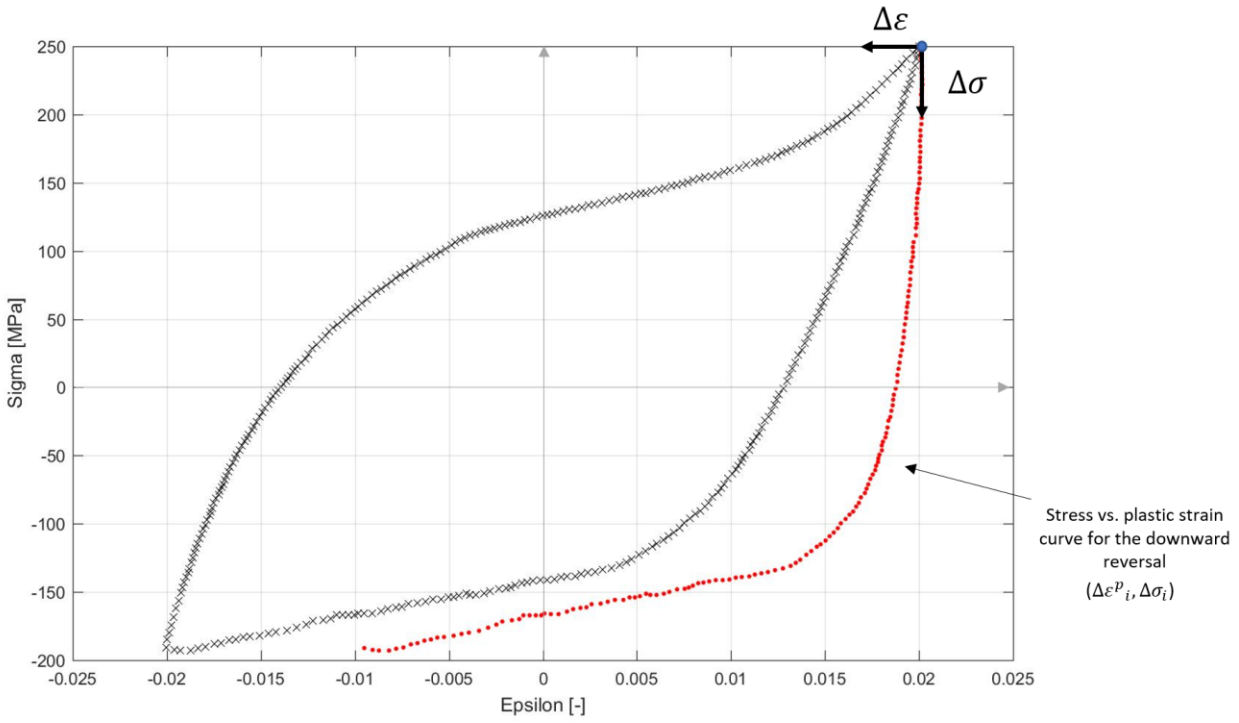

Figure 77. Stress vs. plastic strain curve for the downward reversal (red) in the relative coordinate system (top-right corner)- AZ31B-H24

The stress versus plastic strain curve is determined using Equation (25) in the relative coordinate system shown at the top-right corner for the downward reversal. The inflection point then can be found by Equation (26):

$$f''(\Delta\varepsilon^{p}) = \frac{d}{d\Delta\varepsilon^{p}}\left(\frac{d\Delta\sigma}{d\Delta\varepsilon^{p}}\right) = 0 \tag{26}$$

However, there is no mathematical expression of the stress versus plastic strain curve available to directly use with Equation (26). In addition, the incremental form of Equation (26) is also not likely to give the true inflection point of the curve due to the fact that, the experimental determined stress-strain curve for the downward reversal is generally not smooth. It would be simpler to fit a hyperbolic tangent function to the stress versus plastic strain curve then find the inflection point using Equation (26) directly, however, the strain amplitude required is much larger and it is challenging to conduct such a test without any buckling issue. Besides, the curve fitting requires a lot of tweaks to get it right and it is unlikely to work every single time.

To be able to correctly determine the inflection point of the downward reversal using a hysteresis loop of a relatively smaller strain amplitude, the method proposed is shown below:

The relation between the stress range ($\Delta\sigma_i$) and the plastic strain range ($\Delta{\varepsilon^p}_i$) is shown in Equation (27):

$$\Delta\sigma(\Delta{\varepsilon^p}_i) = \Delta\sigma_i \tag{27}$$

Where $i = 1,2,3 \ldots$

A small cluster of data with (a-1) data points ($a \ll$ the total number of data points) is chosen each time for a linear least-square regression start from the beginning and move to the end. For each set of chosen data points, the slope is given in Equation (28) and illustrated in Figure 78:

$$\frac{\delta\Delta\sigma_i}{\delta\Delta{\varepsilon^p}_i} = \frac{a\sum_{n=i}^{i+a}\Delta\sigma_n\Delta{\varepsilon^p}_n - \sum_{n=i}^{i+a}\Delta\sigma_n\sum_{n=i}^{i+a}\Delta{\varepsilon^p}_n}{a\sum_{n=i}^{i+a}\Delta{\varepsilon^p}_n{}^2 - \left(\sum_{n=i}^{i+a}\Delta{\varepsilon^p}_n\right)^2} \tag{28}$$

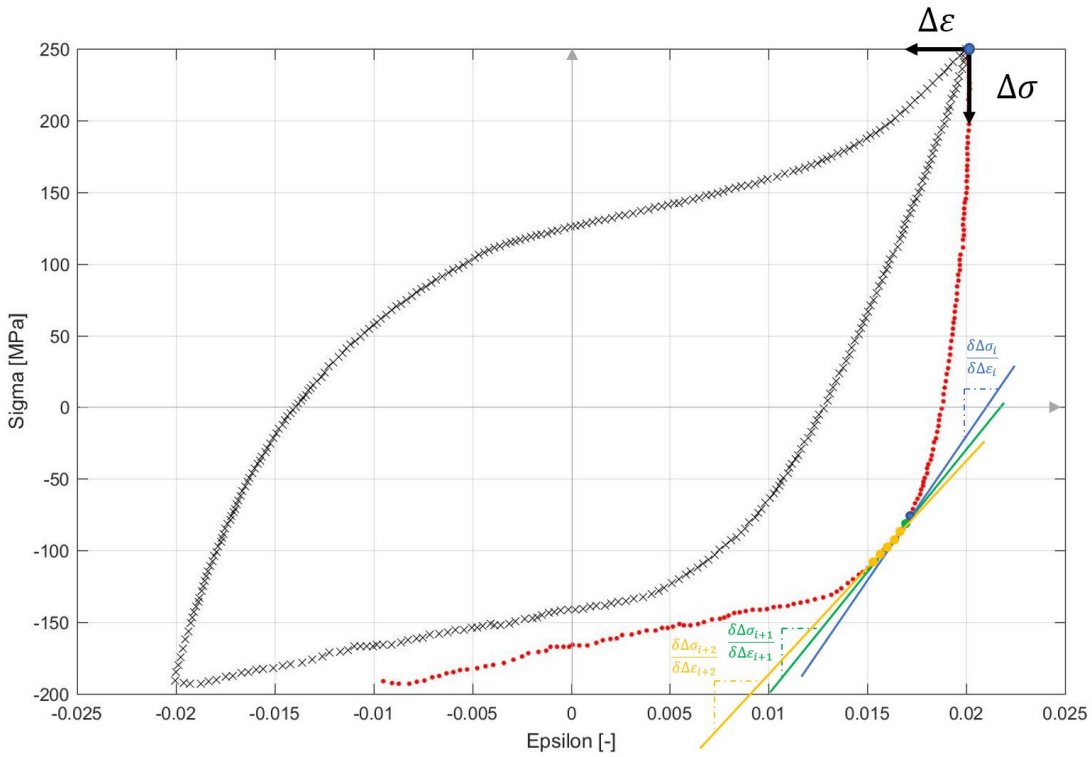

Figure 78. Illustration of finding the slopes on the stress vs. plastic strain curve (red) by performing linear least-square regressions on each set of data points - AZ31B-H24

In order to find the inflection point, the same operation described above is repeated but on the $\frac{\delta\Delta\sigma_i}{\delta\Delta{\varepsilon^p}_i}$ versus $\Delta{\varepsilon^p}_i$ curve, given in Equation (29):

$$\frac{\delta^2\Delta\sigma_i}{\delta\Delta{{\varepsilon^p}_i}^2} = \frac{a\sum_{n=i}^{i+a}\frac{\delta\Delta\sigma_n}{\delta\Delta\varepsilon_n}\Delta{\varepsilon^p}_n - \sum_{n=i}^{i+a}\frac{\delta\Delta\sigma_n}{\delta\Delta\varepsilon_n}\sum_{n=i}^{i+a}\Delta{\varepsilon^p}_n}{a\sum_{n=i}^{i+a}\Delta{\varepsilon^p}_n{}^2 - \left(\sum_{n=i}^{i+a}\Delta{\varepsilon^p}_n\right)^2} \tag{29}$$

The change of plastic strain corresponds to the inflection point $\Delta{\varepsilon^p}_{\text{inflection}}$ can be determined by finding the point where $\frac{\delta^2\Delta\sigma_i}{\delta\Delta{{\varepsilon^p}_i}^2}$ changes sign. Finally, all three parameters described in Table 12 then can be determined simultaneously in which T is double the value of $\Delta{\varepsilon^p}_{\text{inflection}}$, S is the slope at the inflection point and σ_{tw} is the global stress value correspond to the inflection point:

$$T = 2\Delta{\varepsilon^p}_{\text{inflection}} \tag{30}$$

$$S = \frac{\delta \Delta \sigma_{\text{inflection}}}{\delta \Delta \varepsilon^{p}{}_{\text{inflection}}} \tag{31}$$

$$\sigma_{tw} = \Delta\sigma(\Delta \varepsilon^{p}{}_{\text{inflection}}) \tag{32}$$

As described by Dallmeier et al. [5] , $\sigma_{p,up}$ and $\sigma_{p,down}$ correspond to the Pseudo-elastic cut-off stress for ascending and descending reversals, respectively and can be identified as the relative stress in the considered relative coordinate system at which the reversal considerably deviates from linear elastic behavior (20% deviation in stress). The determination of $\sigma_{p,up}$ and $\sigma_{p,down}$ parameters is illustrated in Figure 79:

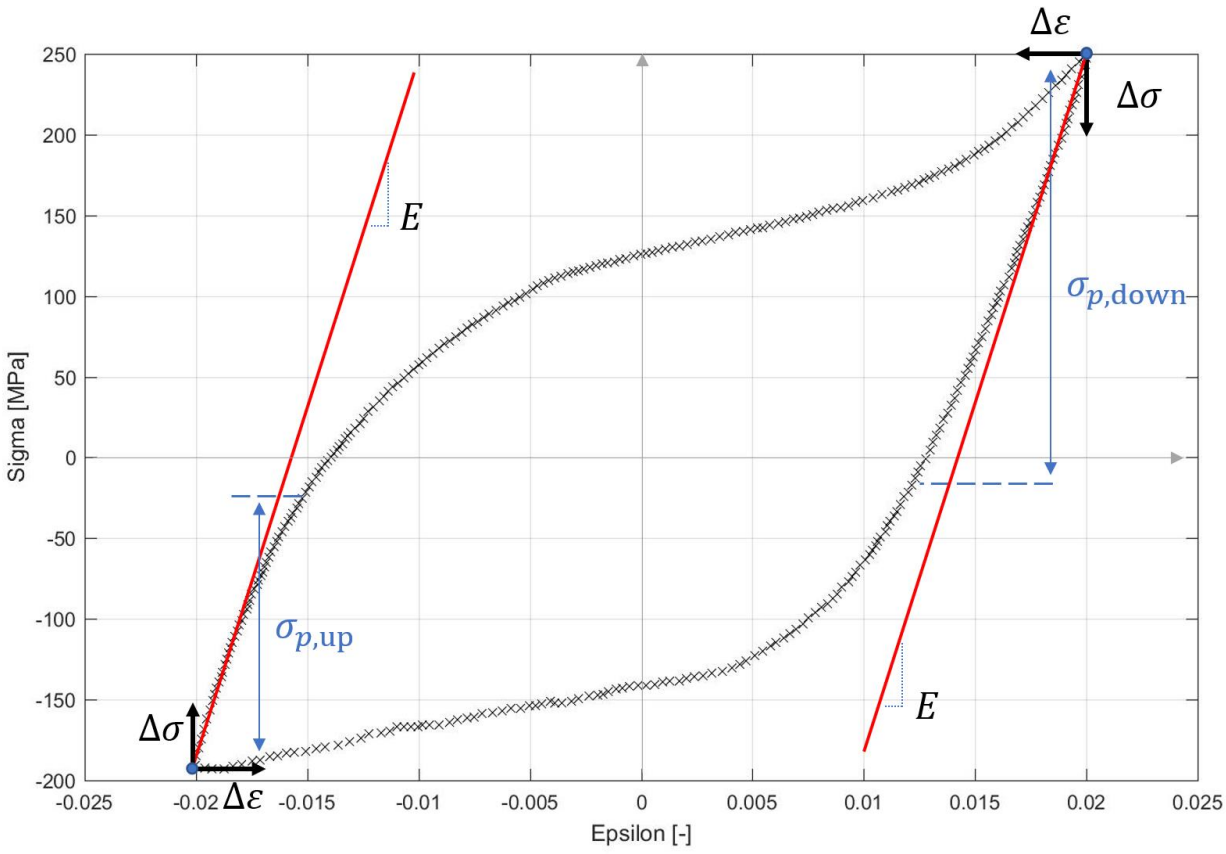

Figure 79. Illustration of the determination of parameters $\sigma_{p,up}$ and $\sigma_{p,down}$ – AZ31B-H24

The determination of the material constant P, which represents the slope of the pseudo-elastic strain component is not mentioned by Dallmeier et al [5] , however, based on Figure 6, the slope of the pseudo-elastic strain seems to be close to the inverse of Young's modulus and it has been proved to work on both ZEK100-O and AZ31B-H24.

Lastly, the R_r value, which enables the correct adaption of the adaption of the memory factors, so that the shape of the stress-strain curves coincides with experiments most accurately as described by Dallmeier et al. [5] modifies the transition of the stress-strain curve from elastic to plastic behavior as shown in Figure 80:

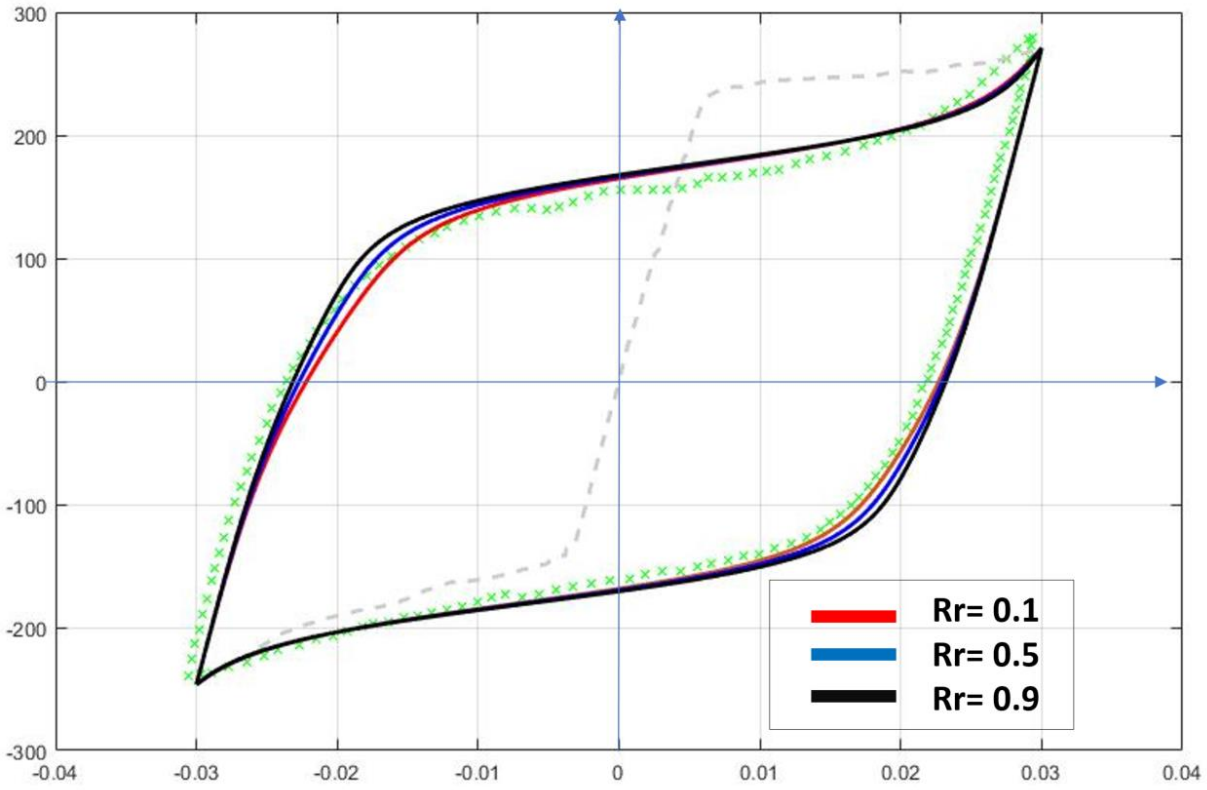

Figure 80. The effect of Rr value on predicted stress-strain curve for AM30 Mg alloy at 3% strain amplitude

The parameters determined for ZEK100-O and AZ31B-H24 is summarized in:

Parameters	Unit	ZEK100-O	AZ31B-H24
E	GPa	44.08	43.70
P	-	0.003571	0.00229
$\sigma_{p,up}$	MPa	97	157
$\sigma_{p,down}$	MPa	158	231
T	-	0.0558	0.02523
S	-	36.086	37.84133
σ_{tw}	MPa	-161.113	-146.71593
R_r	-	0.8	0.9

Table 13. Phenomenological model parameters determined for ZEK100-O and AZ31B-H24

4.2 Hysteresis loop modeling of smooth specimens under uniaxial loading

To model the stress-strain responses for a given strain history using the phenomenological model by Dallmeier et al. [5] , the rain-flow counting method by Matsuishi et al. [87] -[89] is used to track the material memory and identify the closed stress-strain hysteresis loops. However, due to the limitations of this phenomenological model in which the envelope hysteresis has to be identified prior to the simulation in order to define the shapes of the inner hysteresis loops, the strain history has to be rearranged to start and end with the maximum absolute value, shown in Figure 81:

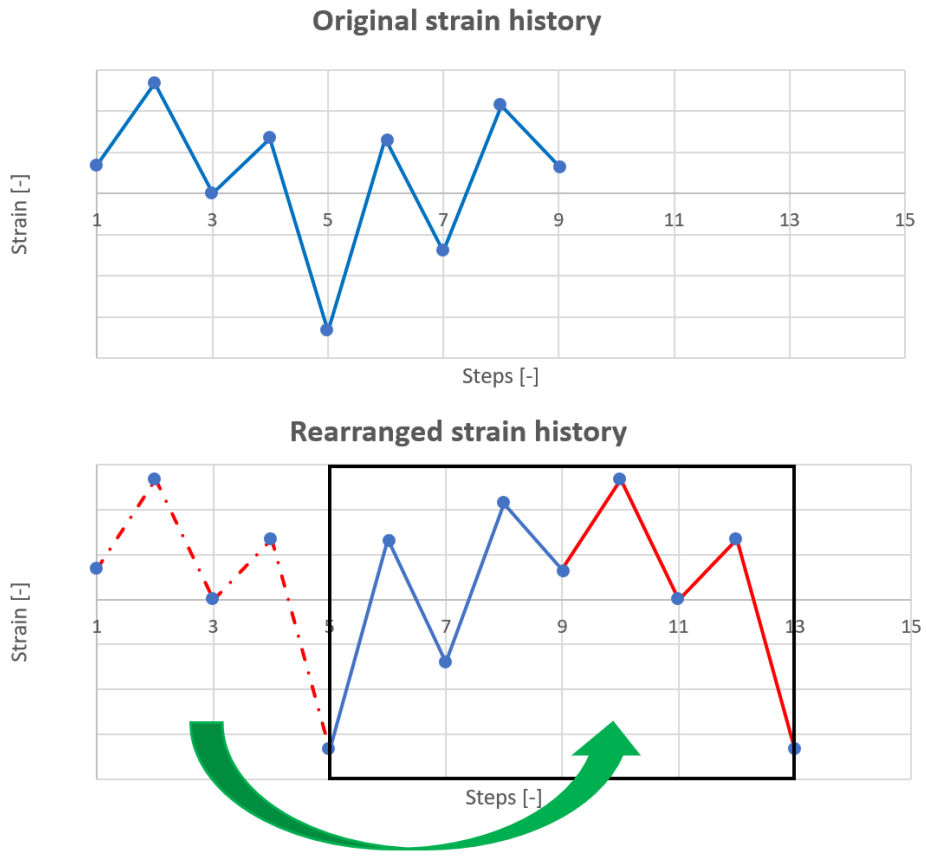

Figure 81. Re-arrangement of the strain history to start/end from the absolute maximum value

To match the model prediction with the material behavior, the reversing points of the fully-reversed-in-strain envelope hysteresis loop have to coincide with the CSSC. Therefore, the simulation starts with the modeling of the envelope hysteresis loop, which is the fully-reversed (strain) hysteresis loop with the strain amplitude equals the value at the end of the first segment from the rearranged strain history, which is shown as the red curve in Figure 82:

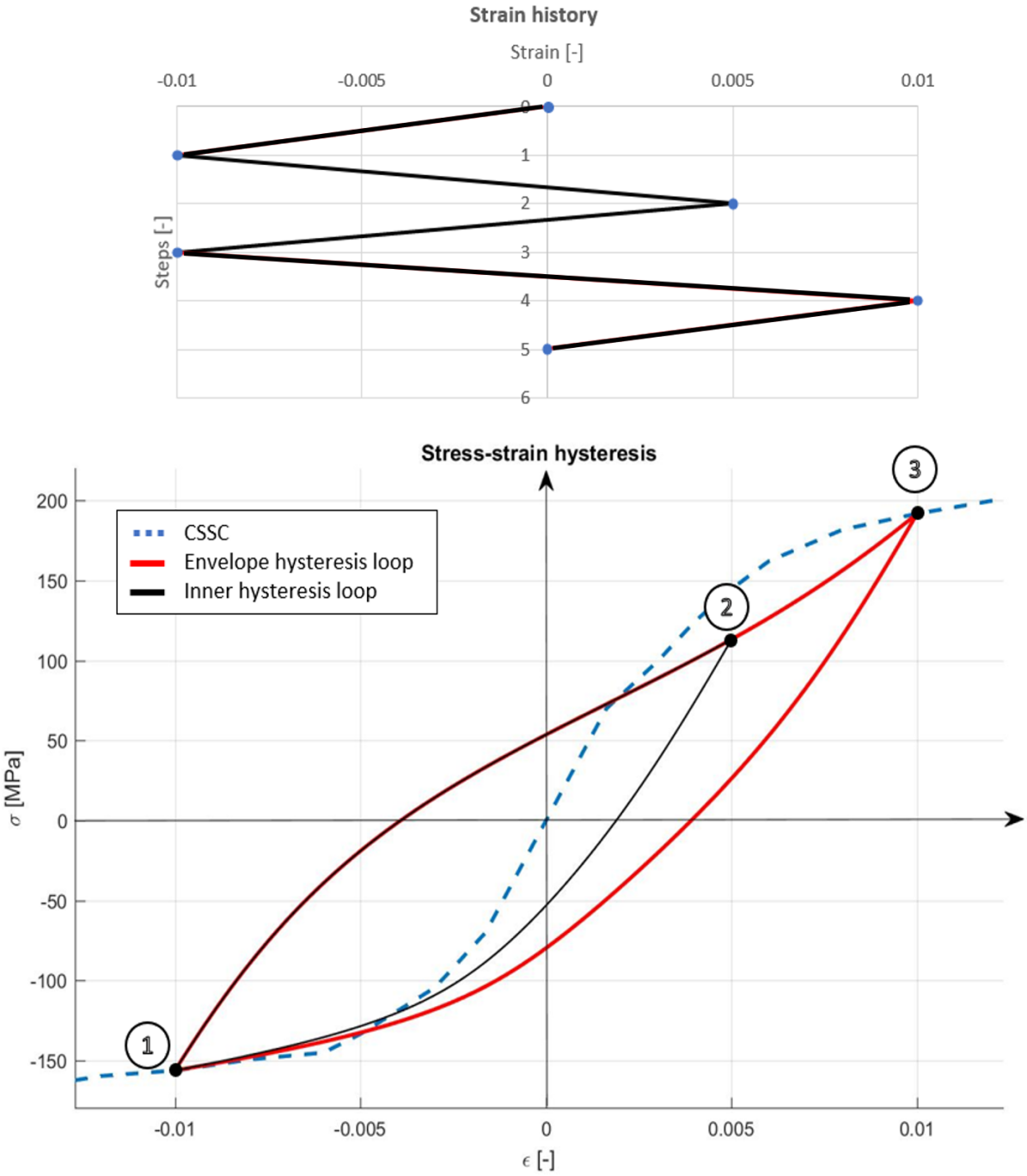

Figure 82. Smooth sample analysis example 1- modeling of the hysteresis loops for the given strain history (ZEK100)

Following the material cyclic stress-strain curve, which is the blue dashed lines in Figure 82 on both tensile and compressive branches to the absolute strain value at the end of the first strain history segment, the stress and strain values at both of the reversing points on the envelope hysteresis loop as well as the strain and stress ranges can be obtained. The envelope hysteresis loop than can be

constructed using the phenomenological model which provides the shape of the stress-strain path to follow for the next reversal, shown as the red curve in the stress vs. strain plot in Figure 82. In spite of the envelope hysteresis loop is always fully-reversed in strain, the largest hysteresis loop for the provided strain history does not have to be fully-reversed in strain since the envelope hysteresis loop is solely used to set the material memory and indirectly defining the shapes of the subsequent stress-strain paths enclosed.

By knowing the stress-strain path from the envelope hysteresis loop, the second reversal is originated from where the first reversal ends, shown as point 1 in Figure 82 and following the stress-strain path alone the envelope hysteresis loop (between point 1 to point 3) to the next strain value on the strain history shown as point 2, known that the stress and strain value will coincide with the CSSC when it reaches point 3 eventually.

To fulfill the material memory, the stress-strain responses will follow the superior reversals after each completion of inner cycles. As an example, after the completion of the cycle between point 1 and point 2 in Figure 82 (The hysteresis loop in black), the stress-strain curve between point 1 and point 3 has been followed started from point 1. Not to mention that, even though the hysteresis loop between point 1 and point 3, which happens to be the envelope hysteresis loop, in this case, was constructed at the very beginning of the simulation, it only serves the purpose of tracking the material memory and the actual hysteresis loop between point 1 and point 3 is modeled after the hysteresis loop in between point 1 and point 2 based on the rain-flow counting method.

Another example is shown in Figure 83, the largest hysteresis loop for the given strain history is not fully reversed (Inner hysteresis loop 1), however, the stress-strain path from point 1 to point 3 is still following the envelope hysteresis loop shown as the red dashed line from point 1 to point 2. In addition, the green hysteresis loop between point 6 and 7 (Inner hysteresis loop 3) has been closed first based on the rain-flow counting method. To fulfill the material memory, the stress-strain path between point 6 and point 4 then followed the stress-strain path for the superior reversals, which is the curve between point 5 and point 4. Similarly, after the closure of the purple hysteresis loop at point 4, the stress-strain path between point 4 and point 1 is following the path of its superior reversal, which is the curve in between point 3 and point 1.

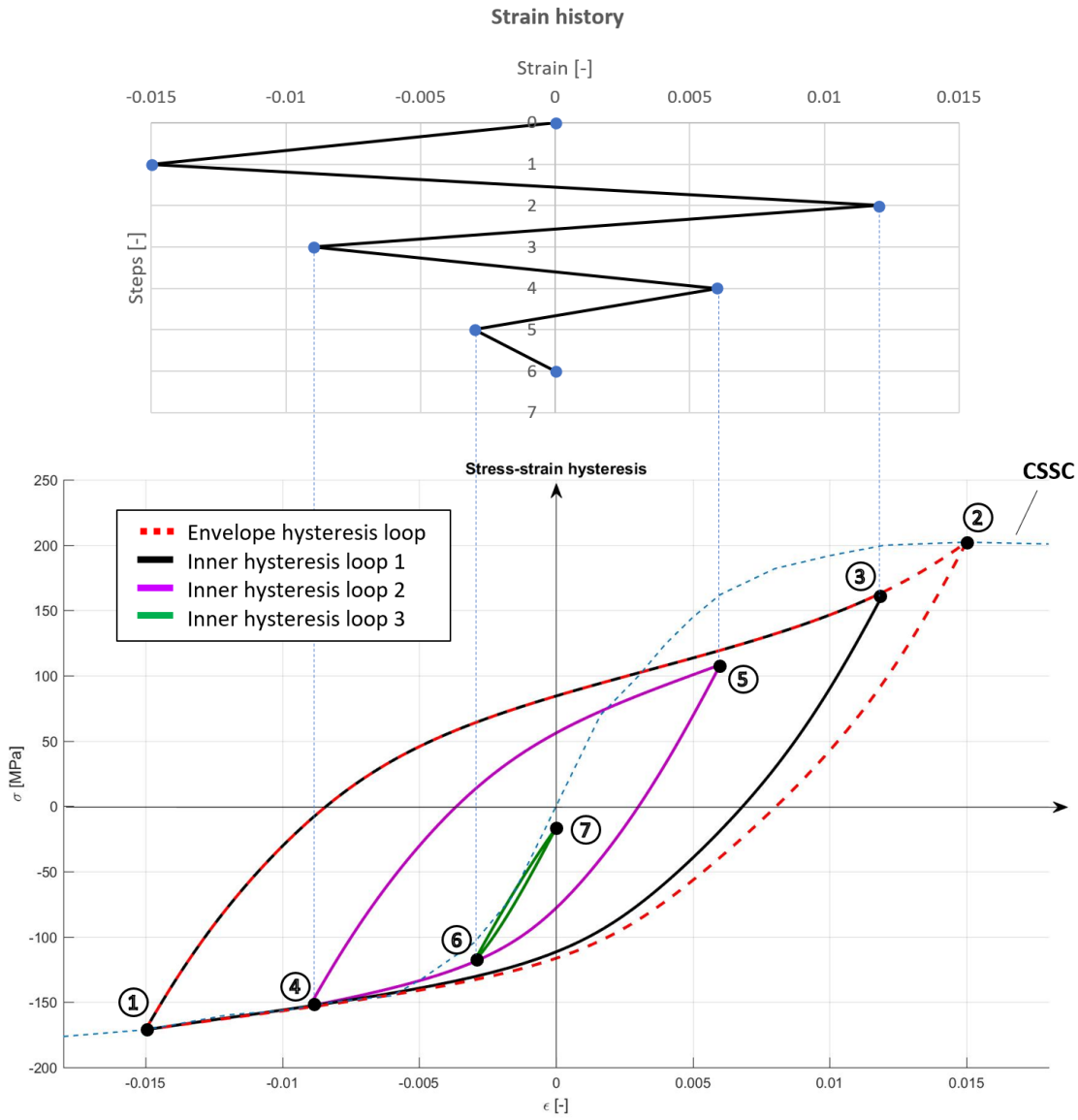

Figure 83 Smooth sample analysis example 2- modeling of the hysteresis loops for the given strain history (ZEK100)

To efficiently track the material memory throughout the simulation using the phenomenological model, the stress-strain curve for each incomplete cycle is stored in an array since each of them have a different shape and the simulation will always pick the most recent stress-strain curve entry to follow. Once a cycle is completed, the most recent entry of the stress-strain curve will be removed and the stress-strain path after will be automatically started to follow the stress-strain path of its superior reversal.

To check the goodness of the model predictions, stabilized stress-strain hysteresis loops for the constant amplitude strain-controlled tests on ZEK100-O and AZ31B-H24 have been used to verify the model predictions, shown in Figure 84 and Figure 85:

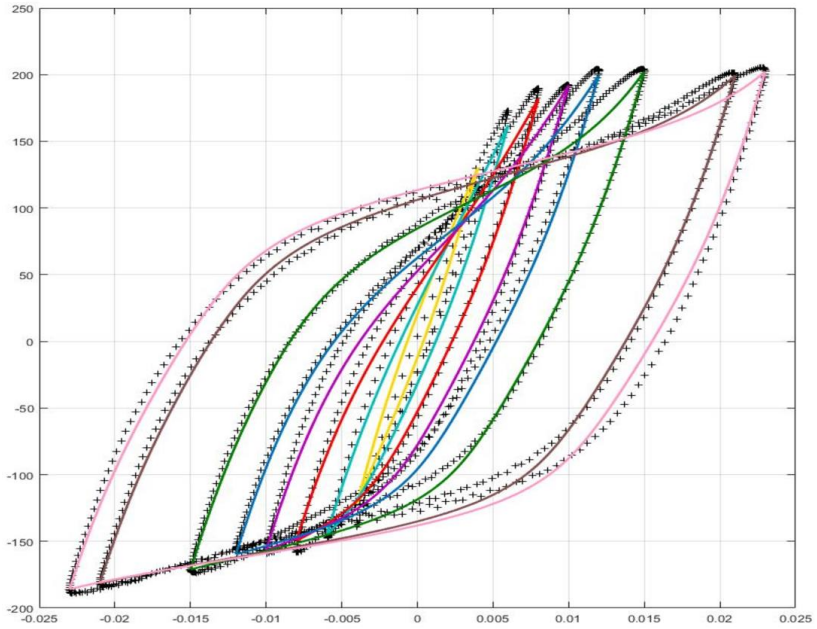

Figure 84. Stress-strain response comparison between experimental results and the model predictions for ZEK100.

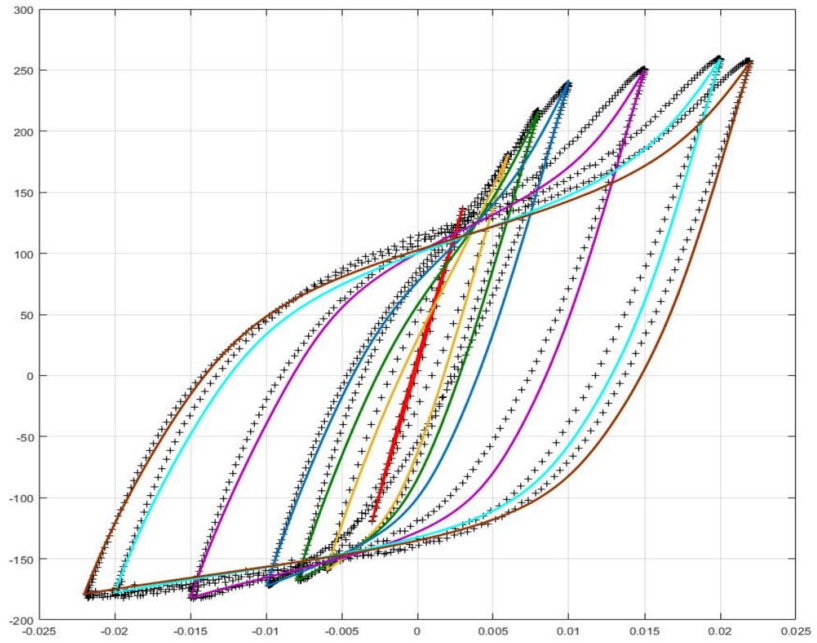

Figure 85. Stress-strain response comparison between experimental results and the model predictions for AZ31B-H24.

The solid lines are the stress-strain response predicted by the model and markers are the experimental results. It can be seen that the phenomenological model performed reasonably well for both ZEK100-O and AZ31B-H24.

The stabilized stress-strain hysteresis loops for the variable amplitude strain-controlled tests for 4 different strain histories shown in Figure 56 - Figure 59 on ZEK100-O are compared against the model predictions, shown in Figure 86 - Figure 89:

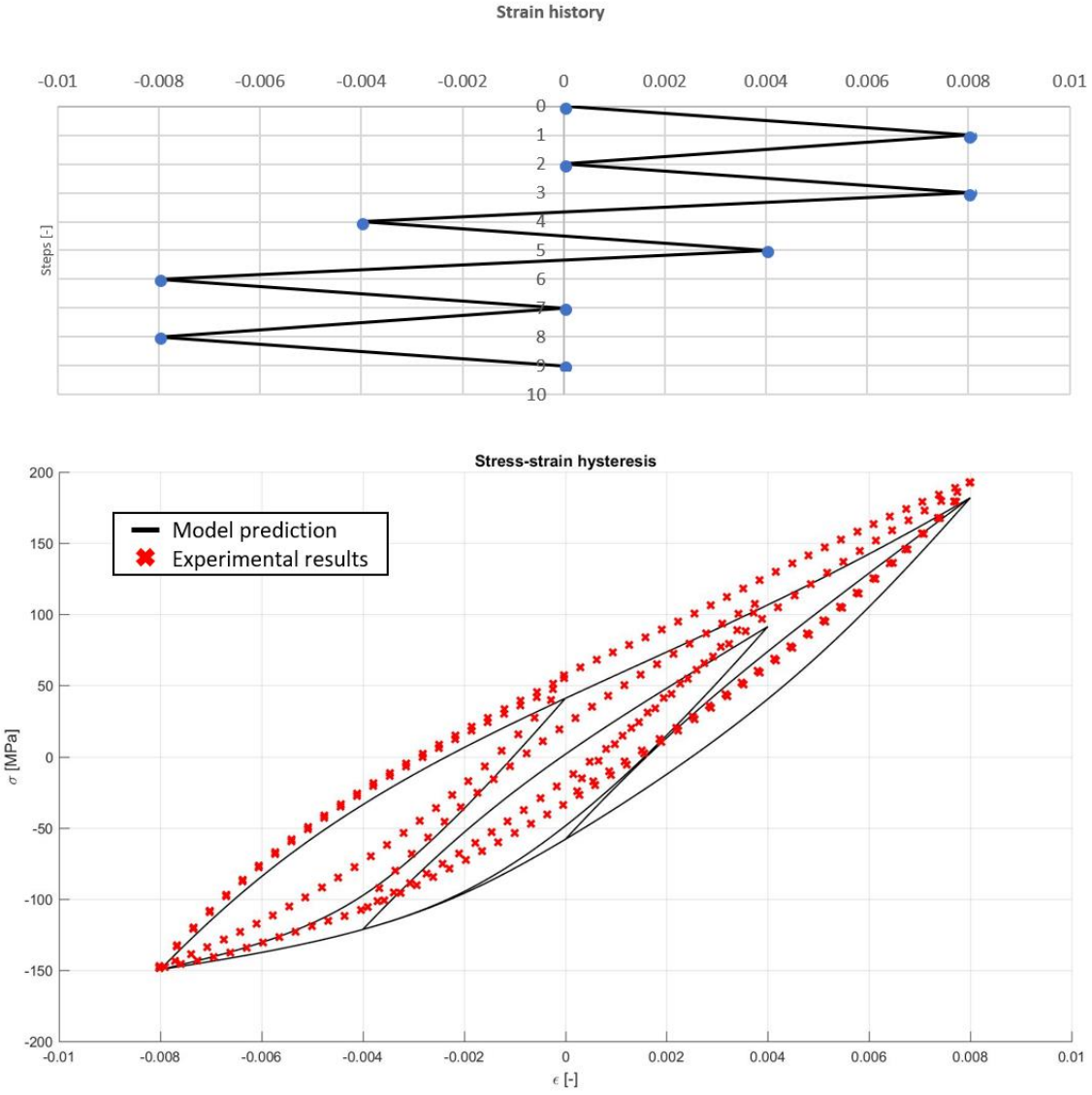

Figure 86. Variable amplitude stress-strain response (load history #1) comparison between experimental results and the model predictions for ZEK100-O

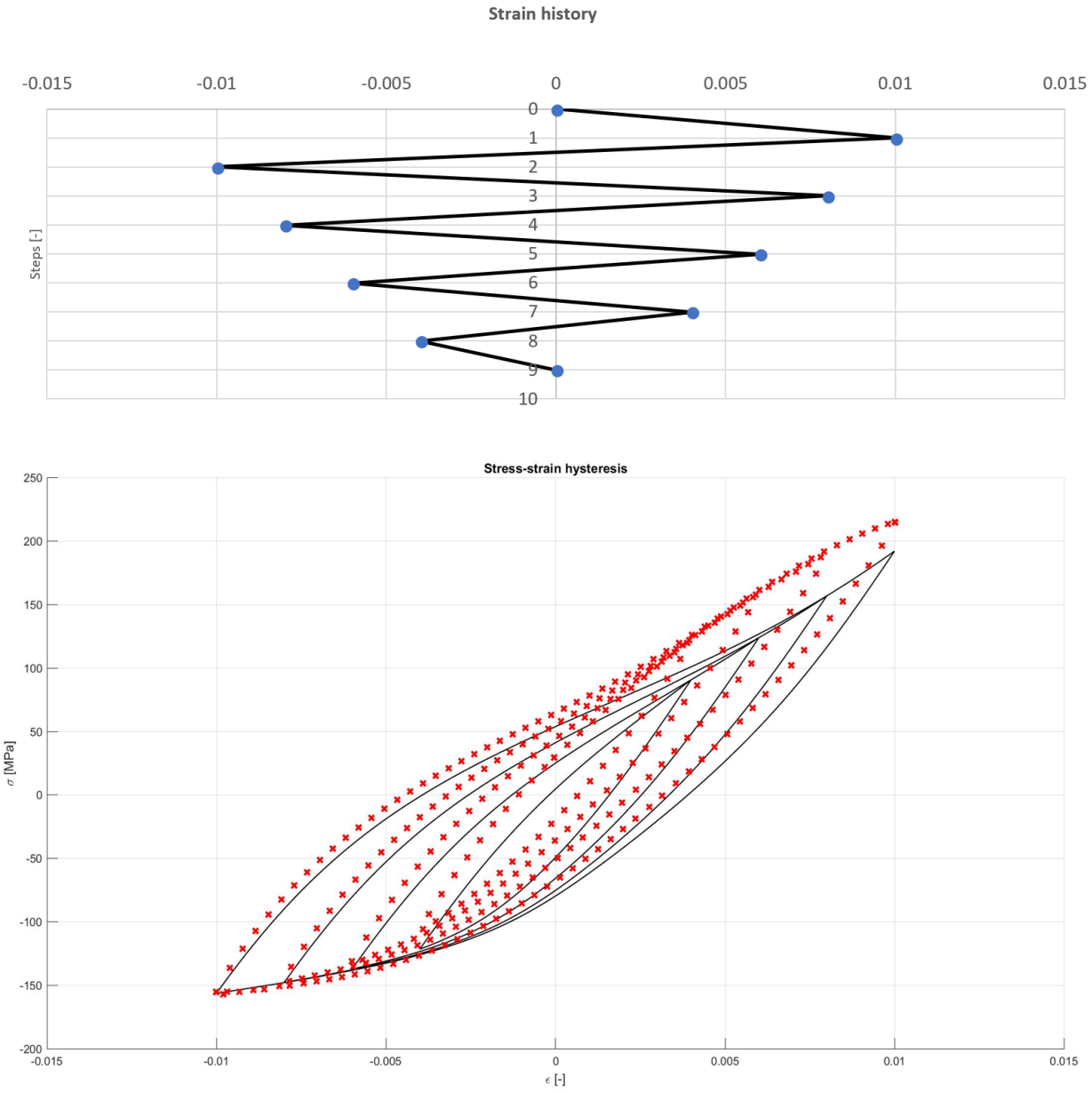

Figure 87. Variable amplitude stress-strain response (load history #2) comparison between experimental results and the model predictions for ZEK100-O

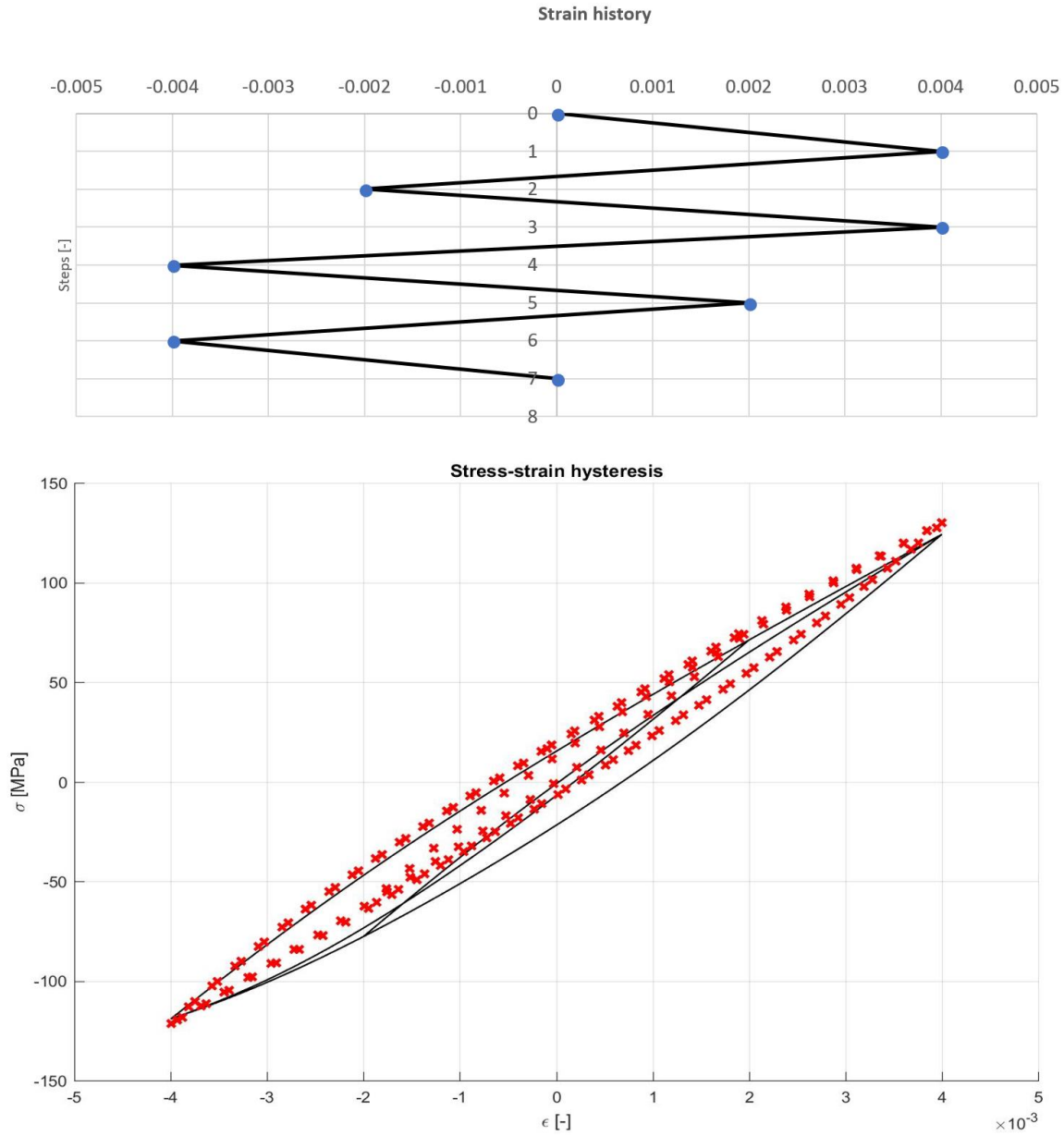

Figure 88. Variable amplitude stress-strain response (load history #3) comparison between experimental results and the model predictions for ZEK100-O

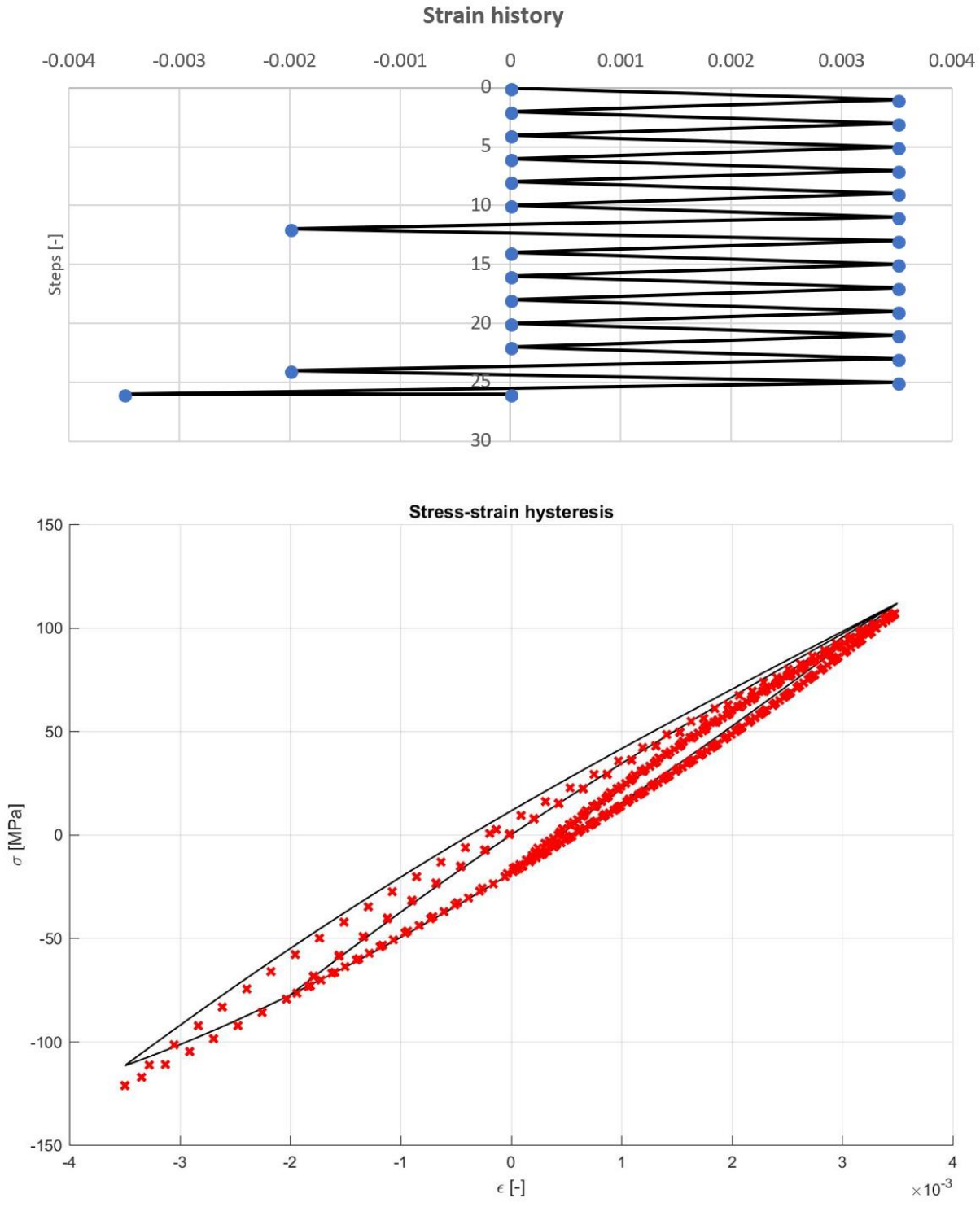

Figure 89. Variable amplitude stress-strain response (load history #4) comparison between experimental results and the model predictions for ZEK100-O

Although there are some deviations between the model predicted and the experimental stress-strain hysteresis loops, the phenomenological model performs reasonably well on the variable amplitude stress-strain hysteresis loops prediction on ZEK100-O for the given strain histories.

4.3 Notch root stress-strain response modeling under uniaxial loading

4.3.1 Approximation method using Neuber's rule

Knowing the local stress-strain responses at the vicinity of the notch root is vital to estimate the fatigue life for a mechanical component under cyclic loading. As the most frequently used approximation method, Neuber's rule is capable to analyze the local plasticity at the vicinity of the notch root with a reasonable accuracy.

The Neuber's rule states that the geometric mean of the stress and strain concentration factors will remain equal to the elastic stress concentration factor during the plastic deformation [75] . In the case of cyclic loading, the Neuber's rule is given as:

$$k_t = \sqrt{k_\sigma k_\varepsilon} \tag{33}$$

$$k_\sigma = \frac{\Delta\sigma}{\Delta S} \tag{34}$$

$$k_\varepsilon = \frac{\Delta\varepsilon}{\Delta e} \tag{35}$$

$$e = \frac{\Delta S}{\Delta E} \tag{36}$$

Substitute Equation (34-36) into Equation (33) gives:

$$\Delta\sigma\Delta\varepsilon = \frac{(k_t\Delta S)^2}{E} = const. \tag{37}$$

In order to predict the notch responses for a given nominal load history, the Neuber's rule has been applied sequentially to each of the stress-strain curves starts with the experimentally determined cyclic stress-strain curve shown in Figure 90. A new relative coordinate system is placed on each reversing point so that the following stress-strain path extends into the first quadrant of the coordinate system. The Neuber's hyperbola Equation (37) is also constructed in the same relative coordinate system so that, according to the Neuber's rule, the intersection between the stress-strain curve and Neuber's hyperbola

gives the stress and strain value at the notch root correspond to the applied nominal stress. It is worth to mention that, even though the first loading segment is going into compression in Figure 90, the changes of strain and stress ($\Delta\varepsilon$ and $\Delta\sigma$) are always remaining positive.

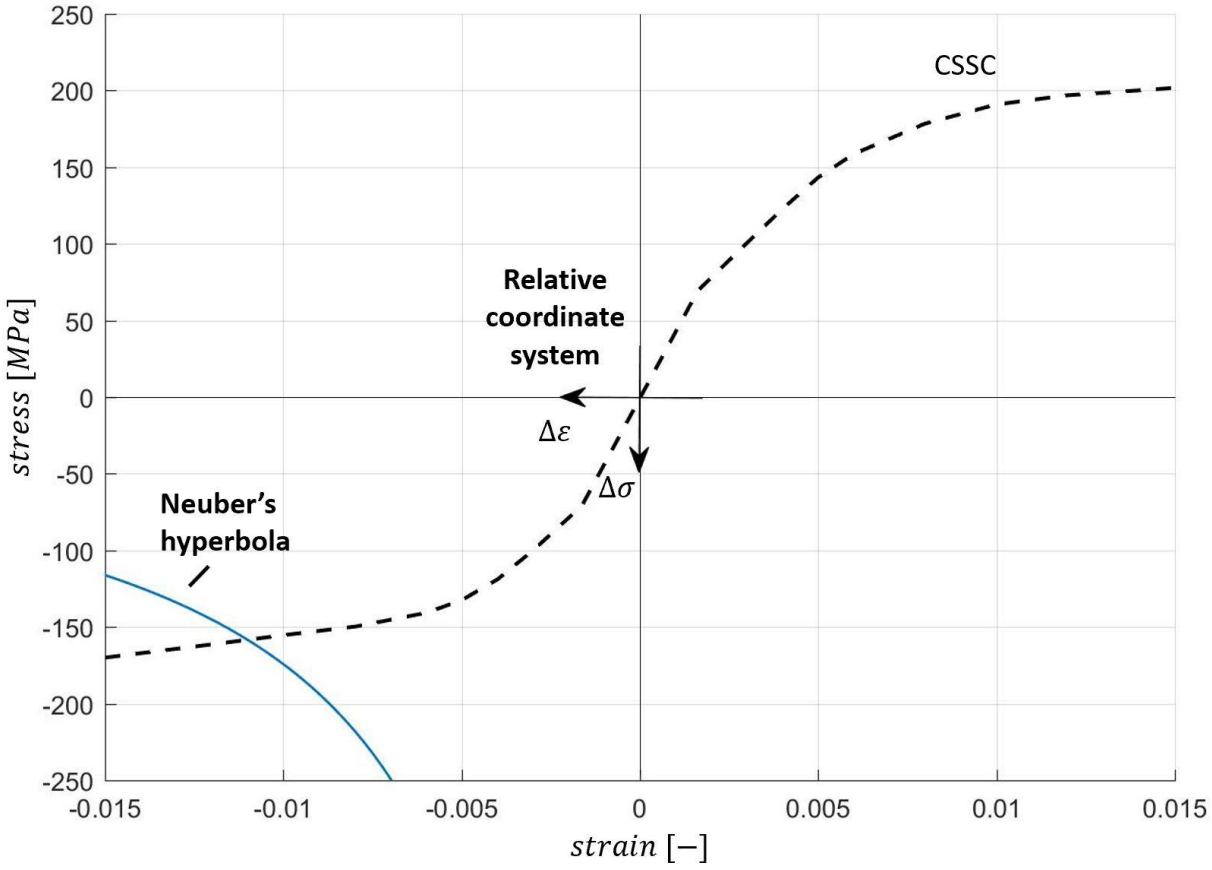

Figure 90. Application of Neuber's rule on the cyclic stress-strain curve for the first reversal going into compression

To apply Neuber's rule to the second reversal, it is essential to determine the corresponding stress-strain curve in advance. Unlike the Ramberg-Osgood equation [69] accompanied with the Masing hypothesis [70] , the phenomenological model [5] requires the stress and strain ranges as well as the stress and strain value at the reversing point for each reversal in order to properly model the asymmetric behavior of magnesium alloys and the equation of the stress-strain curve is not readily available. However, what is known at this point is, the starting point of this reversal is on the cyclic stress-strain curve and the point with double the strain range ($2\Delta\varepsilon_{\text{first reversal}}$) of the first reversal will

also be on the cyclic stress-strain curve on the opposite side; In the case of Figure 90, the tensile branch of the cyclic stress-strain curve. Therefore, the most natural selection of the stress-strain curve correspond to this reversal is the branch of fully reversed (R_ε =-1) hysteresis loop with the strain amplitude equivalent to the change of strain for the first reversal ($\Delta\varepsilon_{\text{first reversal}}$). The upward reversal of the hysteresis loop is taken in Figure 91 since the first reversal is going into compression first. In the case of the first reversal is going into tension first, the downward reversal will be taken as the stress-strain path for the corresponding second reversal. Knowing the stress and strain values at the reversing points on the global coordinate from the first application of the Neuber's rule on the cyclic stress-strain curve and stress range which is from the cyclic stress-strain curve given the strain range to be twice of the first reversal ($2\Delta\varepsilon_{\text{first reversal}}$), it is possible to construct the corresponding stress-strain curve of this reversal using the phenomenological model, shown as the red curve in Figure 91.

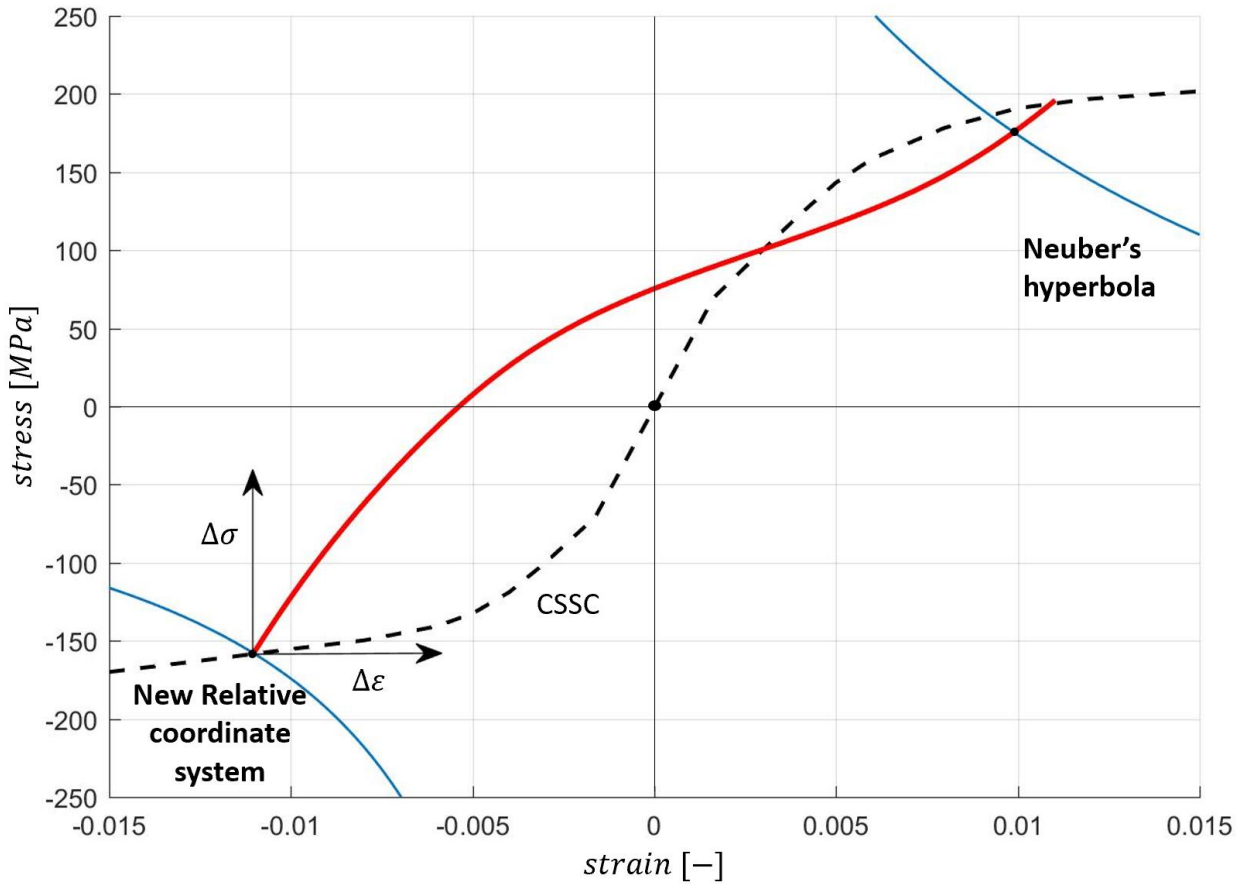

Figure 91. Application of Neuber's rule for the second reversal (The stress-strain curve is created using the phenomenological model [placeholder])

By having the stress-strain curve for the second reversal, a new coordinate system is placed at the first reversing point as shown in Figure 91. The intersect between the new Neuber's hyperbola in the relative coordinate system and the stress-strain curve is then determined. After the conversion back to the global coordinate system, the stress and strain response correspond to the remote load is approximated.

Departure from the cyclic stress-strain curve after the second reversal, the stress-strain path to be followed is remaining unknown since the material at the vicinity of the notch root is neither stress controlled nor strain controlled. However, experimental results on notched specimens under fully reversed nominal load shown that the material at the vicinity of the notch root stabilizes after several applications of the load, shown in Figure 62 and Figure 69. One reason could be that, the material at the vicinity of the notch is restricted by the material surrounds where both the ratcheting and relaxation effect are suppressed. Therefore, it is safe to conclude that the stress-strain hysteresis loop at the notch root will close itself under fully reversed nominal stress. Few attempts were made to find the correct stress-strain curve at the notch root for the third reversal shown in Figure 92 and Figure 93, given the hysteresis loop at the notch root will be closed for a fully reversed nominal stress applied.

As shown in Figure 92, the downward reversal of the fully reversed (R_{strain}=-1) hysteresis loop with a strain amplitude equivalent to the strain approximated by Neuber's rule at the end of second reversal at point 2 is taken (ε_{rp2}). By constructing the stress-strain curve in the relative coordinate system starting from reversing point 2 as well as the Neuber's hyperbola in the same coordinate system, it is apparent that, the stress-strain curve available is insufficient to reach the Neuber's hyperbola, thus, no intersection was found. By extrapolate the existing stress-strain curve, shown as the brown dashed line on the bottom-left corner of the graph, an intersection is found. However, the reversing point, which is point 3 shown in the figure does not coincide with point 1. In other words, the prediction of the stress-strain responses at the notch root by using this stress-strain curve (solid brown curve) will not lead to the closure of the hysteresis loop, which is contrary to the experimental observation in Figure 62 and Figure 69. In fact, this choice of the stress-strain curve will always lead to an unclosed hysteresis loop in general regardless of the nominal stress history.

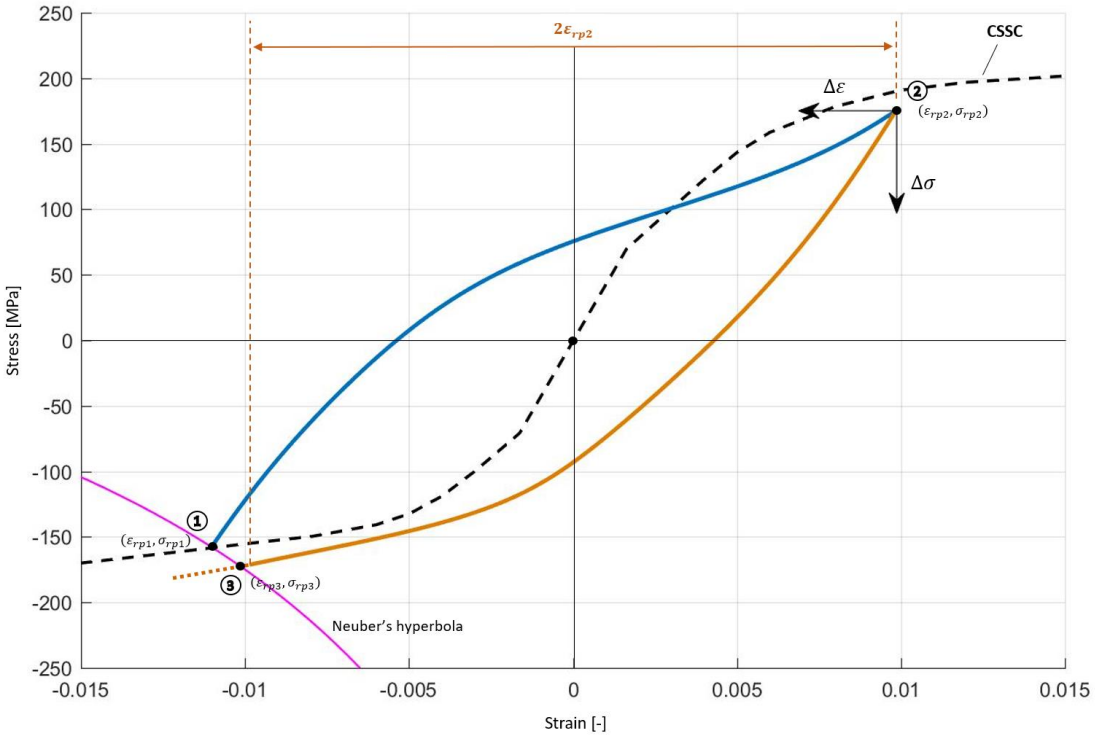

Figure 92. Stress-strain curve selection for the third reversal (solid brown curve)- The shape of the fully reversed (R_{strain}=-1) stress-strain hysteresis loop with the strain amplitude equivalent to the strain at the second reversing point (ε_{rp2}); The dashed brown curve on the bottom-left corner extended from the solid brown curve is the extrapolated line from the stress-strain curve since the range of the curve is insufficient to intersect with Neuber's hyperbola in this case

Another option of the stress-strain curve for this reversal could be taken from the downward reversal of the fully reversed (R_{strain}=-1) hysteresis loop with a strain range equivalent to the strain range between reversing point 1 and reversing point 2 ($\varepsilon_{rp2} - \varepsilon_{rp1}$), shown as the solid green curve in Figure 93. The curve is constructed using the phenomenological model and plotted in the relative coordinate system originated at point 2. The Neuber's hyperbola is also plotted in the same coordinate system shown as the solid purple curve. Even though an intersection between the stress-strain curve and Neuber's hyperbola is found shown as point 3, the hysteresis loop is still remaining unclosed.

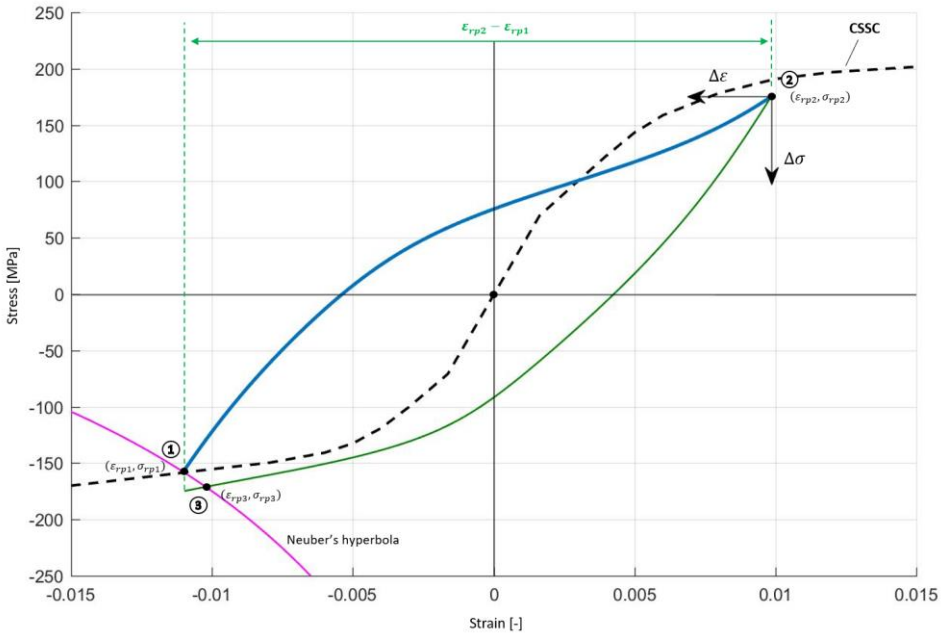

Figure 93. Stress-strain curve selection for the third reversal (solid green curve)- The shape of the fully reversed (R_{strain}=-1) stress-strain hysteresis loop with the strain range equivalent to the strain range between reversing point 1 and reversing point 2 ($\varepsilon_{rp2} - \varepsilon_{rp1}$)

Due to the fact that the phenomenological model been used to construct the stress-strain hysteresis loops is not only asymmetric but also uses different functions for the upward and downward reversals to mimic the actual material behavior, it is very unlikely for the hysteresis loop to close itself simultaneously using Neuber's rule without enforcing this condition. However, the Neuber's hyperbola is point symmetric in a relative coordinate system for a rain-flow counted cycle on the nominal stress history since the change of the nominal stress for both upward and downward reversals are the same. In other words, the reversal of the hysteresis loop which closes itself will also satisfies the Neuber's rule. As seen in Fig. 5, the Neuber's hyperbola, shown as the purple curve is intersect with reversing point 1 ($\varepsilon_{rp1}, \sigma_{rp1}$) in the relative coordinate system shown on the top-right corner originated at reversing point 2 ($\varepsilon_{rp2}, \sigma_{rp2}$). Therefore, instead of finding the corresponding stress-strain curve then apply Neuber's rule upon it to close the stress-strain hysteresis, it is possible to directly close the loop. As shown in Figure 94, the red curve is the corresponding downward reversal for the blue curve constructed using the phenomenological model to directly close the loop.

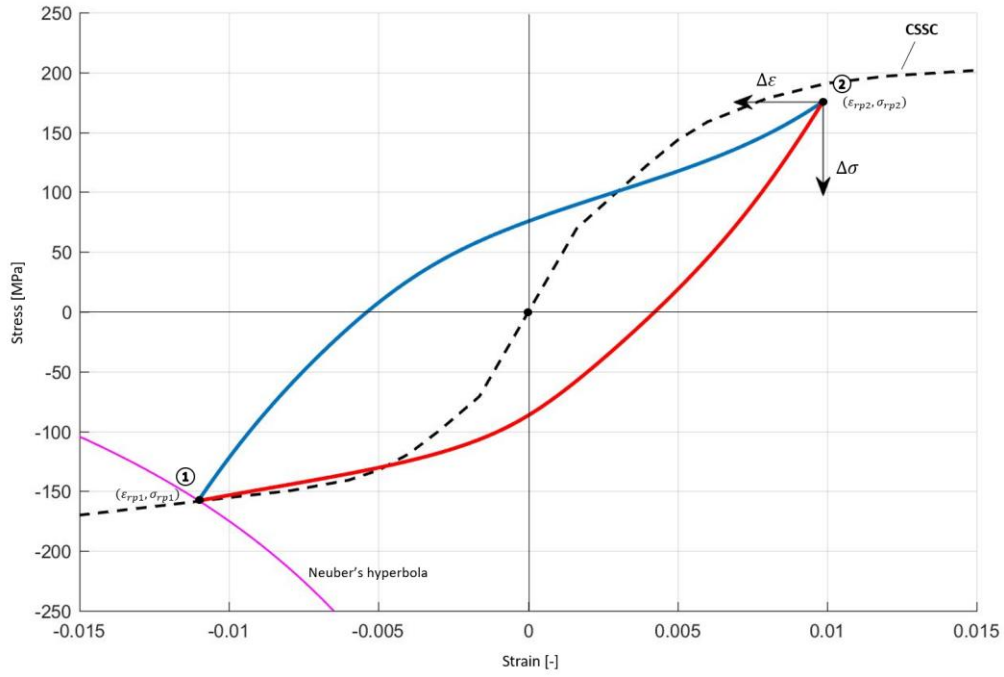

Figure 94. Stress-strain curve selection for the third reversal (solid red curve curve)- The stress-strain curve which will close the loop is chosen directly without applying Neuber's rule

This method is applied to any rain-flow counted cycles during the simulation that, the Neuber's rule is only applied to the stress-strain curve once per cycle. Once a cycle is completed, the simulation will select the stress-strain curve correspond to the same stress and strain range determined using Neuber's rule earlier on the previous reversal of this cycle to close the loop.

Similar to the smooth sample analysis, the load history will be rearranged to start and end with the absolute maximum value, shown in Figure 95, since the envelope hysteresis loop has to be determined first. The method of determining the envelope hysteresis is exactly the same as shown in Figure 90, Figure 91 and Figure 94; assuming the nominal stress applied remotely is fully reversed and the amplitude is equivalent to the absolute value of the maximum nominal stress from the load history. Not to mention that, the envelope hysteresis loop is not necessarily fully reversed in either strain or stress due to the asymmetry of the cyclic stress-strain curve, as seen in Figure 94.

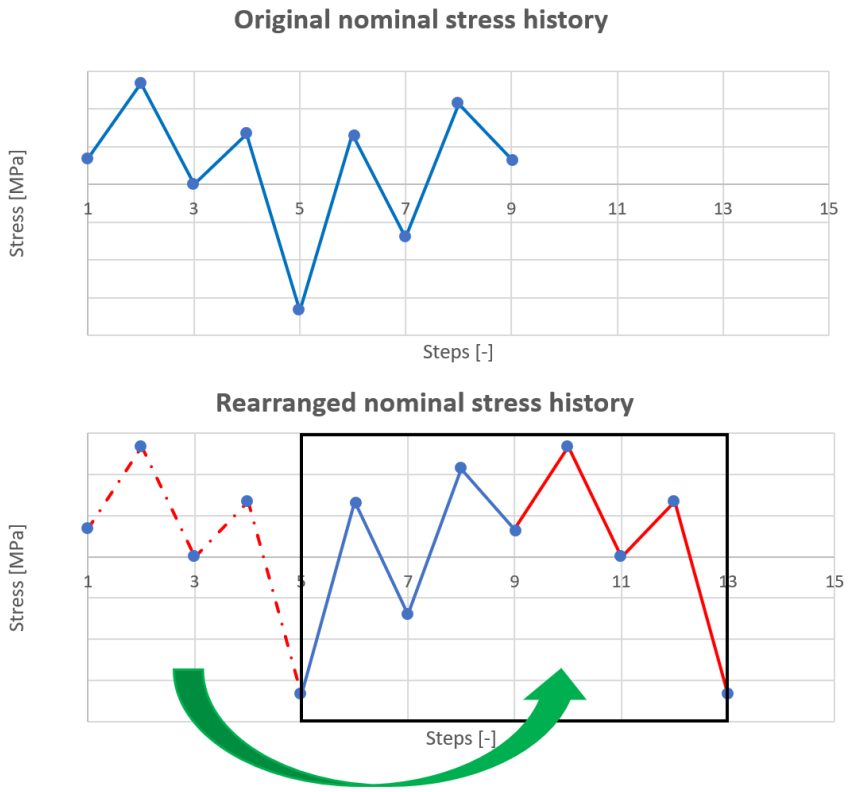

Figure 95. Re-arrangement of the nominal stress history to start/end from the absolute maximum value

The rain-flow counting method [87] -[89] is used upon the nominal stress history to track the material memory and identify the closed stress-stain hysteresis loops. Provides the elastic stress concentration factor K_t and Young's modulus, Neuber's rule is used to identify the landing point for each advance on the corresponding stress-strain curve generated using the phenomenological model. Once a rain-flow counted cycle is found to be closed, the stress-strain curve to be used for that reversal to close the loop is directly determined using the phenomenological model.

4.3.2 Approximation method using Glinka's rule

The nominal stress history is used with the Glinka's rule (ESED) [81] to approximate the stress-strain responses at the notch root. Different from Neuber's rule, the application of the Glinka's rule requires the calculation of the strain energy density, which is the area under the corresponding stress-strain curve in order to determine the next reversing point, as seen in Figure 11.

The Glinka's rule stated that, in the presence of localized small-scale plastic yielding, the gross linear elastic behavior of the material surrounding the notch controls the deformations in the plastic zone. Therefore, it can be concluded that the energy density in the plastic zone is equal to that calculated on the basis of the elastic solution [81] :

$$\frac{(\Delta S K_t)^2}{2E} = \int_0^{\Delta\epsilon_{ij}} \Delta\sigma_{ij}\, d\Delta\epsilon_{ij} \qquad (38)$$

The elastoplastic stress-strain curve at the notch root is numerically integrated to find the notch stress range ($\Delta\sigma$) and notch strain range ($\Delta\varepsilon$) on the stress-strain curve in which the area under the curve is equivalent to the elastic solution, shown as Figure 96.

Similar to the approach of using Neuber's rule, a new relative coordinate system is placed at the beginning of each reversal at the reversing point so that the following stress-strain path extends into the first quadrant of the coordinate system. The simulation starts with the origin of the global coordinate system following the experimentally determined cyclic stress-strain curve for the first reversal as shown in Figure 96. If the first reversal on the rearranged load history is going into compression first, the compressive branch of the cyclic stress-strain curve will be used; If the first reversal is going into tension first, the tensile branch of the cyclic stress-strain curve will be used instead.

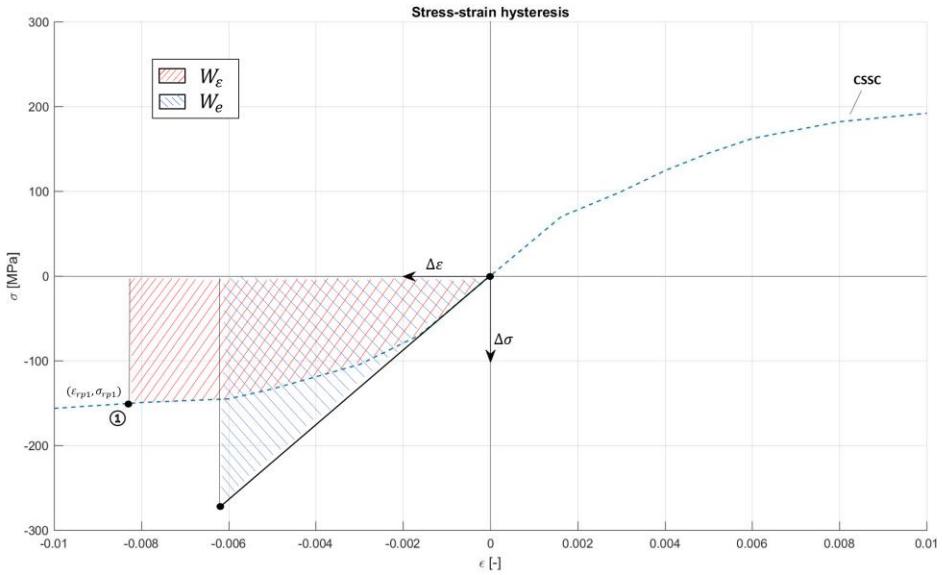

Figure 96. Calculation of the notch stress and strain ranges using Glinka's rule (ESED)

Following the compressive branch of the cyclic stress-strain curve to point 1 on the curve, where the area under the curve shown as the red shaded area (W_ε) is equal to the area under the elastic solution (W_e), shown as the blue shaded area. Therefore, the stress and strain value at point 1 in the global coordinate system correspond to the stress and strain approximation using Glinka's rule for the first reversal.

The second reversal follows the exact same logic as for how Neuber's rule is implemented, where the branch of the fully reversed (R_ε=-1) stress-strain hysteresis loop with the strain amplitude equivalent to the strain at the first reversing point (ε_{rp1}) will be followed. A new relative coordinate system is placed at point 1 ($\varepsilon_{rp1}, \sigma_{rp1}$) and the area under the next corresponding stress-strain curve in the same coordinate system is calculated to match the elastic solution given by Equation (29).

Unlike Neuber's rule, the notch-response approximation using Glinka's rule is much more sensitive to the shape of the stress-strain curve itself. Therefore, it is extremely unlikely that the hysteresis loop can close itself by applying Glinka's rule upon the stress-strain curves due to the asymmetry of the material stress-strain behavior, where the upward and downward reversals have different shapes. However, it has been experimentally proved that the stress-strain hysteresis loop at the vicinity of the notch root will close itself under fully reversed nominal stress applied, as seen in Figure 62 and Figure 69. As a result, this condition has to be enforced to correctly mimic the stress-strain behavior at the notch root

under remote stresses. Accordingly, once a rain-flow counted cycle is deemed to be closed, the stress-strain curve which will close the hysteresis loop will be picked to directly close the loop without applying Glinka's rule to the stress-strain curve.

To future improve the prediction, the strain energy density correction factor for plastic yielding (C_p) by G. Glinka [82] has been used to account for the stress re-distribution due to plastic yielding at the vicinity of the notch root.

As seen in Figure 12, the real stresses within the plastic zone are significantly lower than what derived from the linear elastic analysis (σ_y). In order to satisfy the equilibrium condition, the stress distribution is shifted in which the shaded area F_1 is equal to F_2.

The first approximation of the plastic zone size ahead of the notch root r_p for uniaxial tension or compression derived from the Hencky-Mises-Huber criterion under plane stress state is given as:

$$\sigma_y = \frac{k_t S}{2\sqrt{2}}\left[\frac{\rho}{r_p} + \frac{3}{4}\left(\frac{\rho}{r_p}\right)^3\right]^{1/2} \tag{39}$$

In which ρ is the notch radius of the curvature, σ_y is the yield stress and S is the nominal stress applied remotely.

Known the yield stress, nominal stress and notch radius, the first approximation of the plastic zone size ahead of the notch root r_p can be easily calculated using the Newton-Raphson method. It should be noted that, the yield stress is different with what derived using the monotonic stress-strain curve for cyclic loading. Therefore, the yield stress for each reversal is individually calculated based on 0.2 percent plastic strain.

Finally, the correction factor for the energy density C_p at the notch root under tension or compression can be calculated using:

$$C_p = 1 + \left(\rho/r_p\right)\left[\frac{2\left(r_p/\rho\right)^{1/2} - \left(\rho/r_p\right)^{1/2}}{\left(\rho/r_p\right)^{1/2} + \frac{1}{2}\left(\rho/r_p\right)^{3/2}} - \left(\frac{r_p}{\rho} - \frac{1}{2}\right)\right] \tag{40}$$

The correction factor for the energy density C_p is directly applied to the elastic solution of the strain energy density at the notch root:

$$C_p \frac{(\Delta S \cdot K_t)^2}{2E} = \int_0^{\Delta\epsilon_{ij}} \Delta\sigma_{ij}\, d\Delta\epsilon_{ij} \qquad (41)$$

During the simulation, the yield stress for each reversal is first calculated based on the 0.2 percent plastic strain criteria. In the case of the stress-strain curve is entirely within the elastic region, a C_p factor of 1 is directly assigned without further calculation. If the available stress-strain extends to the plastic region, the yield limit will be determined and assigned to the corresponding curve. Next, the first approximation of the plastic zone size ahead of the notch root r_p then will be calculated using Equation (39). Finally, the corresponding C_p factor can be determined using Equation (40).

The C_p correction factor is applied for every single reversal. Once the C_p factor is determined, Equation (41) will be used to replace Equation (38) in order to find the landing point on the stress-strain curve.

4.3.3 Plane strain transformation for Neuber's and Glinka's rule

To account for the non-zero through thickness component of the stress (σ_{33}) shown in Figure 97 and Figure 98 due to geometrical constraint, the plane strain correction by Dowling, N. [90] and lately explained in detail by Jahed, H. [98] has been used to transform the uniaxial plane stress stress-strain curve into the equivalent biaxial plane strain stress-strain curve.

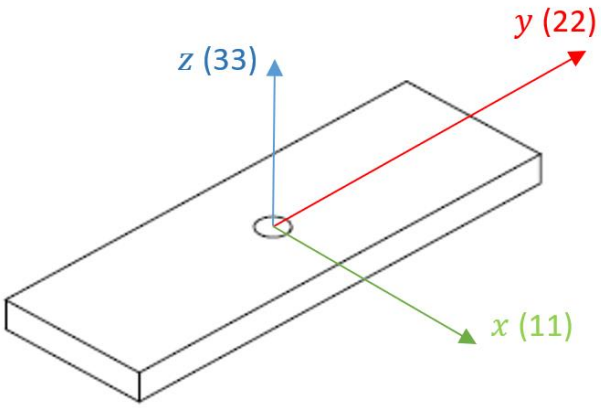

Figure 97. Direction assigned to the notched sample

For a notched thin sheet (t is small), the material in the through-thickness direction (33) at the notch root is not able to build up any stress due to a lack of support from the surrounding material where the Poisson's effect occurs freely when a stress in the axial direction (22) is applied. The stress state at the notch root under plane stress condition shown in Figure 98 can be written as:

$$\sigma_{nr(\text{plane stress})} = \begin{bmatrix} 0 & 0 & 0 \\ 0 & \sigma_{22} & 0 \\ 0 & 0 & 0 \end{bmatrix} \tag{42}$$

The corresponding strain state at the notch root can be written as:

$$\varepsilon_{nr(\text{plane stress})} = \begin{bmatrix} \varepsilon_{11} & 0 & 0 \\ 0 & \varepsilon_{22} & 0 \\ 0 & 0 & \varepsilon_{33} \end{bmatrix} \tag{43}$$

Even though there are three non-zero components of strain present at the notch root, namely, ε_{11}, ε_{22}, and ε_{33}, only the σ_{22} and ε_{22} contribute to the deformation energy and the strain energy density at the notch root can be calculated by the area under the stress-strain curve in the axial direction (22):

$$W_{nr(\text{plane stress})} = \int_0^{\varepsilon_{22}} \sigma_{22}\, d\varepsilon_{22} \tag{44}$$

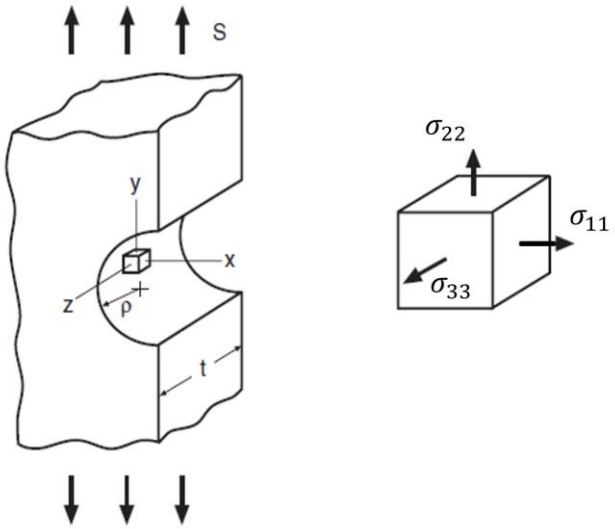

Figure 98. Stress state at the notch root under an applied nominal tensile stress S [6]

For a thicker notched plate (t is large), the deformation in the through-thickness direction (33) at the notch root is restricted by the surrounding material which is subject to lower stresses outside of the localized plastic zone in the vicinity of the notch root and the Poisson's effect is relatively small. The stress at the notch root can be written as:

$$\sigma_{ns(\text{plane strain})} = \begin{bmatrix} 0 & 0 & 0 \\ 0 & \sigma_{22} & 0 \\ 0 & 0 & \sigma_{33} \end{bmatrix} \tag{45}$$

And the corresponding strain at the notch root under the plane strain condition can be written as:

$$\varepsilon_{nr(\text{plane strain})} = \begin{bmatrix} \varepsilon_{11} & 0 & 0 \\ 0 & \varepsilon_{22} & 0 \\ 0 & 0 & 0 \end{bmatrix} \tag{46}$$

Notice that the strain in the through-thickness direction (33) is zero due to the restrictions of deformation, which induces the stress in the same direction. However, the strain energy density at the notch root is only contributed by the stress and strain in the axial direction:

$$W_{nr(\text{plane strain})} = \int_0^{\varepsilon_{22}} \sigma_{22}\, d\varepsilon_{22} \quad (47)$$

Although the equations used to calculate the strain energy density at the notch root under both plane stress and plane strain condition may look the same, the stress-strain curves for cases are very different. In the case of plane strain state, the geometric constraint from the surrounding material limits the deformation in the through-thickness direction (33), which results in the rise of the stress in both axial (22) and through thickness (33) direction. For this reason, it is possible to only transform the stress-strain curve in the plane stress state to the equivalent plane strain state in the axial direction (22), yet still able to calculate the strain energy density at the notch root. Therefore, the energy-based approximations like Neuber's rule and Glinka's rule still hold by using the transformed stress-strain curve.

Using the total deformation plasticity theory [91] [97] , the total strain at the notch root is then broken down to elastic and plastic strain components:

$$\varepsilon_{ij} = \varepsilon_{ij}^{e} + \varepsilon_{ij}^{p} \quad (48)$$

And the deviatoric stress tensor can be expressed as:

$$s_{ij} = \sigma_{ij} - \frac{1}{3}\sigma_{kk}\delta_{ij} \quad (49)$$

Which is the subtraction of the hydrostatic stress from the total stress. Also known that the plastic strain is a function of the deviatoric stress by:

$$\varepsilon_{ij}^{p} = \phi s_{ij} \quad (50)$$

Where,

$$\phi = \frac{3\varepsilon_e^p}{2\sigma_e} \quad (51)$$

And the elastic strain can be expressed using Hooke's law:

$$\varepsilon_{ij}^{e} = \left(\frac{1+v}{E}\right)\sigma_{ij} - \left(\frac{v}{E}\right)\sigma_{kk}\delta_{ij} \tag{52}$$

Combine the plastic strain and elastic strain gives:

$$\varepsilon_{ij} = \left(\frac{1+v}{E} + \phi\right)\sigma_{ij} - \left(\frac{v}{E} + \frac{\phi}{3}\right)\sigma_{kk}\delta_{ij} \tag{53}$$

Combine the terms to form of the elastoplastic Hooke's law:

$$\varepsilon_{ij} = \frac{1+v_{\text{eff}}}{E_{\text{eff}}}\sigma_{ij} - \frac{v_{\text{eff}}}{E_{\text{eff}}}\sigma_{kk}\delta_{ij} \tag{54}$$

Where E_{eff} is the secant modulus given in Equation (55):

$$E_{\text{eff}} = \frac{3E}{3+2E\phi} \tag{55}$$

And v_{eff} is the effective Poisson's ratio:

$$v_{\text{eff}} = \frac{3v+E\phi}{3+2E\phi} \tag{56}$$

Expand and substitute Equation (45-46) into the elastoplastic Hooke's law gives:

$$\begin{cases} \varepsilon_{11} = -\frac{v_{\text{eff}}}{E_{\text{eff}}}(\sigma_{22} - \sigma_{33}) \\ \varepsilon_{22} = \frac{1}{E_{\text{eff}}}\sigma_{22} - \frac{v_{\text{eff}}}{E_{\text{eff}}}\sigma_{33} \\ 0 = \frac{1}{E_{\text{eff}}}\sigma_{33} - \frac{v_{\text{eff}}}{E_{\text{eff}}}\sigma_{22} \end{cases} \tag{57}$$

The third equation in Equation (57) gives:

$$\sigma_{33} = \upsilon_{\text{eff}}\sigma_{22} \tag{58}$$

Substitute Equation (58) into the second equation in Equation (57) gives:

$$\varepsilon_{22} = \frac{1}{E_{\text{eff}}}\sigma_{22} - \frac{v_{\text{eff}}}{E_{\text{eff}}}\upsilon_{\text{eff}}\sigma_{22} = \frac{1-{v_{\text{eff}}}^2}{E_{\text{eff}}}\sigma_{22} \tag{59}$$

Even though Equation (50) gives the relation between the stress and strain in the axial direction (22) under plane strain condition, the stress in the axial direction (22) is not yet available. However, known the relation between σ_{22} and σ_{33}, it is possible to express the axial strain in terms of the effective stress, which is readily available:

$$\sigma_e = (\sigma_{22}^2 - \sigma_{22}\sigma_{33} + \sigma_{33}^2)^{\frac{1}{2}} \tag{60}$$

Substitute Equation (58) into Equation (60) gives:

$$\sigma_e = \left(\sigma_{22}^2 - v_{\text{eff}}\sigma_{22}\,\sigma_{22} + v_{\text{eff}}^2\,\sigma_{22}^2\right)^{\frac{1}{2}} \tag{61}$$

Isolate σ_{22} gives:

$$\sigma_{22} = \frac{\sigma_e}{\sqrt{1-v_{\text{eff}}+v_{\text{eff}}^2}} \tag{62}$$

This expression can then be directly used since the effective stress at the notch root under plane stress condition is equivalent to the axial stress since that is the only non-zero component of stress. Notice that the effective Poisson's ratio (υ_{eff}) is a function of the effective stress (σ_e) and effective plastic strain (${\varepsilon_e}^p$) which is not readily available, however, the effective Poisson's ratio (υ_{eff}) can be calculated discretely at each point, provided the plane stress stress-strain curve in the axial direction. Also substitute the Equation (62) into Equation (59) gives:

$$\varepsilon_{22} = \frac{1-{v_{\text{eff}}}^2}{E_{\text{eff}}}\frac{\sigma_e}{\sqrt{1-v_{\text{eff}}+v_{\text{eff}}^2}} \tag{63}$$

Substitute the definition of the secant modulus ($E_{\text{eff}} = {\sigma_e}/{\varepsilon_e}$) [99] into Equation (63) gives:

$$\varepsilon_{22} = \frac{1-{\nu_{\text{eff}}}^2}{\sqrt{1-\nu_{\text{eff}}+\nu_{\text{eff}}^2}}\varepsilon_e \tag{64}$$

Equation (62) and Equation (64) provide the linkage between the effective stress (σ_e) and effective strain (ε_e) to the stress and strain in the axial direction (σ_{22} and ε_{22}) under the biaxial plane strain condition. Also known that the stress state at the notch root is uniaxial under plane stress condition, which gives:

$$\varepsilon_{e\,\text{plane stress}} = \varepsilon_{22\,\text{plane stress}} \tag{65}$$

$$\varepsilon_{e\,\text{plane stress}}^{p} = \varepsilon_{22\,\text{plane stress}}^{p} \tag{66}$$

$$\sigma_{e\,\text{plane stress}} = \sigma_{22\,\text{plane stress}} \tag{67}$$

Therefore, the final form of the plane strain transformation equations can be written as:

$$\varepsilon' = \frac{1-{\nu_{\text{eff}}}^2}{\sqrt{1-\nu_{\text{eff}}+\nu_{\text{eff}}^2}}\varepsilon \tag{68}$$

$$\sigma' = \frac{1}{\sqrt{1-\nu_{\text{eff}}+\nu_{\text{eff}}^2}}\sigma \tag{69}$$

$$\nu_{\text{eff}} = \frac{\nu+\frac{E\varepsilon^p}{2\sigma}}{1+\frac{E\varepsilon^p}{\sigma}} \tag{70}$$

$$\varepsilon^p = \varepsilon - \frac{\sigma}{E} \tag{71}$$

Where σ and ε are the axial stress and strain under plane stress condition whereas σ' and ε' are the transformed axial stress and strain under plane strain condition. Given the axial stress-strain curve under plane stress condition, the curve is then discretized to points on the stress-strain curve and each point is then mapped to the points on the analogous plane strain stress-strain curve as shown in Figure 99. Finally, the transformed plane strain stress-strain curve then can be used with either Neuber's or Glinka's rule to approximate the stress strain at the notch root under plane strain condition.

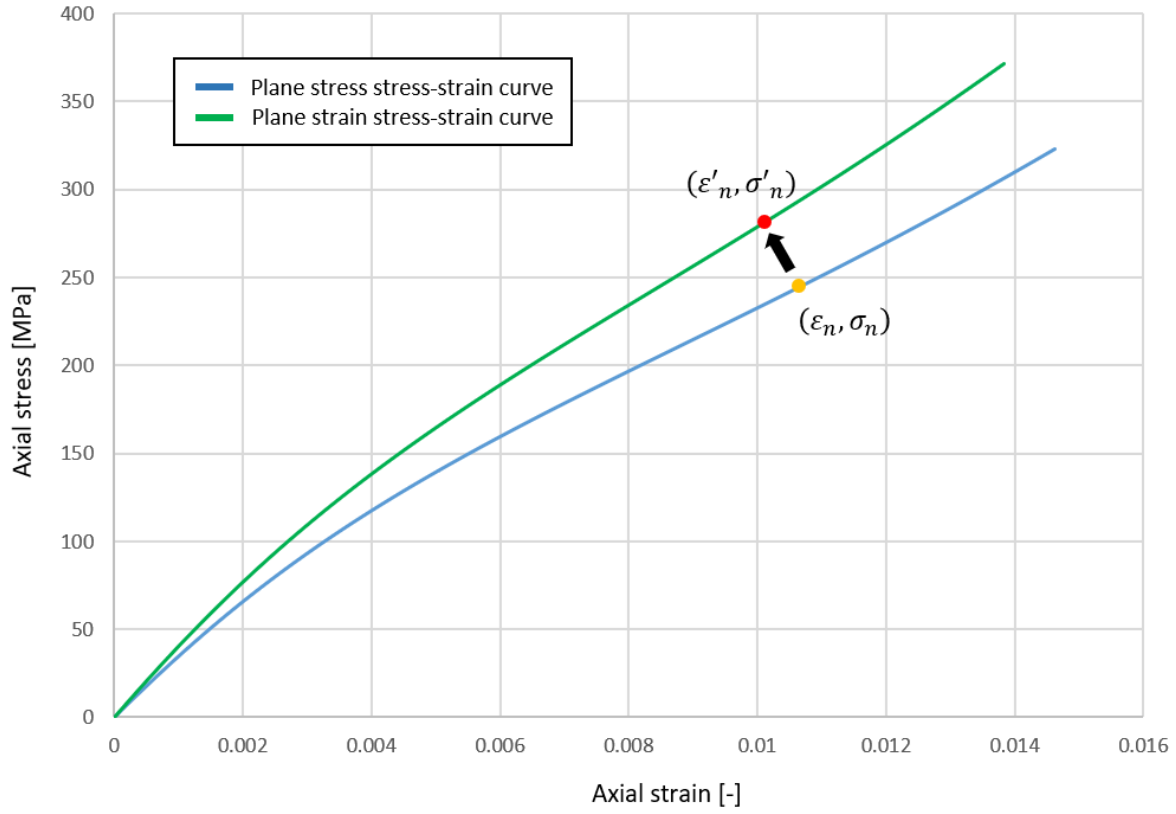

Figure 99. Plane stress to plane strain stress-strain curve transformation by Dowling et al.

The plane strain correction is applied reversal by reversal starts from the cyclic stress-strain curve. Once the stress-strain curve to be used is determined, a new relative coordinate system will be placed at the beginning of that reversal in which the stress-strain path extends into the first quadrant of the coordinate system. The plane strain correction is then applied within the same coordinate system by:

$$\Delta\varepsilon' = \frac{1-{\nu_{\text{eff}}}^2}{\sqrt{1-\nu_{\text{eff}}+\nu_{\text{eff}}^2}}\Delta\varepsilon \tag{72}$$

$$\Delta\sigma' = \frac{1}{\sqrt{1-\nu_{\text{eff}}+\nu_{\text{eff}}^2}}\Delta\sigma \tag{73}$$

$$\nu_{\text{eff}} = \frac{\nu+\frac{E\Delta\varepsilon^p}{2\Delta\sigma}}{1+\frac{E\Delta\varepsilon^p}{\Delta\sigma}} \tag{74}$$

$$\Delta\varepsilon^p = \Delta\varepsilon - \frac{\Delta\sigma}{E} \tag{75}$$

Once the corrected plane strain stress-strain curve is obtained, it will replace the original stress-strain curve and either Neuber's or Glinka's rule will be used to predict the stress-strain response at the vicinity of the notch root.

Due to the limitations of the phenomenological model which is used to obtain the shape of the stress-strain curve, the stress and strain range, as well as the stress and strain value at the beginning of each reversal, are needed to construct the stress-strain curve. However, none of them would be readily available after the replacement of the original stress-strain curve with the corrected plane strain stress-strain curve for the previous reversal. Even though the Neuber's or Glinka's approximation using the corrected plane strain stress-strain curve provide the stress and strain range under plane strain condition for the next reversal, the corresponding stress-strain curve cannot be directly obtained using the phenomenological model since the stress state at the notch root is not uniaxial. The corresponding plane stress stress-strain curve has to be known for every single reversal in order to find its plane strain counterpart.

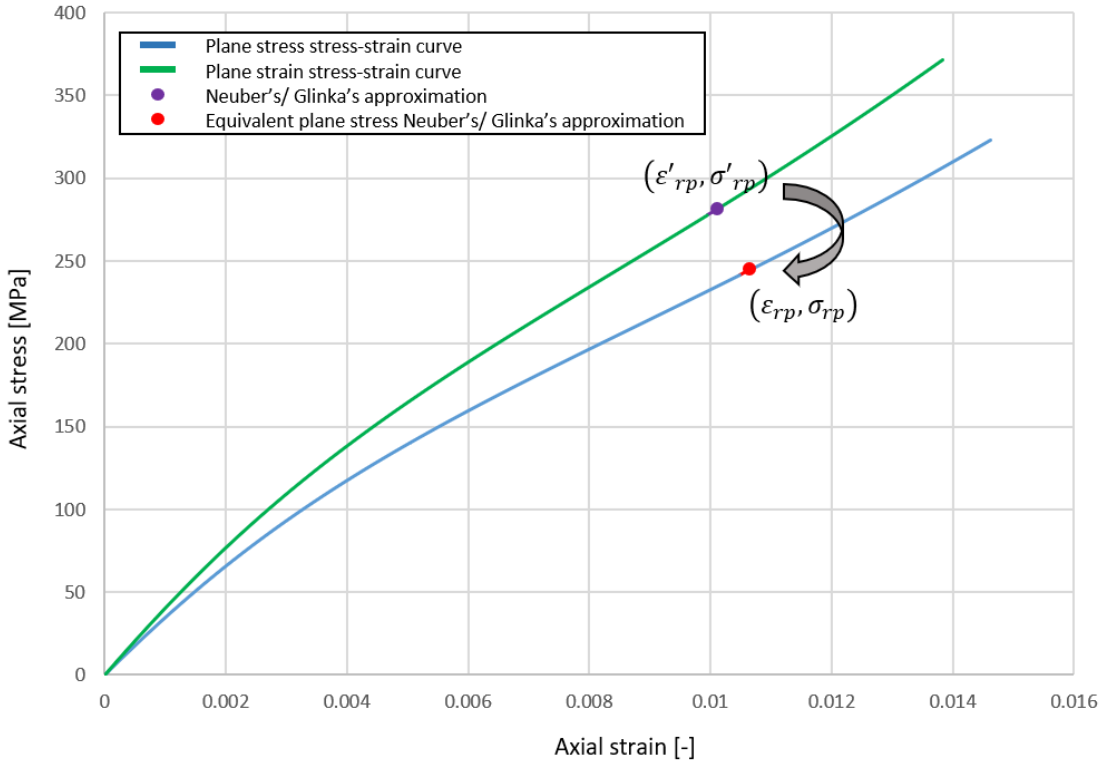

Figure 100. Back transformation from plane strain to plane stress stress-strain curve

For this reason, every time the prediction is made using either Neuber's or Glinka's rule upon the corrected plane strain stress-strain curve, the prediction result is stored as the plane strain response at the vicinity of the notch root for that load history segment and at the same time, the predicted point on the corrected stress-strain curve is transformed back to the point on the plane stress stress-strain curve to obtain the corresponding stress-strain curve to be followed for the succeed reversals as shown in Figure 100.

In other words, the approximation method of Neuber's or Glinka's is executed upon the corrected stress-strain curves whereas the determination of the stress-strain curves to be followed is executed upon the original stress-strain curve. However, there is no analytical solution to map back to the plane stress curve from the corrected plane strain stress-strain curve using (equation placeholder), the Newton-Raphson method is used to numerically calculate the corresponding point (ε_{rp}, σ_{rp}) on the original stress-strain curve equivalent to the prediction on the corrected stress-strain curve (ε'_{rp}, σ'_{rp}).

4.3.4 Experimental Verification (notched)

The experimental results on notched specimens under constant-amplitude nominal stresses for ZEK100-O are compared with the model predictions. Due to the large thickness of the notched specimens have been used for these tests, the stress state at the notch root under load is much closer to plane strain and the plane strain results by the model is expected to be closer to the experimental results, however, all the possible output options of the model are shown for the sake of comparison in Figure 101 - Figure 104:

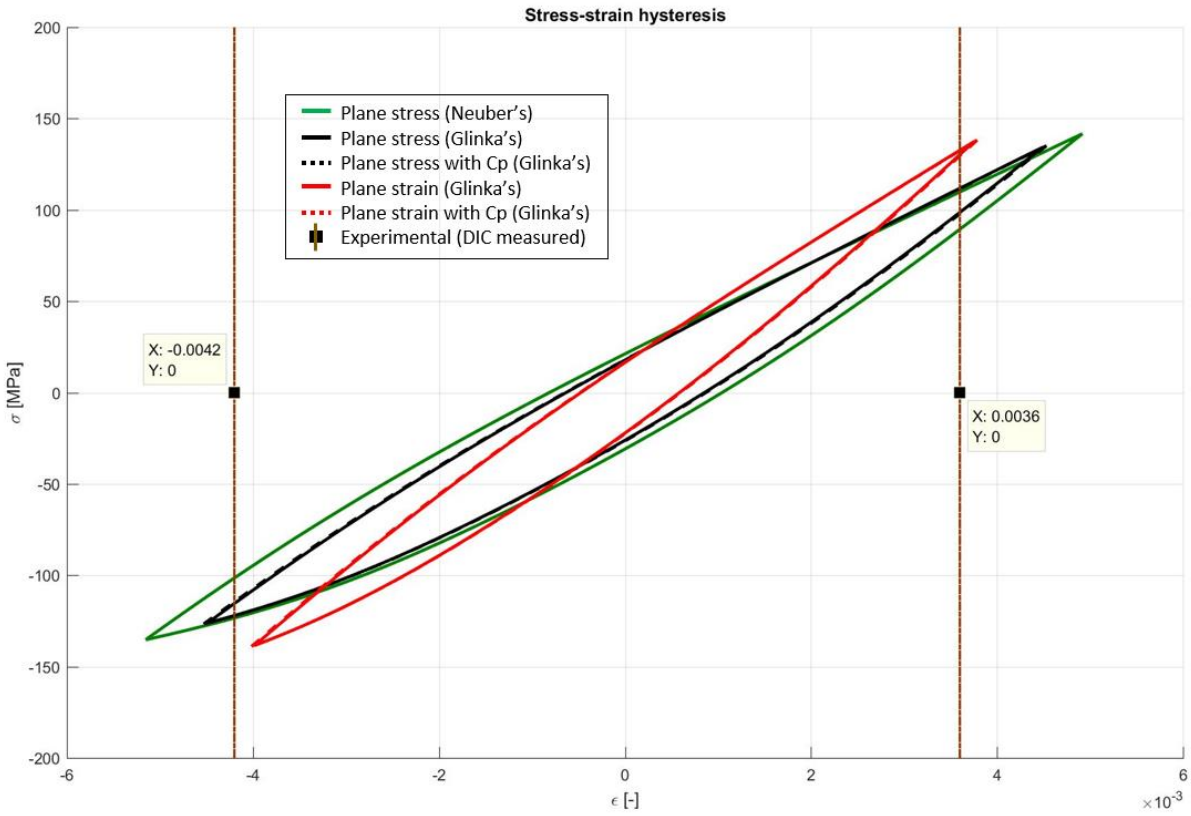

Figure 101. Modeled notch stress-strain hysteresis loop vs. Experimental notch stain responses @ 50% of compressive yield equivalent fully-reversed nominal stress (68.45 MPa) (Note that the Plane strain Neuber's solution is not shown in this figure since the available stress-strain curves are insufficient to reach the Neuber's hyperbola in this case) - ZEK100-O

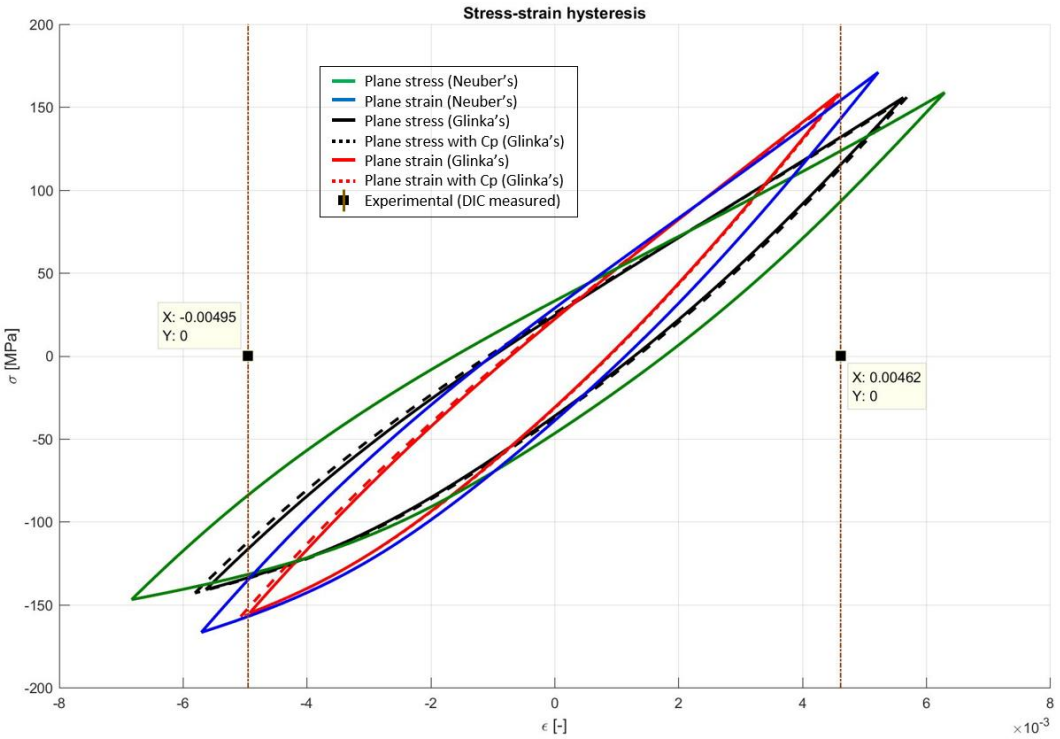

Figure 102. Modeled notch stress-strain hysteresis loop vs. Experimental notch stain responses @ 60% of compressive yield equivalent fully-reversed nominal stress (82.14 MPa) - ZEK100-O

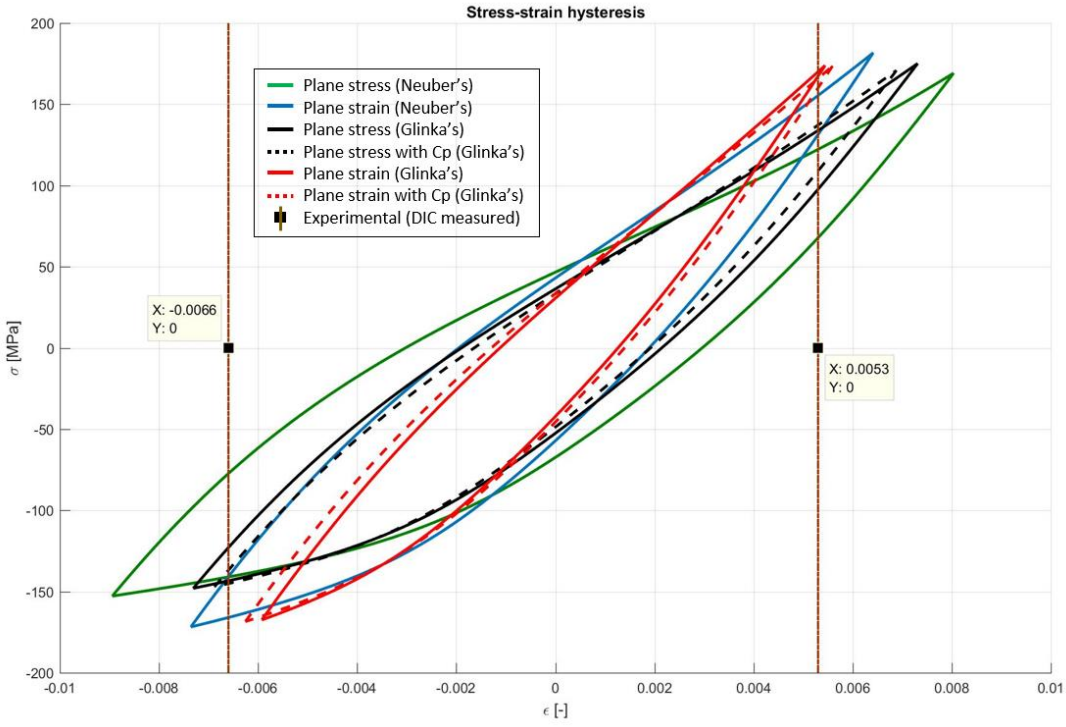

Figure 103. Modeled notch stress-strain hysteresis loop vs. Experimental notch stain responses @ 70% of compressive yield equivalent fully-reversed nominal stress (95.83 MPa) - ZEK100-O

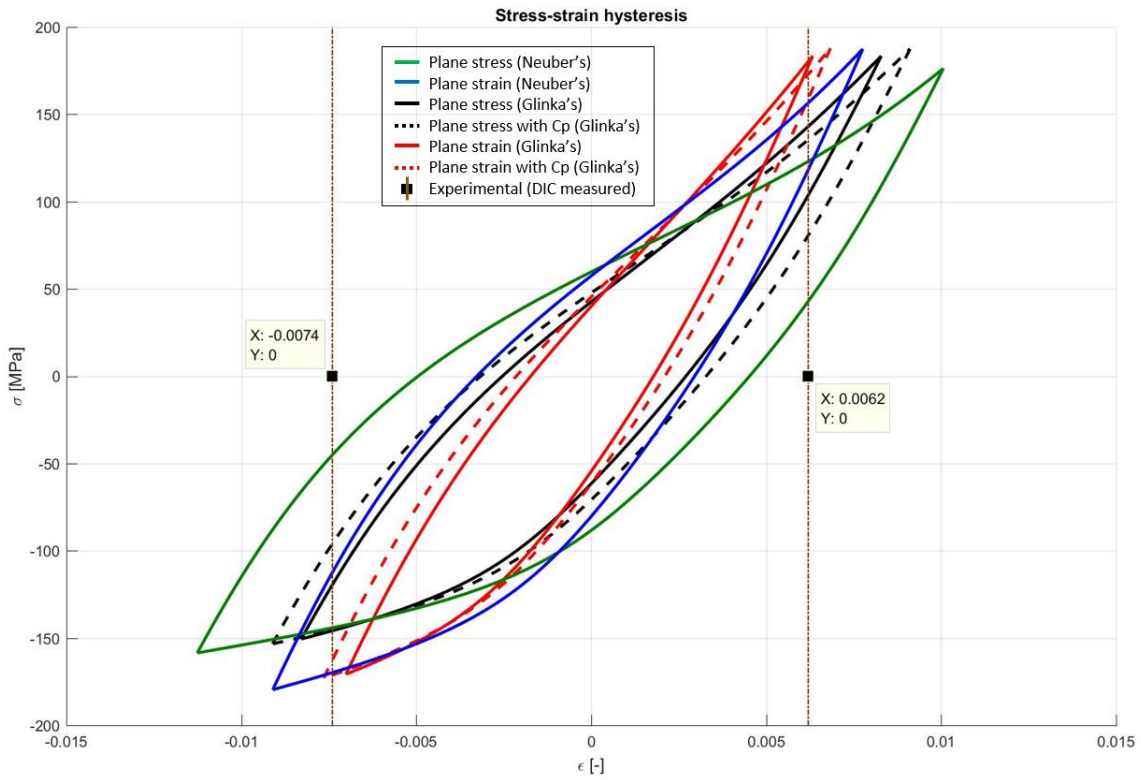

Figure 104. Modeled notch stress-strain hysteresis loop vs. Experimental notch stain responses @ 80% of compressive yield equivalent fully-reversed nominal stress (109.52 MPa) - ZEK100-O

The brown dotted vertical lines in Figure 101 - Figure 104 represent the experimentally measured axial notch strain value at peak tension and compression after the stabilization summarized in Table 8. Both plane stress and plane strain predictions using Neuber's and Glinka's rules are present. In addition, the differences in the prediction of the stress-strain hysteresis loops by having the C_p are also shown.

It can be seen that the Neuber's rule over-predicts the notch stresses and strains in all cases whereas the Glinka's rule under-predicts the notch stresses and strains which is aligned with what has been suggested in the literature as discussed in chapter 2. The inclusion of the C_p correction using Glinka's rule improves the prediction in all cases, however, the effect of the correction is insignificant when the nominal stress amplitude is low, as seen in Figure 101 and Figure 102, due to a small plastic zone size whereas the over-prediction is now possible for a relatively larger nominal stress amplitude as seen in Figure 104. Besides, the plane strain solution leads to a higher notch stress value for a lower strain in all cases.

It is apparent that the plane strain solutions for both Neuber's and Glinka's rule give better perditions as what to be expected, yet, the predictions by plane strain Glinka's rule with C_p correction are the closest to the experiments.

The experimental results on notched specimens under constant-amplitude nominal stresses for AZ31B-H24 are also compared with the model predictions, shown in:

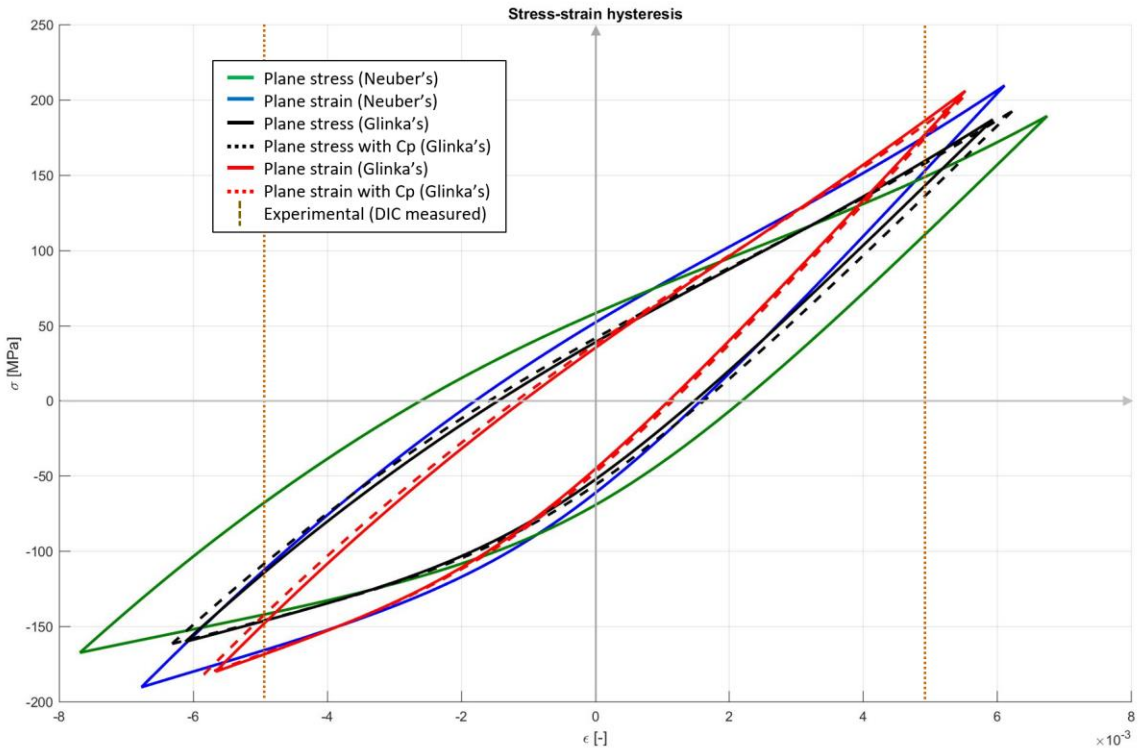

Figure 105. Modeled notch stress-strain hysteresis loop vs. Experimental notch stain responses @ 60% of compressive yield equivalent fully-reversed nominal stress (94.84 MPa) – AZ31B-H24

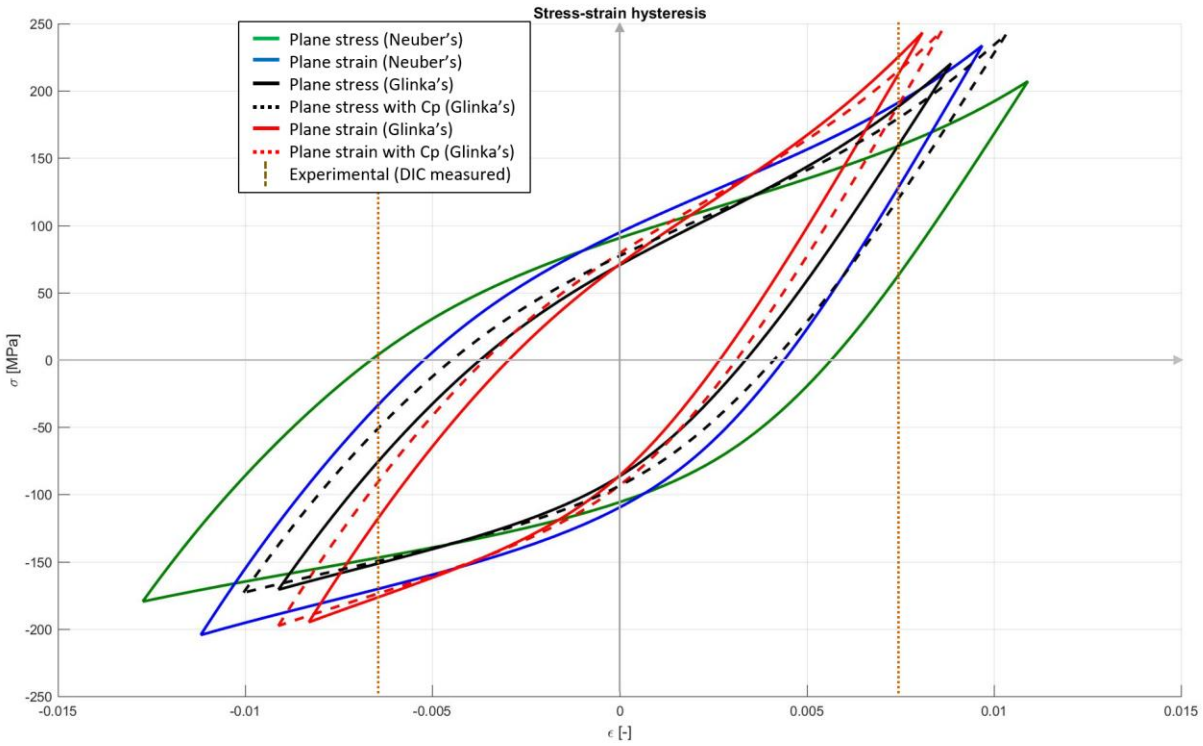

Figure 106. Modeled notch stress-strain hysteresis loop vs. Experimental notch stain responses @ 80% of compressive yield equivalent fully-reversed nominal stress (126.45 MPa) – AZ31B-H24

It can be seen that both Neuber's and Glinka's rules lead to overprediction of the notch strains on AZ31B-H24, which is contradicting to what has been suggested in the literature that, Glinka's rule should always lead to underprediction of the notch stresses and strains. However, the Glinka's rule is very sensitive to the shape of the stress-strain paths, which were generated using the phenomenological model by Dallmeier et al. [5] . The deviation between the model and the actual stress-strain path is believed to cause the overprediction in the case.

Chapter 5: Fatigue Modelling

Engineering components are often subjected to cyclic loads in their applications, and the resulting cyclic stresses can cause microscopic damage to the material. These microscopic damages can accumulate until a crack is developed, which will lead to a catastrophic failure of the component even if the stresses are well below the ultimate strength of the material. Therefore, it is essential to be able to accurately predict the fatigue life of engineering components in their design phase as well as in service to prevent fatigue failure to happen.

There are many fatigue models have been developed over the years, however, they all fall into these three big categories:

i. Strain-based approach
ii. Stress-based approach
iii. Energy-based approach

Since the fatigue tests have been done on ZEK100-O smooth specimens were all strain-controlled, the stress-based approach may not be appropriate for the modeling of the fatigue behavior. In addition, the increasing of the strain amplitude does not necessarily induce a higher peak stress or mean stress in ZEK100-O magnesium alloy, however, the impact on the fatigue life is certain. Therefore, a strain-based (SWT) and an energy based (J-V energy) fatigue model have been chosen to model the fatigue behavior of ZEK100-O magnesium alloy.

5.1 Smith-Watson-Topper (SWT) model

As one of the most widely used approaches, Smith-Watson-Topper (SWT) model was developed as a modification upon the Coffin-Manson relations, which taking account for mean stress effects in fatigue life analysis [7] :

$$\sigma_{max}\varepsilon_a = f(2N_f) \tag{73}$$

Where σ_{max} is the maximum tensile stress, ε_a is the strain amplitude and N_f is the number of reversals to failure.

The strain amplitude versus life curve can be decomposed to elastic and plastic strain amplitude shown in Equation (74):

$$\varepsilon_a = \frac{\varepsilon_e}{2} + \frac{\varepsilon_p}{2} \tag{74}$$

The relation between the elastic strain amplitude and life is given in Equation (75):

$$\frac{\varepsilon_e}{2} = \frac{\sigma_a}{E} = \frac{\sigma'_f}{E}\left(2N_f\right)^b \tag{75}$$

And the relation between the plastic strain amplitude and life is given in Equation (76):

$$\frac{\varepsilon_p}{2} = \varepsilon'_f\left(2N_f\right)^c \tag{76}$$

By substitute Equation (75-76) into Equation (74):

$$\varepsilon_a = \frac{\sigma'_f}{E}\left(2N_f\right)^b + \varepsilon'_f\left(2N_f\right)^c \tag{77}$$

Equation (77) is known as the Coffin-Manson relation, which is named by the separate development of related equations in the 1950s by L. F. Coffin and S. S. Manson, where E is the Young's modulus, N_f is the reversals to failure, σ'_f is the fatigue strength coefficient, b is the fatigue strength exponent, ε'_f is the fatigue ductility coefficient and c is the fatigue ductility exponent.

Known that the maximum stress can be represented by the mean stress (σ_{mean}) and stress amplitude (σ_a) by:

$$\sigma_{max} = \sigma_{\text{mean}} + \sigma_a \tag{78}$$

Substitute Equation (78) into Equation (73) gives:

$$(\sigma_{\text{mean}} + \sigma_a)\varepsilon_a = f(2N_f) \tag{79}$$

Also known that the fatigue life is expected to be the same if the mean stress is zero ($\sigma_{\text{mean}} = 0$):

$$\sigma_{max}\varepsilon_a = \sigma_a\varepsilon_a \qquad (\sigma_{\text{mean}} = 0) \tag{80}$$

Substitute Equation (75) and Equation (77) into Equation (80) gives:

$$\sigma_{max}\varepsilon_a = \sigma'_f\left(2N_f\right)^b \cdot \left[\frac{\sigma'_f}{E}\left(2N_f\right)^b + \varepsilon'_f\left(2N_f\right)^c\right] \tag{81}$$

Rearrange the equation gives:

$$\sigma_{max}\varepsilon_a = \frac{{\sigma'_f}^2}{E}\left(2N_f\right)^{2b} + \sigma'_f \cdot \varepsilon'_f\left(2N_f\right)^{b+c} \tag{82}$$

Equation (82) is the full-expression of the SWT model, which link the strain amplitude (ε_a), maximum tensile stress (σ_{max}) to the fatigue life of the material.

The Coffin-Manson relation is fitted to the experimentally determined strain amplitude versus life to failure curve of the fully-reversed (R_ε=-1) strain-controlled tests in Figure 44 and shown in Figure 107:

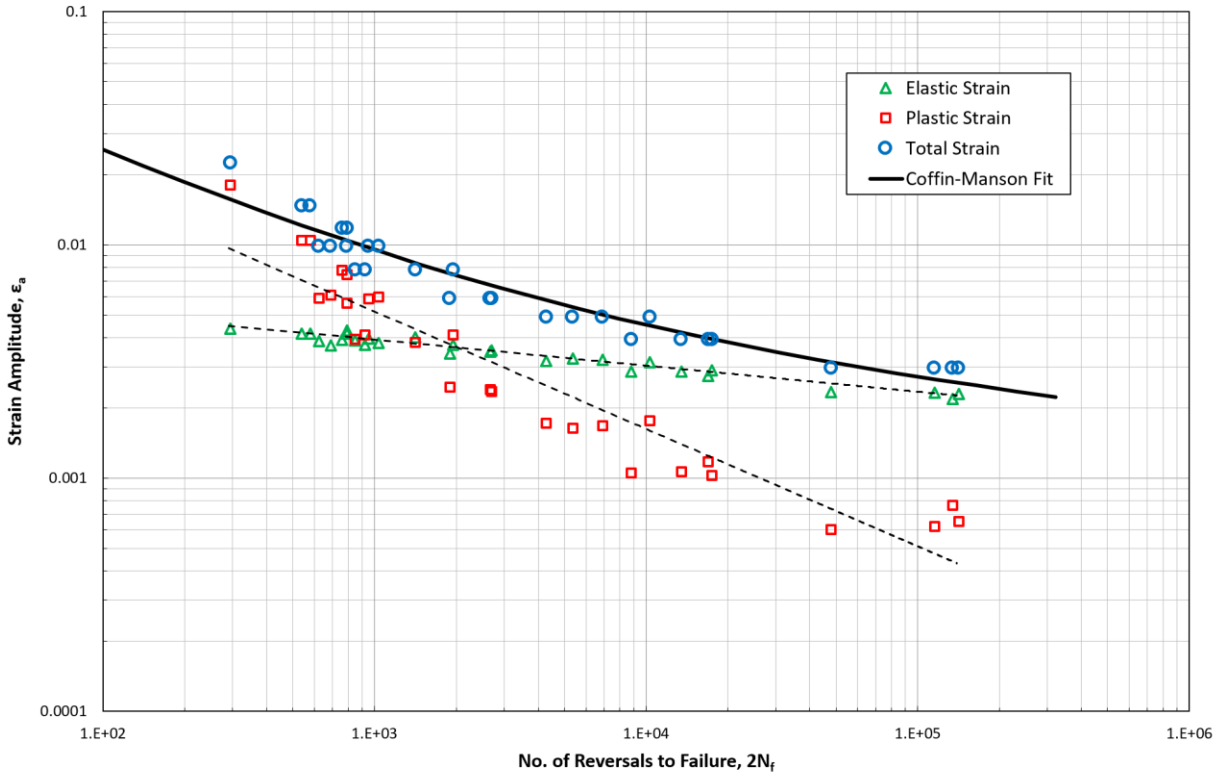

Figure 107. Coffin-Manson relation fitted to the strain amplitude vs. number of reversals to failure curve- ZEK100-O

The Coffin-Manson parameters are summarized in Table 14:

Elastic Part	σ'_f (MPa) =	389.351
	b =	-0.117
Plastic Part	ε'_f =	0.272
	c =	-0.563

Table 14. Coffin-Manson parameters- ZEK100-O

The life predictions using the SWT parameters given in Table 14 versus experimental lives are shown in Figure 108:

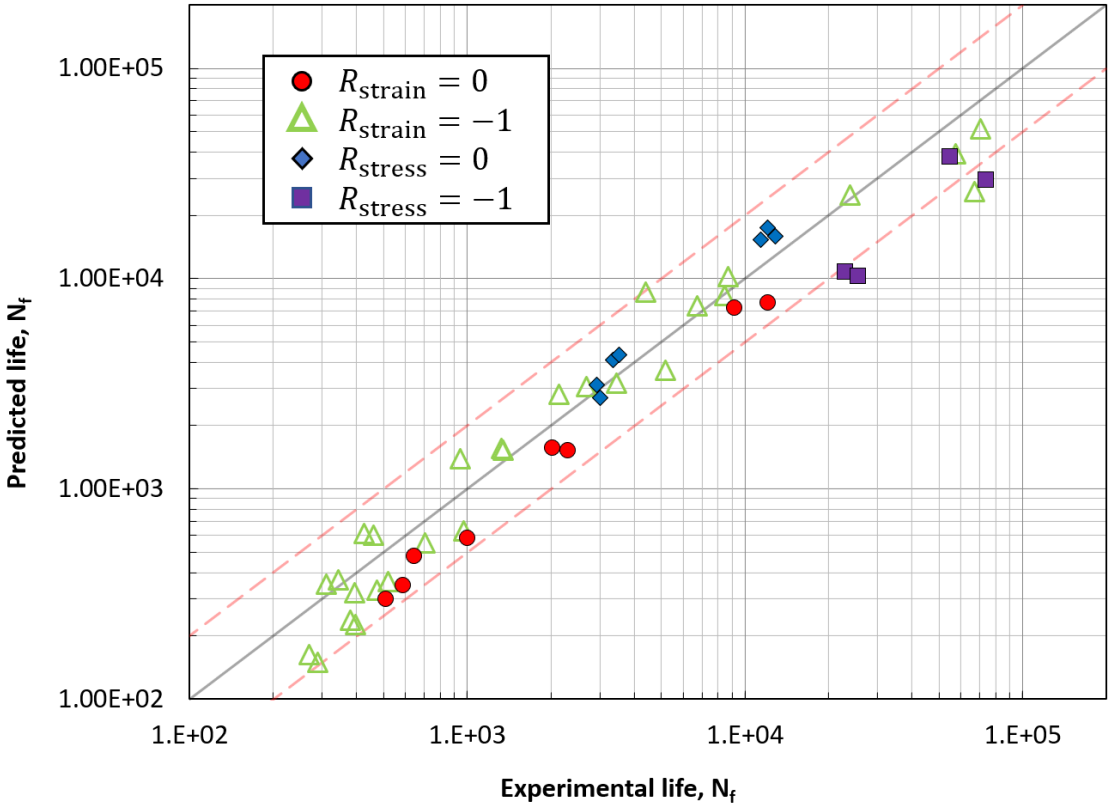

Figure 108. Predicted life using the SWT model vs. experimental life for $R_{strain} = 0$, $R_{strain} = -1$, $R_{stress} = 0$ and $R_{stress} = -1$ tests using the SWT parameters given in Table 14- ZEK100-O

The black diagonal line represents the best prediction whereas the dashed red lines represent the factor of 2 bounds between the experimental life and the model prediction.

It can be seen that most of the results are falling in between the factor of 2 bound. However, as what have been mentioned during the derivation of the SWT model from Coffin-Manson relation, the fully-reversed strain-controlled tests have been used to obtain the SWT parameters were assumed to be fully-reversed in stress as well, which is not the case for magnesium alloys due to the tension-compression asymmetry. Although the tension-compression asymmetry for ZEK100-O is weakened by the additional rare-earth element neodymium compare with other types of magnesium alloys as mentioned in chapter 2, the asymmetry still presents.

To take the mean stress of the fully-reversed strain-controlled tests into consideration, instead of fitting the Coffin-Manson relations to the strain amplitude versus life curve, Equation (82) is directly used to fit the strain amplitude versus life curve in a form shown in Equation (83):

$$\sigma_{max}\varepsilon_a = A_1(2N_f)^{b_1} + A_2(2N_f)^{b_2} \quad (83)$$

The fitting parameters for Equation (83) is given in:

Parameter	Fitted values
A_1 [MPa]	3928.389
A_2 [MPa]	-1.225
b_1	4.361
b_2	-0.231

Table 15. Parameters by fitting Equation (83) to the strain amplitude versus life curve- ZEK100-O

The parameters shown in Table 15 can be converted to the form of SWT parameters shown in:

Elastic Part	σ'_f (MPa)	438.593
	b	-0.116
Plastic Part	ε'_f	8.956798
	c	-1.109

Table 16. SWT direct-fit parameters- ZEK100-O

Using the parameters shown in Table 16 (later referred to the SWT direct-fit), the predicted life vs. experimental life plot for ZEK100-O is shown in Figure 109:

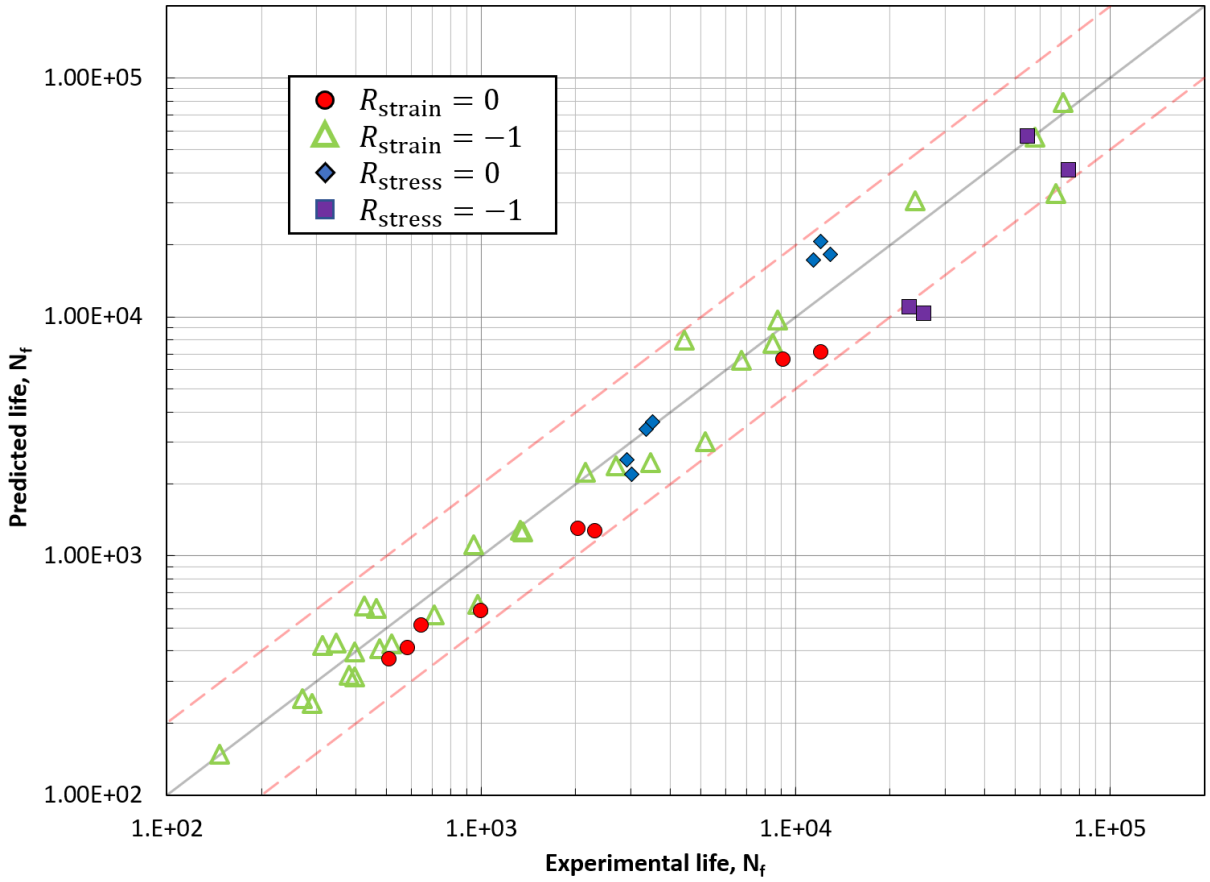

Figure 109. The predicted life using SWT direct-fit vs. experimental life- ZEK100-O

It can be seen that the predictions within the low-cycle region are greatly improved and some improvements can also be observed in the high-cycle region.

5.2 Jahed-Varvani (J-V energy) model

In addition to the SWT model, an energy-based model has also been considered to model the fatigue behavior of ZEK100-O magnesium alloy. Energy-based fatigue models generally have the advantage on the modeling of asymmetric/anisotropic materials since the damage is directly linked to the strain energy density of each cycle.

The Jahed-Varvani model (later referred as the J-V energy model) proposed by Jahed and Varvani [8] [9] and has been used widely (e.g., [100] [102]) is given in Equation (84):

$$\Delta E = {E'}_e\left(2N_f\right)^B + {E'}_f\left(2N_f\right)^C \quad (84)$$

Where ${E'}_e$ is the fatigue strength coefficient, B is the fatigue strength exponent, ${E'}_f$ is the fatigue toughness coefficient, C is the fatigue toughness exponent, N_f is the reversals to failure and ΔE is the total strain energy density for a completed cycle, consist of the positive elastic and plastic parts, shown in Equation (85):

$$\Delta E = {\Delta E_e}^+ + \Delta E_p \quad (85)$$

The plastic strain energy density is given by the area enclosed by the stress-strain hysteresis loop, and the positive elastic strain energy density is given by Equation (86):

$${\Delta E_e}^+ = \frac{{\sigma_{max}}^2}{2E} \quad (86)$$

The strain energy densities of the stabilized stress-strain hysteresis loops were calculated and plotted against the reversal to failure as shown in Figure 110:

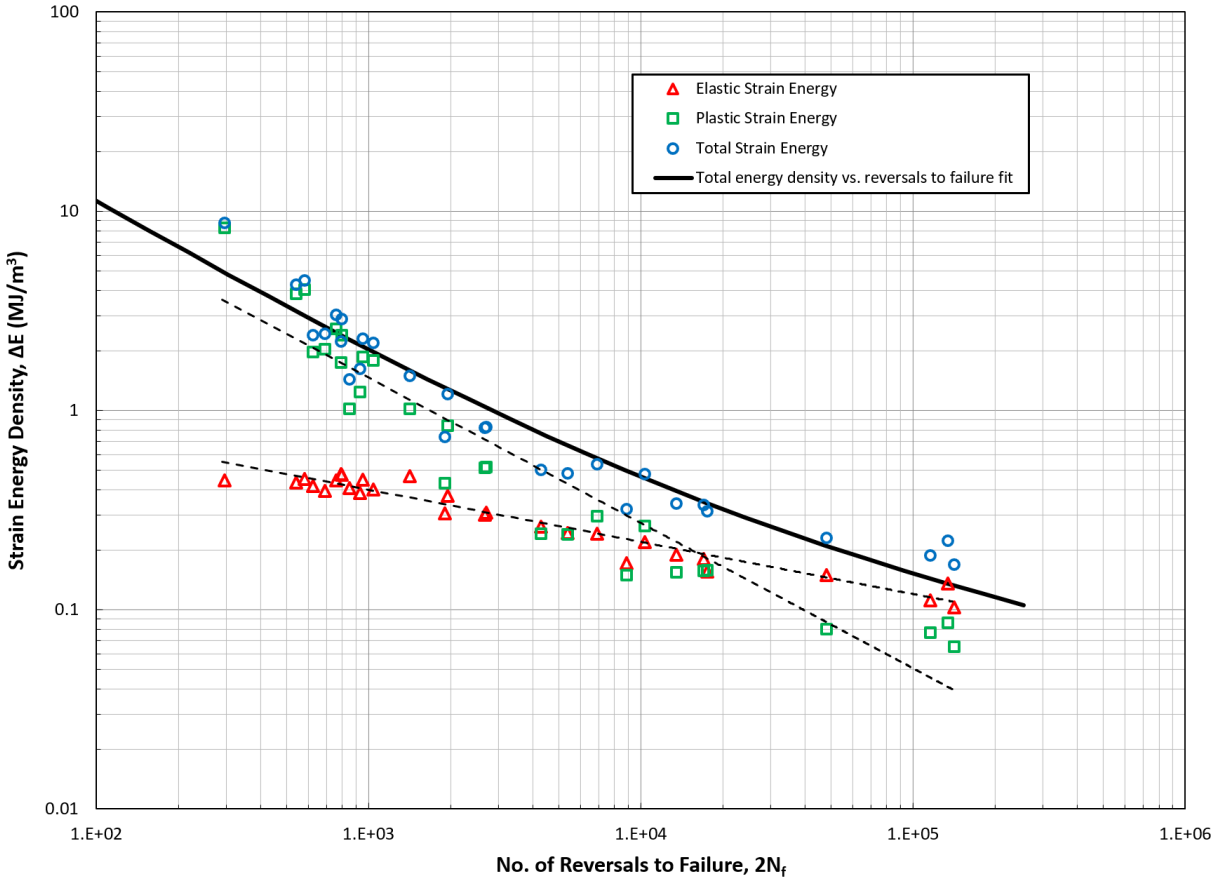

Figure 110. Strain energy density vs. reversals to failure and the curve fitted with Equation (84) - ZEK100-O

Equation (84) is fitted to the total energy versus reversals to failure curve analogous to Coffin-Manson relation and the J-V energy parameters are given in Table 17:

Elastic Part	E'_e =	2.771
	B =	-0.277
Plastic Part	E'_f =	443.662
	C =	-0.813

Table 17. J-V energy model parameters- ZEK100-O

The life predictions using J-V energy parameters given in Table 17 are shown in:

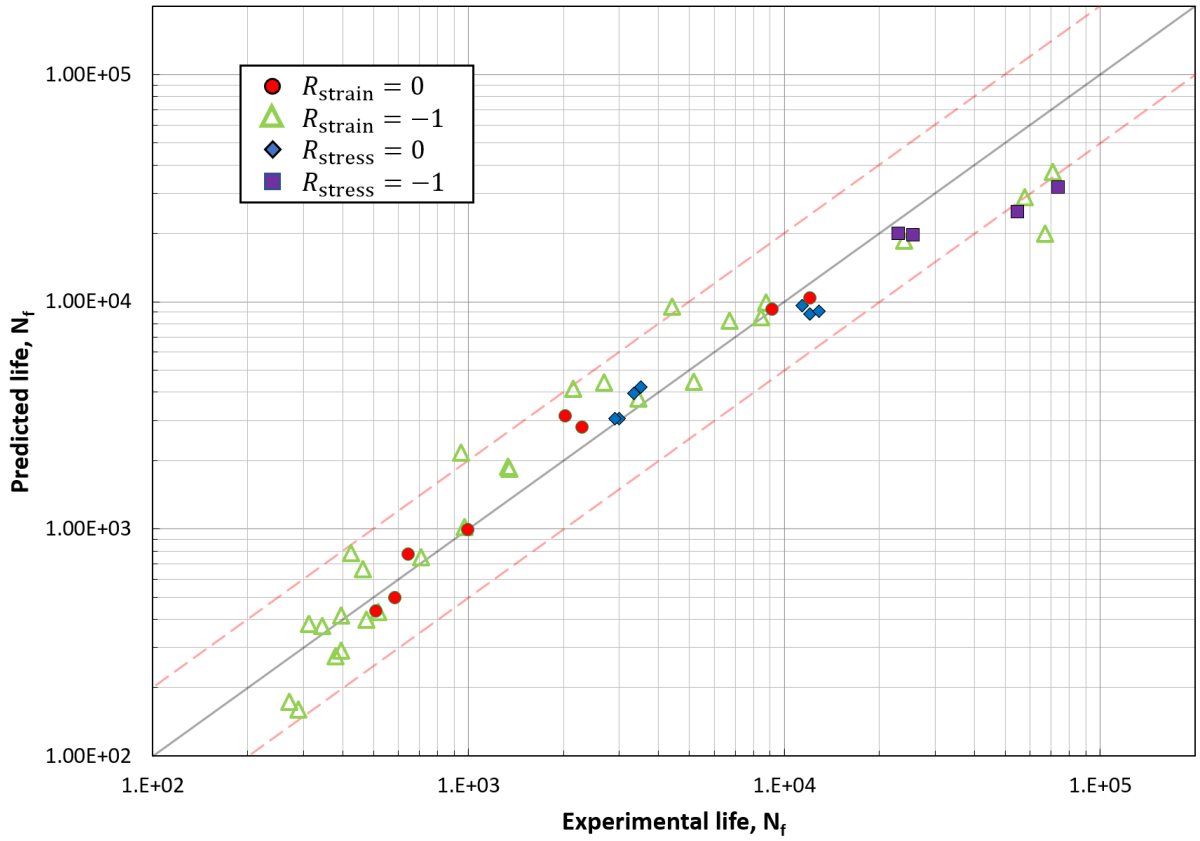

Figure 111. The predicted life using J-V energy model vs. experimental life- ZEK100-O

Even though there are few points land outside of the factor of 2 bounds on the high-cycle side, the majority of the points are within the bounds and the predictions using J-V energy model are considered as good.

5.3 Damage accumulation for variable amplitude loading

In the case of variable amplitude loading, because of the variation of the stress/strain amplitudes from cycle to cycle, some types of damage accumulation rules have to be. For this purpose, the Palmgren-Miner rule is used to taking the damage contribution of individual cycles into consideration.

The Palmgren-Miner rule is shown in Equation (87):

$$\sum_{i=1}^{k} \frac{n_i}{N_i} = C \qquad (87)$$

Where n_i is the number of cycles accumulated for a certain stress/strain amplitude within a given load history, N_i is the number of cycles to failure for that stress/strain amplitude and C is the fraction of the life consumed for that load history. Failure will occur when the value of C reaches 1. Therefore, the number of times a given load history can be allied before the final failure is:

$$N_f = \frac{1}{C} = \frac{1}{\sum_{i=1}^{k} \frac{n_i}{N_i}} \qquad (88)$$

Where N_f is the number of blocks of a given load history can be applied before the final failure.

The variable amplitude strain-controlled tests on smooth sample shown in Figure 56 - Figure 59 are used to evaluate the Palmgren-Miner rule on ZEK100-O. The damage distribution by SWT direct-fit and J-V energy model for all four tests aside with its corresponding strain histories are shown in Figure 112 - Figure 115:

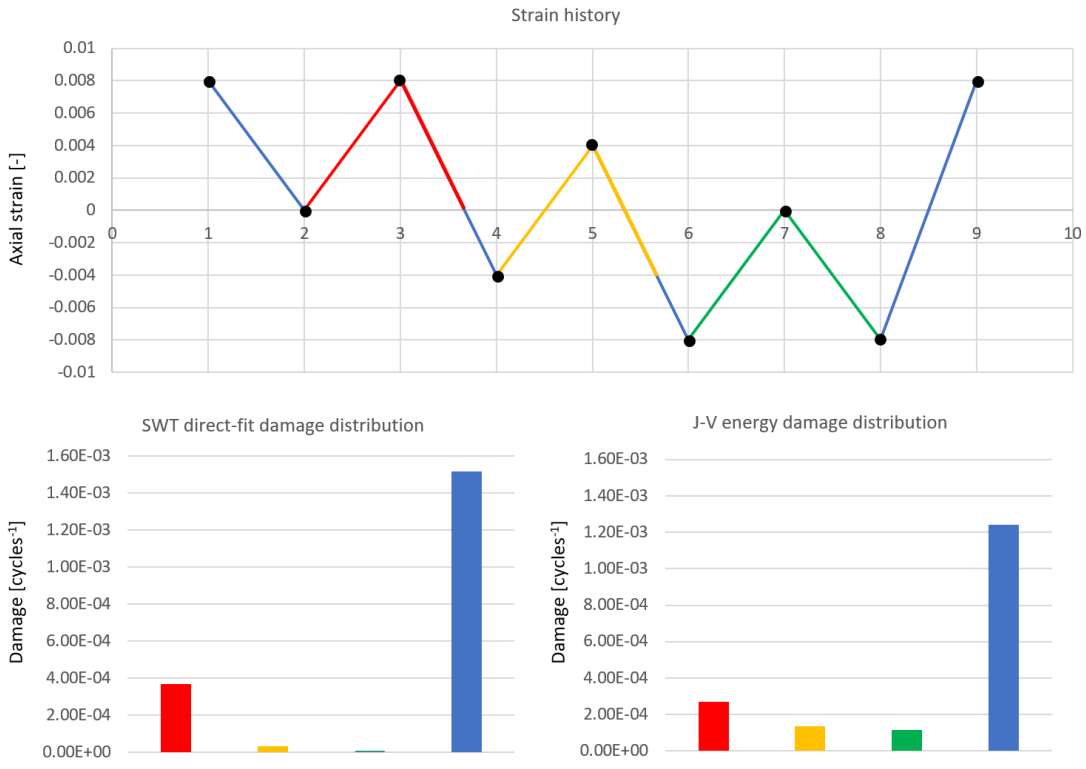

Figure 112. Strain history and damage distribution by SWT direct-fit and J-V energy model for the variable amplitude strain-controlled test # 1 - ZEK100-O

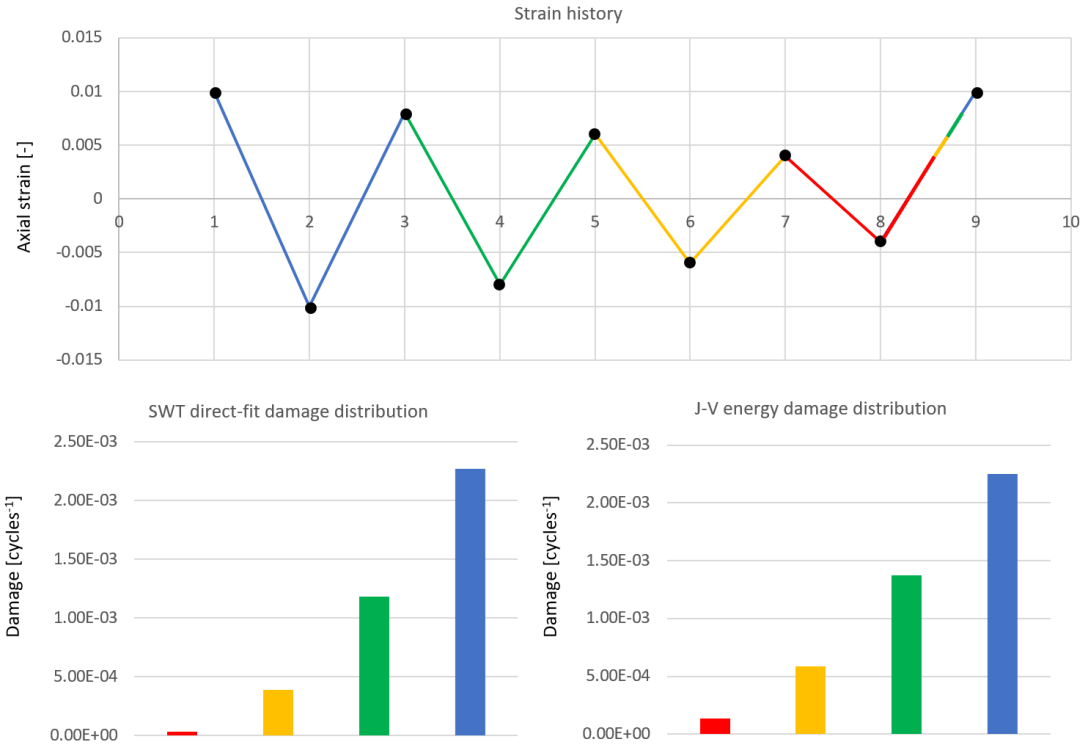

Figure 113. Strain history and damage distribution by SWT direct-fit and J-V energy model for the variable amplitude strain-controlled test # 2 - ZEK100-O

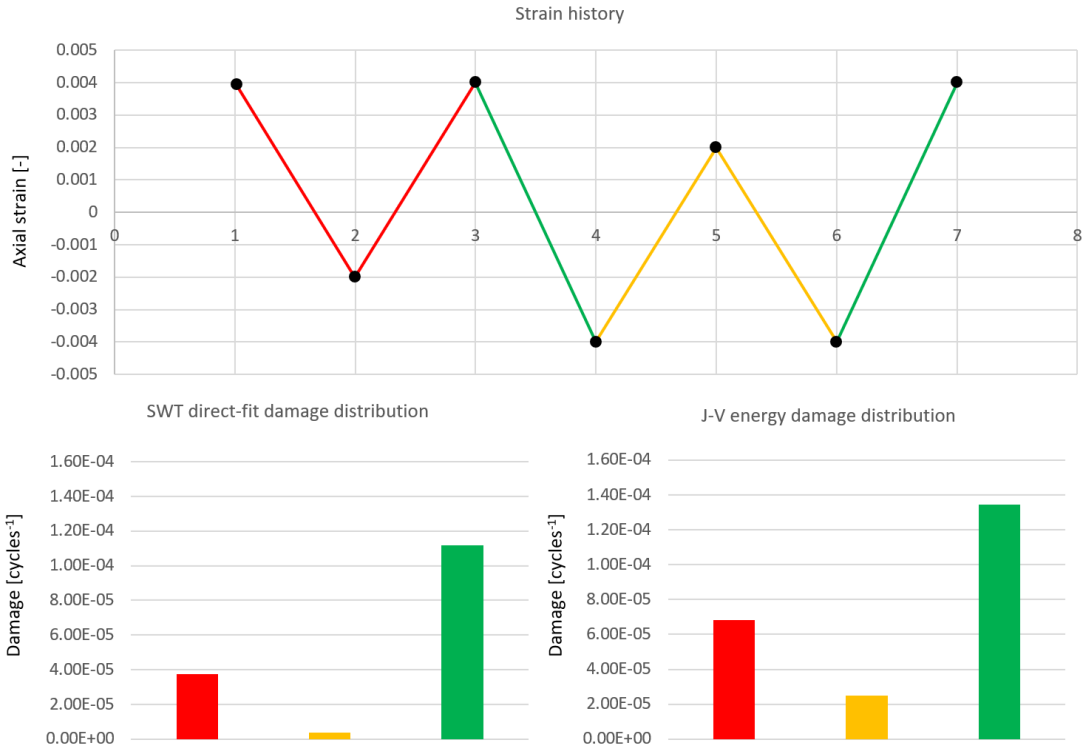

Figure 114. Strain history and damage distribution by SWT direct-fit and J-V energy model for the variable amplitude strain-controlled test # 3 - ZEK100-O

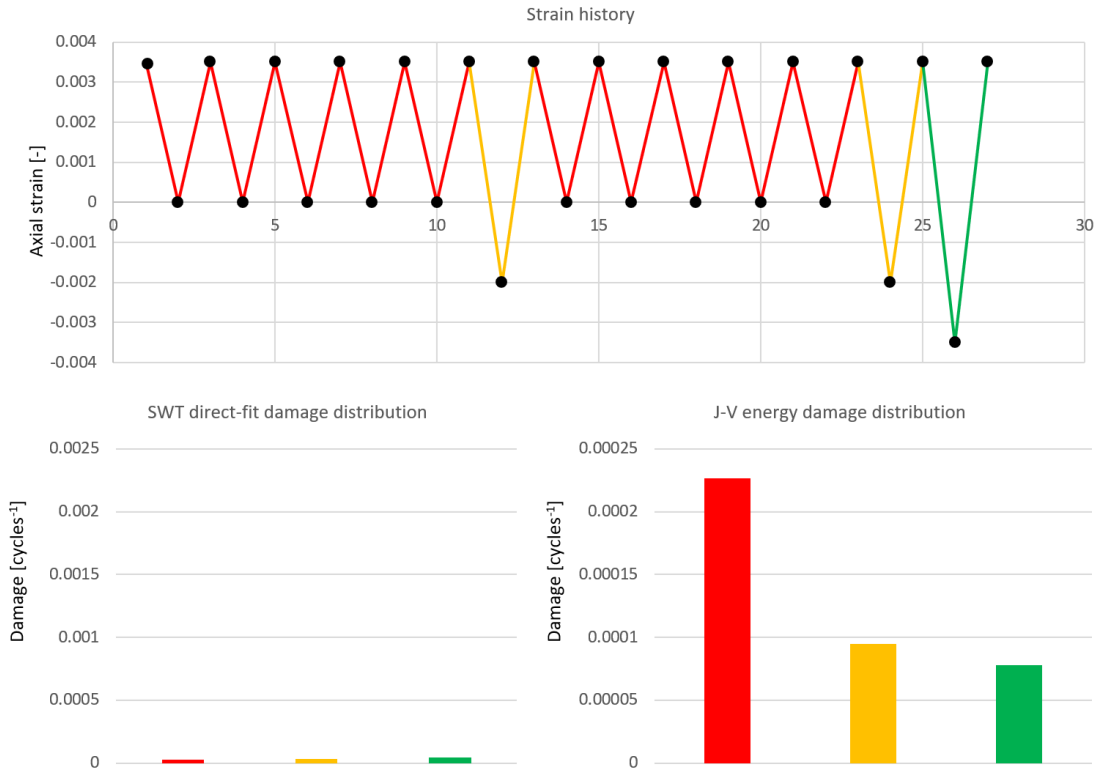

Figure 115. Strain history and damage distribution by SWT direct-fit and J-V energy model for the variable amplitude strain-controlled test # 4 - ZEK100-O

The predictions using both SWT direct-fit and Jahed-Varvani models are summarized in Table 18:

Test #	Experimental life (blocks)	SWT-direct fit (blocks)	J-V energy model (blocks)
1	545	520	567
2	206	258	229
3	4130	6538	4405
4	3900	9571	2505

Table 18. Experimental life vs. SWT direct-fit and J-V energy model predictions of variable amplitude strain-controlled tests on smooth specimens- ZEK100-O

It can be seen that both SWT direct-fit and Jahed-Varvani models give very good predictions for all four tests, however, the predictions using J-V energy model give better results especially for test number 3 and test number 4.

Therefore, it can be concluded that:

i. The Palmgren-Miner rule is working for ZEK100-O magnesium alloy.
ii. Both SWT direct-fit and Jahed-Varvani models can very well predict the fatigue life of ZEK100-O.
iii. Jahed-Varvani model gives better predictions compare with SWT-direct fit for ZEK100-O.

5.4 Fatigue life prediction for notched specimens

The fatigue life predictions of the notched sample tests are compared with the experimentally determined crack-initiation lives at the notch root. In terms of the failure criteria, the notched specimens are deemed as a failure when any crack of length exceeds 100 μm at the vicinity of the notch root is observed on the surface of the specimens. Additionally, the phenomenological model by Dallmeier et al. [5] accompanied with either the Neuber's or Glinka's rule has been used to obtain the local stress-strain responses at the vicinity of the notch root in order to use both SWT direct-fit and Jahed-Varvani fatigue models.

The fatigue lives of the constant nominal stress amplitude fatigue tests on notched specimens summarized in Table 9 is compared with the predictions, shown in Table 19:

Approximation method	**Fatigue model**	**Fatigue life (60%) * (cycles)**	**Fatigue life (80%) * (cycles)**
Experimental	N/A	4500, 5065	900, 710, 1165, 900
Neuber's rule (plane strain)	SWT-Direct fit	1203	455
	J-V energy	1418	384
Glinka's rule (Plane strain with C_p correction)	SWT-Direct fit	1706	611
	J-V energy	2200	610

Table 19. Experimental lives vs. model predictions for ZEK100-O notched specimens under fully-reversed nominal stresses (60% and 80% stand for 60% or 80% of compressive yield equivalent fully-reversed nominal stress been applied to the notched specimen)

Noticed that, all the predictions made by either Neuber's or Glinka's approximation with SWT direct-fit or J-V energy model at 60% and 80% of compressive yield stress equivalent fully-reversed nominal stresses are underpredicting the crack initiation life of the ZEK100-O notched specimens. However, the Neuber's tend to overpredict the notch strains as what has been discussed in chapter 5, which will result in a further underprediction. On the other hand, Glinka's rule with C_p correction has been shown to give a closer to experimental prediction in terms of the notch strains, therefore, a better fatigue life prediction from Glinka's rule is expected. Finally, the predictions given by SWT direct-fit and J-V energy models are not too far away from each other, while the predictions made by J-V energy model are slightly closer to experiments in this case.

In addition to ZEK100-O, the fatigue life of AZ31B-H24 notched specimens are also used to compare with the model predictions, shown in Table 20:

Approximation method	Fatigue model	Fatigue life (60%) * (cycles)	Fatigue life (80%) * (cycles)
Experimental	N/A	5300, 5500	1000, 1380, 900, 1120
Neuber's rule (plane strain)	SWT-Direct fit	980	403
	J-V energy	872	341
Glinka's rule (Plane strain with C_p correction)	SWT-Direct fit	1318	474
	J-V energy	1164	447

Table 20. Experimental lives vs. model predictions for AZ31B-H24 notched specimens under fully-reversed nominal stresses (60% and 80% stand for 60% or 80% of compressive yield equivalent fully-reversed nominal stress been applied to the notched specimen)

Due to the fact that, the deviation of the notch strains between the prediction and the experimental values are relatively larger for both Neuber's and Glinka's rules on AZ31B-H24 compare with ZEK100-O as shown in chapter 5, the relatively larger deviation between the experimental and model predicted life is expected, which is reflected in

Table 20. In contrary to ZEK100-O, predictions by SWT direct-fit tend to be closer to the experiments, however, no conclusion can be drawn without additional tests.

In addition to the constant nominal stress amplitude tests, variable amplitude fatigue tests have been done on notched ZEK100-O specimens as shown in Figure 76 are compared with the predictions using the phenomenological model by Dallmeier et al. with either Neuber's or Glinka's rule to obtain the local stress-strain responses at the notch root, the fatigue life then accessed with SWT direct-fit or J-V energy model accompanied with Palmgren-Miner rule, shown in Table 21:

Approximation method	**Fatigue model**	**Load history #1** (Blocks)	**Load history #2** (Blocks)	**Load history #3** (Blocks)
Experimental	N/A	3980	23800	24100
Neuber's rule (plane strain)	SWT-Direct fit	1909	7564	7214
	J-V energy	1867	4465	3254
Glinka's rule (Plane strain with C_p correction)	SWT-Direct fit	2654	9720	9373
	J-V energy	2288	4862	3675

Table 21. Experimental lives vs. model predictions for ZEK100-O notched specimens under variable amplitude nominal stresses loading (The nominal stress histories for all three tests are given in Figure 76)

A relatively larger deviation between the predicted and experimental lives has been observed for load history #2 and load history #3 compare with load history #1. The reason could be that the modeled strain amplitudes at the notch root are well under the lowest strain amplitude for the fully-reversed strain-controlled tests on the ZEK100-O smooth specimens were used to determine the parameters for SWT direct-fit or J-V energy fatigue models. Other than that, all the predictions for load history #1 are very close and Glinka's rule with C_p correction seems to have the best result.

Chapter 6: MATLAB implementation

The modeling procedures for both smooth and notched samples analysis as described in chapter 4 have been coded in MATLAB. In addition, the fatigue modeling using SWT direct-fit and J-V energy models have also been integrated to predict the fatigue life for a given load history.

There are 3 inputs needed for each analysis:

i. A single stabilized hysteresis with visible twinning exhaustion (>2% strain amplitude)
ii. Experimentally obtained cyclic stress-strain curve (CSSC)
iii. Load history (strain history for smooth sample analysis and nominal stress history for notch samples)

However, the built-in material library has already included ZEK100-O and AZ31B-H24 properties and can be expanded later as needed. Therefore, the load history will be the only input needed for the existing materials in the material library.

The output capabilities for the MATLAB program are:

i. Stress-strain hysteresis loops prediction for magnesium alloys given the strain history
ii. Fatigue life predictions using SWT direct-fit or J-V energy model for the given strain history
iii. The localized stress-strain hysteresis loops prediction at the vicinity of the notch root for magnesium alloys given the stress history using Neuber's or Glinka's approximation method
iv. Fatigue crack initiation life predictions at the notch root using SWT direct-fit or J-V energy model for the given nominal stress history

The flow diagrams for the phenomenological model, notch analysis using Neuber's/Glinka's rule and life prediction are shown in Figure 116 - Figure 118:

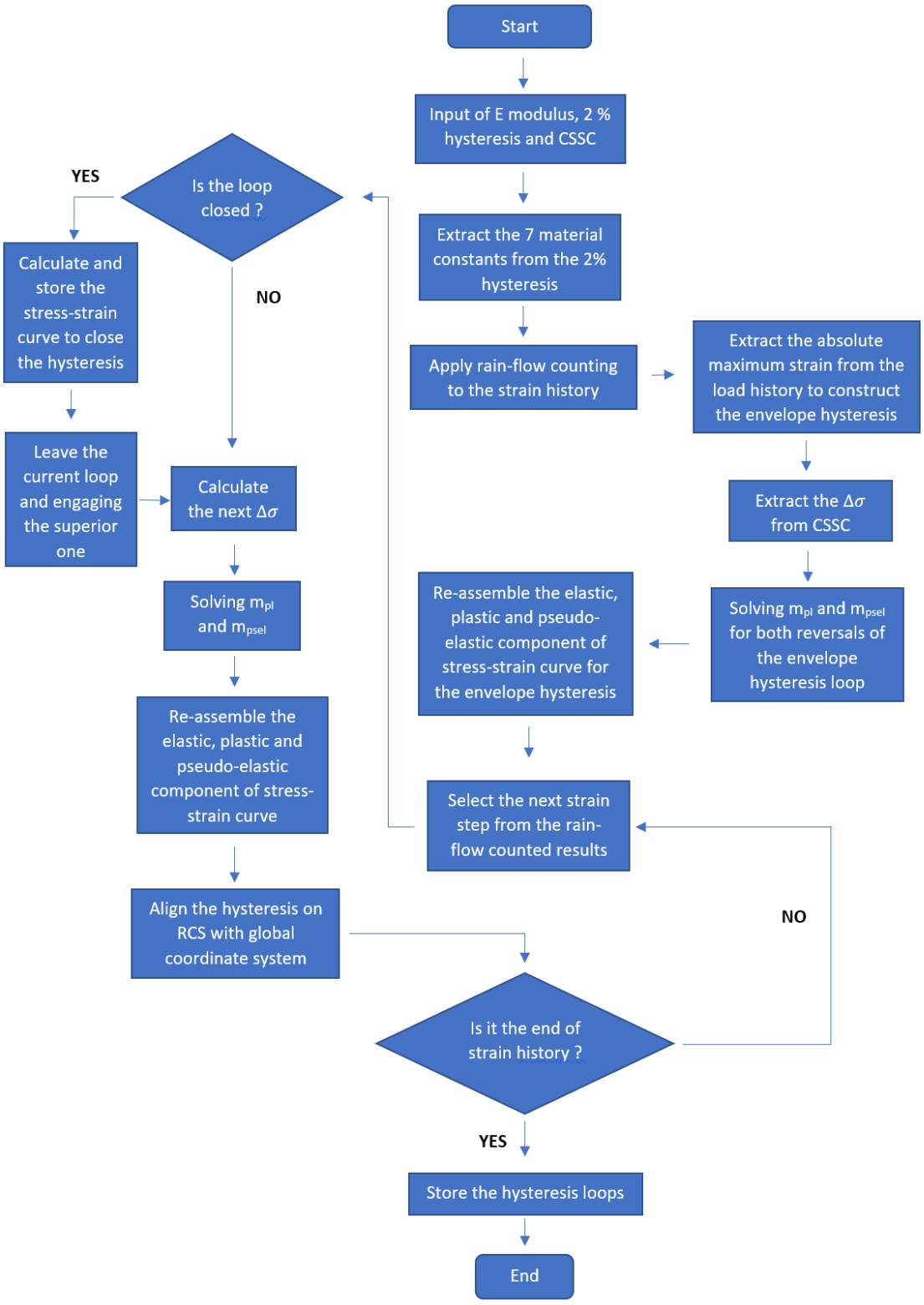

Figure 116. Flow diagram for the implementation of the phenomenological model by Dallmeier et al [5]

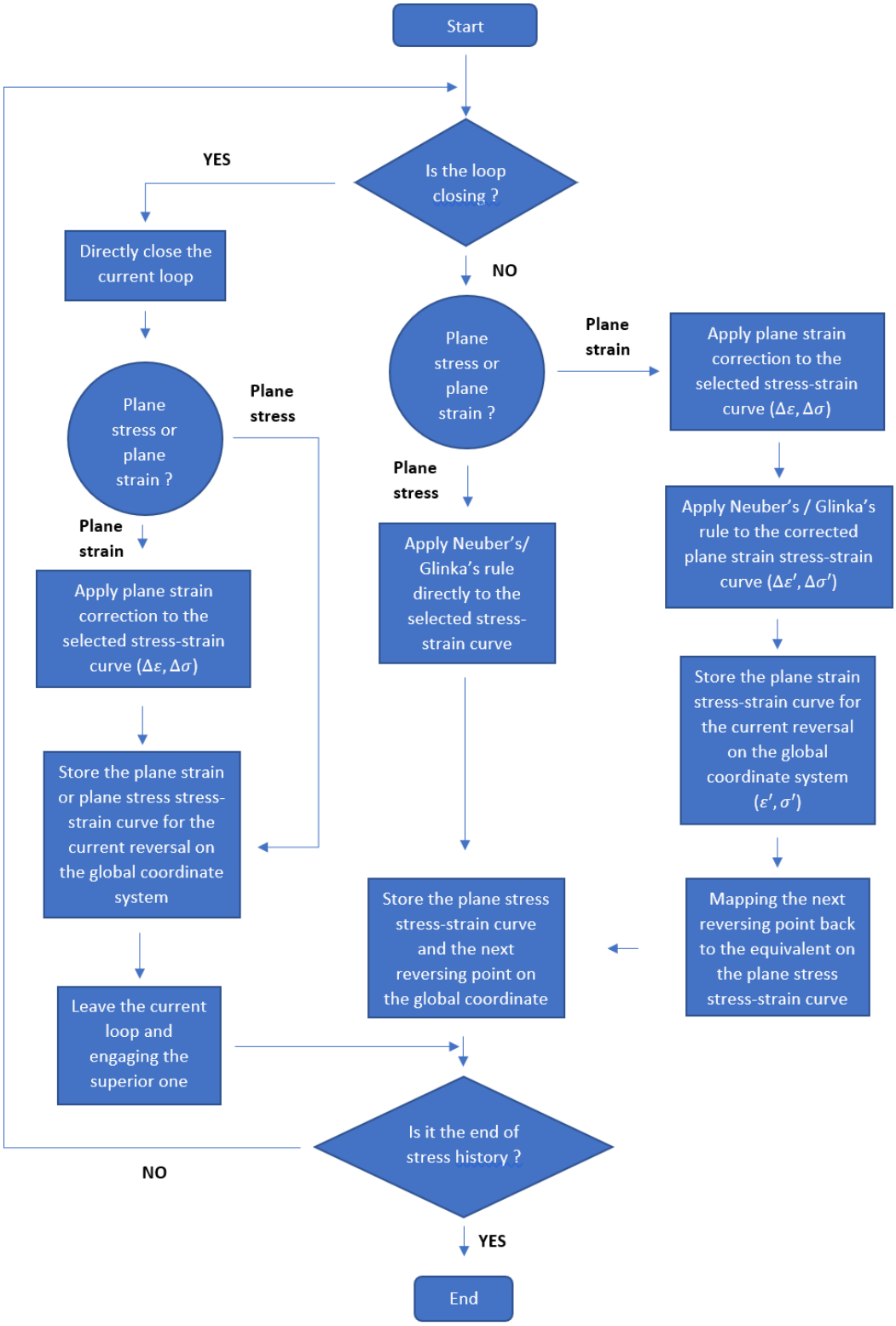

Figure 117. Flow diagram for the notch analysis using Neuber's/ Glinka's rule

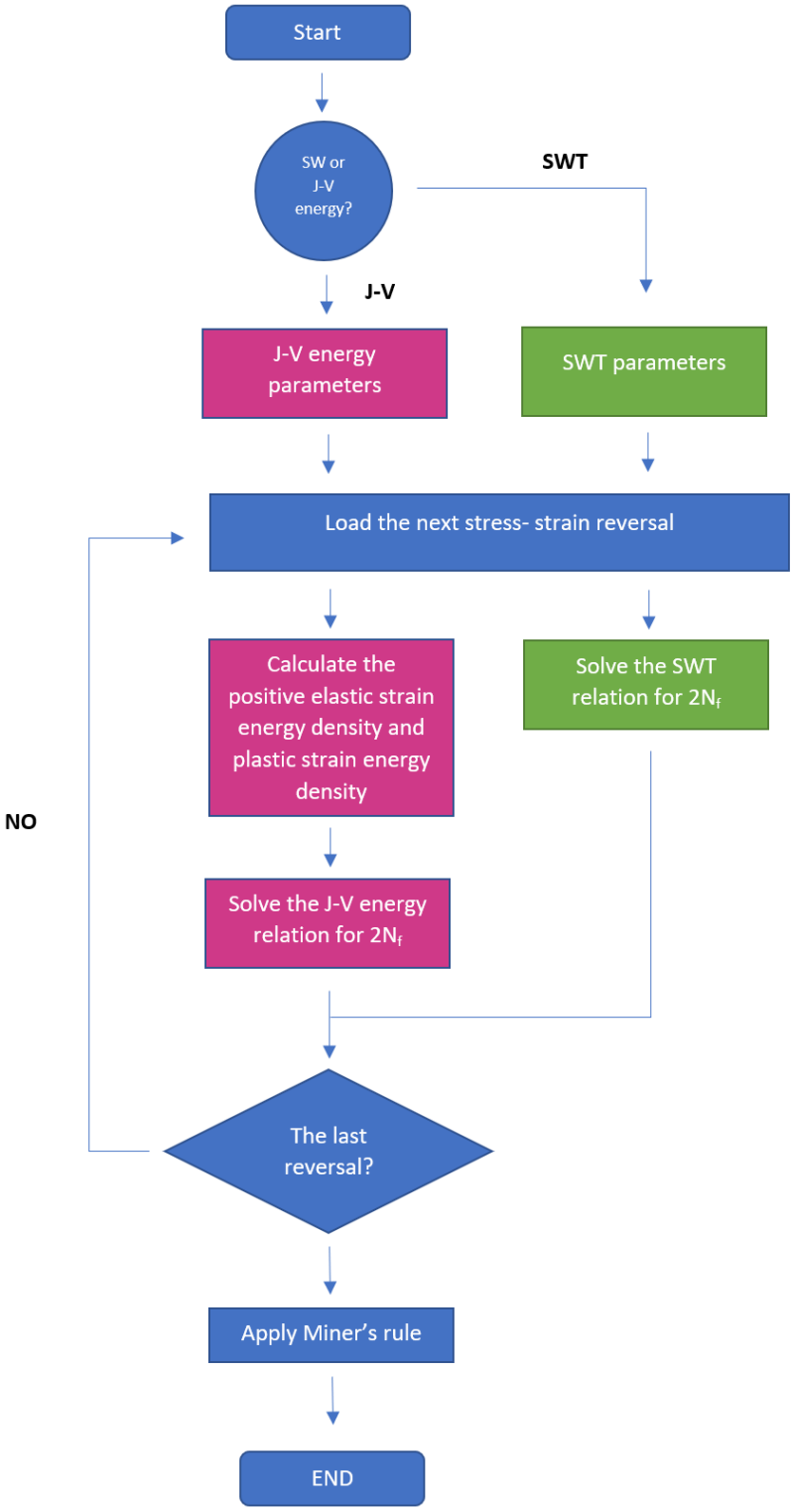

Figure 118. Flow diagram for the implementation of the life prediction using SWT or J-V energy model

Chapter 7: Conclusion and Future Work

7.1 Conclusions:

At the end of this thesis, these things can be concluded:

i. ZEK100-O magnesium alloy have relatively weaker basal texture due to the inclusion of the rare-earth element neodymium, and the basal poles have a spread along the transverse direction.
ii. ZEK100-O magnesium alloy has relatively weaker tension-compression asymmetry and relatively stronger planar anisotropy.
iii. ZEK100-O magnesium alloy has good formability due to its high ductility.
iv. The axial strain at the notch root for both ZEK100-O and AZ31B-H24 will be stabilized under fully-reversed nominal stress.
v. The phenomenological model by Dallmeier et al. is able to mimic the sigmoidal-shaped stress-strain behaviors of both ZEK100-O and AZ31B-H24 magnesium alloys.
vi. Both Neuber's and Glinka's rules (ESED) are able to predict the localized notch strain with reasonable accuracy for both ZEK100-O and AZ31B-H24.
vii. The notch strain predictions are given by Glinka's rule (ESED) with C_p corrections are closer to experiments
viii. The original SWT model does not take the tension-compression asymmetry of the fully-reversed strain-controlled tests into consideration.
ix. Direct fitting the strain-life curve to the SWT model will take the mean stresses caused by the tension-compression asymmetry on the fully-reversed strain-controlled tests into consideration.
x. Both SWT direct-fit and J-V energy models give good predictions on the fatigue life of ZEK100-O magnesium alloy.
xi. The MATLAB program developed is able to predict the stress-strain hysteresis loops as well as the fatigue life of smooth specimens given the strain history with a reasonable accuracy.
xii. The MATLAB program developed is able to predict the stress-strain responses at the notch root using either Neuber's or Glinka's method for a given nominal stress history as well as the fatigue crack initiation life of the notched specimens with a reasonable accuracy.

7.2 Future Work:

The suggested future works are listed below:

- Additional fully-reversed strain-controlled tests at and below 0.3% strain amplitude are needed to improve the fatigue model predictions in the high-cycle regime.
- Current test results have shown a trend that, the mean strains have little effect on the fatigue life of ZEK100-O, however, additional tests have to be done to confirm it.
- The specimens have been used for ZEK100-O notched tests are 6.6 mm thick, which makes the stress state at the notch root to be close to plane strain. Additional tests on thinner specimens are beneficial to confirm the plane stress solution of the model predictions.
- More efficient numerical methods can be implemented in the developed notch analysis program to improve efficiency and stability.

Reference

[1] Climate change 2001: Impacts, adaptation, and vulnerability. (2002). *Choice Reviews Online, 39*(06). doi:10.5860/choice.39-3433

[2] U.S. Environmental Protection Agency (2018). Inventory of U.S. Greenhouse Gas Emissions and Sinks: 1990-2016

[3] Ball, E., & Prangnell, P. (1994). Tensile-compressive yield asymmetries in high strength wrought magnesium alloys. *Scripta Metallurgica Et Materialia, 31*(2), 111-116. doi:10.1016/0956-716x(94)90159-7

[4] Habib, S. A., Khan, A. S., Gnäupel-Herold, T., Lloyd, J. T., & Schoenfeld, S. E. (2017). Anisotropy, tension-compression asymmetry and texture evolution of a rare-earth-containing magnesium alloy sheet, ZEK100, at different strain rates and temperatures: Experiments and modeling. *International Journal of Plasticity, 95*, 163-190. doi:10.1016/j.ijplas.2017.04.006

[5] Dallmeier, J., Denk, J., Huber, O., Saage, H., & Eigenfeld, K. (2015). A phenomenological stress–strain model for wrought magnesium alloys under elastoplastic strain-controlled variable amplitude loading. *International Journal of Fatigue, 80*, 306-323. doi:10.1016/j.ijfatigue.2015.06.007

[6] Dowling, N. E. (2013). *Mechanical behavior of materials: Engineering methods for deformation, fracture, and fatigue*. Harlow, Essex, England: Pearson Education Limited.

[7] K.N. Smith, P. Watson, T.H. Topper, A stress–strain functions for the fatigue of metals, *J. Mater. 5* (1970) 767–778.

[8] Jahed, H., & Varvanifarahani, A. (2006). Upper and lower fatigue life limits model using energy-based fatigue properties. *International Journal of Fatigue, 28*(5-6), 467-473. doi:10.1016/j.ijfatigue.2005.07.039

[9] Jahed, H., Varvanifarahani, A., Noban, M., & Khalaji, I. (2007). An energy-based fatigue life assessment model for various metallic materials under proportional and non-proportional loading conditions. *International Journal of Fatigue, 29*(4), 647-655. doi:10.1016/j.ijfatigue.2006.07.017

[10] Casey, J., & Jahedmotlagh, H. (1984). The strength-differential effect in plasticity. *International journal of solids and structures*, *20*(4), 377-393.

[11] Rokhlin, L. L. (2003). *Magnesium alloys containing rare earth metals: Structure and properties*. London: Taylor and Francis.

[12] Fan, H., & El-Awady, J. A. (2015). Molecular Dynamics Simulations of Orientation Effects During Tension, Compression, and Bending Deformations of Magnesium Nanocrystals. *Journal of Applied Mechanics, 82*(10), 101006. doi:10.1115/1.4030930

[13] Groves, G. W., & Kelly, A. (1963). Independent slip systems in crystals. *Philosophical Magazine, 8*(89), 877-887. doi:10.1080/14786436308213843

[14] Chapuis, A., & Driver, J. H. (2011). Temperature dependency of slip and twinning in plane strain compressed magnesium single crystals. *Acta Materialia, 59*(5), 1986-1994. doi:10.1016/j.actamat.2010.11.064

[15] Wang, Y., & Huang, J. (2003). Texture analysis in hexagonal materials. *Materials Chemistry and Physics, 81*(1), 11-26. doi:10.1016/s0254-0584(03)00168-8

[16] Yoo, M. H. (1981). Slip, twinning, and fracture in hexagonal close-packed metals. *Metallurgical Transactions A, 12*(3), 409-418. doi:10.1007/bf02648537
[17] Wonsiewicz, B.C., 1966. Plasticity of Magnesium Crystals. *Doctoral dissertation. Massachusetts Institute of Technology.*
[18] Wonsiewicz, B.C., 1966. Plasticity of Magnesium Crystals. *Doctoral dissertation. Massachusetts Institute of Technology.*
[19] Nave, M. D., & Barnett, M. R. (2004). Microstructures and textures of pure magnesium deformed in plane-strain compression. *Scripta Materialia, 51*(9), 881-885. doi:10.1016/j.scriptamat.2004.07.002
[20] Ardeljan, M., Beyerlein, I.J., McWilliams, B.A., Knezevic, M., 2016a. Strain rate and temperature sensitive multi-level crystal plasticity model for large plastic deformation behavior: application to AZ31 magnesium alloy. Int. J. Plast. 83, 90e109.
[21] Hong, S., Park, S. H., & Lee, C. S. (2010). Role of {10–12} twinning characteristics in the deformation behavior of a polycrystalline magnesium alloy. *Acta Materialia, 58*(18), 5873-5885. doi:10.1016/j.actamat.2010.07.002
[22] Muhammad, W., Mohammadi, M., Kang, J., Mishra, R. K., & Inal, K. (2015). An elasto-plastic constitutive model for evolving asymmetric/anisotropic hardening behavior of AZ31B and ZEK100 magnesium alloy sheets considering monotonic and reverse loading paths. *International Journal of Plasticity, 70*, 30-59. doi:10.1016/j.ijplas.2015.03.004
[23] Lou, X.Y., Li, M., Boger, R.K., Agnew, S.R., Wagoner, R.H., 2007. Hardening evolution of AZ31B Mg sheet. *Int. J. Plast.* 23 (1), 44e86
[24] Kaiser, F., Bohlen, J., Letzig, D., Kainer, K.U., Styczynski, A., Hartig, C., 2003. Influence of rolling conditions on the microstructure and mechanical properties of magnesium sheet AZ31. Adv. Eng. Mater. 5, 891e896.
[25] Gryguc, A., Shaha, S. K., Behravesh, S. B., Jahed, H., Wells, M., Williams, B., & Su, X. (2017). Monotonic and cyclic behaviour of cast and cast-forged AZ80 Mg. *International Journal of Fatigue*, *104*, 136-149.
[26] Kalatehmollaei, E., Mahmoudi-Asl, H., & Jahed, H. (2014). An asymmetric elastic–plastic analysis of the load-controlled rotating bending test and its application in the fatigue life estimation of wrought magnesium AZ31B. *International Journal of Fatigue*, *64*, 33-41.
[27] Karparvarfard, S. M. H., Shaha, S. K., Behravesh, S. B., Jahed, H., & Williams, B. W. (2017). Microstructure, texture and mechanical behavior characterization of hot forged cast ZK60 magnesium alloy. *Journal of Materials Science & Technology*, *33*(9), 907-918.
[28] Roostaei, A. A., & Jahed, H. (2016). Role of loading direction on cyclic behaviour characteristics of AM30 extrusion and its fatigue damage modelling. *Materials Science and Engineering: A*, *670*, 26-40.
[29] Jain, A., Agnew, S.R., 2007. Modeling the temperature dependent effect of twinning on the behavior of magnesium alloy AZ31B sheet. *Mater. Sci. Eng. A* 462 (1), 29e36.
[30] Abedini, A., Butcher, C., Nemcko, M., Kurukuri, S., & Worswick, M. (2017). Constitutive characterization of a rare-earth magnesium alloy sheet (ZEK100-O) in shear loading: Studies of anisotropy and rate sensitivity. *International Journal of Mechanical Sciences, 128-129*, 54-69. doi:10.1016/j.ijmecsci.2017.04.013
[31] Kamrani, S., & Fleck, C. (2014). Effects of calcium and rare-earth elements on the microstructure and tension–compression yield asymmetry of ZEK100 alloy. *Materials Science and Engineering: A, 618*, 238-243. doi:10.1016/j.msea.2014.09.023

[32] Bohlen, J., Nurnberg, M.R., Senn, J.W., Letzig, D., Agnew, S.R., 2007. The texture and anisotropy of magnesium-zinc-rare earth alloy sheets. *Acta Mater*. 55, 2101e2112.

[33] Albinmousa, J., Jahed, H., & Lambert, S. (2011). Cyclic behaviour of wrought magnesium alloy under multiaxial load. *International Journal of Fatigue*, *33*(8), 1127-1139.

[34] Albinmousa, J., Jahed, H., & Lambert, S. (2011). Cyclic axial and cyclic torsional behaviour of extruded AZ31B magnesium alloy. *International Journal of Fatigue*, *33*(11), 1403-1416.

[35] Jahed, H., & Albinmousa, J. (2014). Multiaxial behaviour of wrought magnesium alloys–A review and suitability of energy-based fatigue life model. *Theoretical and Applied Fracture Mechanics*, *73*, 97-108.

[36] Gryguc, A., Shaha, S. K., Jahed, H., Wells, M., Williams, B., & McKinley, J. (2016). Tensile and fatigue behaviour of as-forged AZ31B extrusion. *Frattura ed Integrità Strutturale*, *10*(38), 251-258.

[37] Dayani, S. B., Shaha, S. K., Ghelichi, R., Wang, J. F., & Jahed, H. (2018). The impact of AA7075 cold spray coating on the fatigue life of AZ31B cast alloy. *Surface and Coatings Technology*, *337*, 150-158.

[38] ANDREW, G., HAMID, J., BRUCE, W., & JONATHAN, M. (2015, July). MagForge-Mechanical Behaviour of Forged AZ31B Extruded Magnesium in Monotonic Compression. In *Materials Science Forum*.

[39] Marzbanrad, B., Toyserkani, E., & Jahed, H. (2017). Cyclic hysteresis of AZ31B extrusion under load-control tests using embedded sensor technology. *Fatigue & Fracture of Engineering Materials & Structures*, *40*(2), 221-232.

[40] Noban, M., Albinmousa, J., Jahed, H., & Lambert, S. (2011). A continuum-based cyclic plasticity model for AZ31B magnesium alloy under proportional loading. *Procedia Engineering*, *10*, 1366-1371.

[41] Behravesh, S. B., Jahed, H., & Lambert, S. (2011). Characterization of magnesium spot welds under tensile and cyclic loadings. *Materials & Design*, *32*(10), 4890-4900.

[42] Behravesh, S. B. (2013). Fatigue Characterization and Cyclic Plasticity Modeling of Magnesium Spot-Welds.

[43] Behravesh, S. B., Jahed, H., Lambert, S. B., & Chengji, M. (2014). Constitutive modeling for cyclic behavior of AZ31B magnesium alloy and its application. In *Advanced Materials Research* (Vol. 891, pp. 809-814). Trans Tech Publications.

[44] Sun, M., Behravesh, S. B., Wu, L., Zhou, Y., & Jahed, H. (2017). Fatigue behaviour of dissimilar Al 5052 and Mg AZ31 resistance spot welds with Sn-coated steel interlayer. *Fatigue & Fracture of Engineering Materials & Structures*, *40*(7), 1048-1058.

[45] Toscano, D., Shaha, S. K., Behravesh, B., Jahed, H., & Williams, B. (2017). Effect of forging on the low cycle fatigue behavior of cast AZ31B alloy. *Materials Science and Engineering: A*, *706*, 342-356.

[46] Karparvarfard, S. M. H., Shaha, S. K., Behravesh, S. B., Jahed, H., & Williams, B. W. (2018). Fatigue characteristics and modeling of cast and cast-forged ZK60 magnesium alloy. *International Journal of Fatigue*.

[47] Karparvarfard, S. M. H., Shaha, S. K., Behravesh, S. B., Jahed, H., & Williams, B. W. (2017). Microstructure, texture and mechanical behavior characterization of hot forged cast ZK60 magnesium alloy. *Journal of Materials Science & Technology*, *33*(9), 907-918.

[48] Hadadzadeh, A., Wells, M. A., Shaha, S. K., Jahed, H., & Williams, B. W. (2017). Role of compression direction on recrystallization behavior and texture evolution during hot deformation of extruded ZK60 magnesium alloy. *Journal of Alloys and Compounds*, *702*, 274-289.

[49] Albinmousa, J., Pascu, A., Jahed, H., Horstemeyer, M. F., Luo, A., Chen, D., ... & Duan, Q. Q. (2010). *Monotonic and Fatigue Behavior of Magnesium Extrusion Alloy AM30: An International Benchmark Test in the "Magnesium Front End Research and Development Project"* (No. 2010-01-0407). SAE Technical Paper.

[50] Jahadi, R., Sedighi, M., & Jahed, H. (2017). Effects of aluminum and copper cover tube casing on the ECAP process of AM30 magnesium alloy. *Materials and Manufacturing Processes*, *32*(12), 1375-1383.
[51] Jahadi, R., Sedighi, M., & Jahed, H. (2014). ECAP effect on the micro-structure and mechanical properties of AM30 magnesium alloy. *Materials Science and Engineering: A*, *593*, 178-184.
[52] Roostaei, A. A., & Jahed, H. (2016). Role of loading direction on cyclic behaviour characteristics of AM30 extrusion and its fatigue damage modelling. *Materials Science and Engineering: A*, *670*, 26-40.
[53] Roostaei, A. A., & Jahed, H. (2017). Multiaxial cyclic behaviour and fatigue modelling of AM30 Mg alloy extrusion. *International Journal of Fatigue*, *97*, 150-161.
[54] Roostaei, A. A., & Jahed, H. (2018). A cyclic small-strain plasticity model for wrought Mg alloys under multiaxial loading: Numerical implementation and validation. *International Journal of Mechanical Sciences*, *145*, 318-329.
[55] Gryguc, A., Shaha, S. K., Behravesh, S. B., Jahed, H., Wells, M., Williams, B., & Su, X. (2017). Monotonic and cyclic behaviour of cast and cast-forged AZ80 Mg. *International Journal of Fatigue*, *104*, 136-149.
[56] Gryguc, A., Shaha, S. K., Behravesh, S. B., Jahed, H., Wells, M., & Williams, B. (2017). Compression Behaviour of Semi-closed Die Forged AZ80 Extrusion. In *Characterization of Minerals, Metals, and Materials 2017* (pp. 361-369). Springer, Cham.
[57] Gryguc, A., Behravesh, S. B., Shaha, S. K., Jahed, H., Wells, M., Williams, B., & Su, X. (2018). Low-cycle fatigue characterization and texture induced ratcheting behaviour of forged AZ80 Mg alloys. *International Journal of Fatigue*, *116*, 429-438.
[58] Al-Samman, T., & Li, X. (2011). Sheet texture modification in magnesium-based alloys by selective rare earth alloying. *Materials Science and Engineering: A, 528*(10-11), 3809-3822. doi:10.1016/j.msea.2011.01.080
[59] Mokdad, F., & Chen, D. (2015). Strain-controlled low cycle fatigue properties of a rare-earth containing ZEK100 magnesium alloy. *Materials & Design, 67*, 436-447. doi:10.1016/j.matdes.2014.11.058
[60] Arroyave R, Shin D, Liu ZK. Modification of the thermodynamic model for the Mg–Zr system. *CALPHAD 2005*;29:230–8.
[61] Lee, Y. C., Dahle, A. K., & Stjohn, D. H. (2000). The role of solute in grain refinement of magnesium. *Metallurgical and Materials Transactions A, 31*(11), 2895-2906. doi:10.1007/bf02830349
[62] Ray, A. K., & Wilkinson, D. S. (2016). The effect of microstructure on damage and fracture in AZ31B and ZEK100 magnesium alloys. *Materials Science and Engineering: A, 658*, 33-41. doi:10.1016/j.msea.2016.01.103
[63] Barnett, M., Keshavarz, Z., Beer, A., & Atwell, D. (2004). Influence of grain size on the compressive deformation of wrought Mg–3Al–1Zn. Acta Materialia, 52(17), 5093-5103. doi:10.1016/j.actamat.2004.07.015
[64] Barnett, M., Nave, M., & Bettles, C. (2004). Deformation microstructures and textures of some cold rolled Mg alloys. Materials Science and Engineering: A, 386(1-2), 205-211. doi:10.1016/j.msea.2004.07.030
[65] Agnew, S. R., & Duygulu, Ö. (2005). Plastic anisotropy and the role of non-basal slip in magnesium alloy AZ31B. International Journal of Plasticity, 21(6), 1161-1193. doi:10.1016/j.ijplas.2004.05.018

[66] Wang, H., Wu, P., Tomé, C., & Wang, J. (2012). A constitutive model of twinning and detwinning for hexagonal close packed polycrystals. *Materials Science and Engineering: A, 555*, 93-98. doi:10.1016/j.msea.2012.06.038

[67] Lee, M., Wagoner, R., Lee, J., Chung, K., & Kim, H. (2008). Constitutive modeling for anisotropic/asymmetric hardening behavior of magnesium alloy sheets. *International Journal of Plasticity, 24*(4), 545-582. doi:10.1016/j.ijplas.2007.05.004

[68] Xiong, Y., Yu, Q., & Jiang, Y. (2014). An experimental study of cyclic plastic deformation of extruded ZK60 magnesium alloy under uniaxial loading at room temperature. *International Journal of Plasticity, 53*, 107-124. doi:10.1016/j.ijplas.2013.07.008

[69] Ramberg W, Osgood WR. Description of stress–strain curves by three parameters. Technical note no. 902, National Advisory Committee for Aeronautics, Washington, DC; 1943

[70] Masing G. Zur Heynschen Theorie der Verfestigung der Metalle durch verborgene elastische Spannungen. Wissenschaftliche Veröffentlichungen aus dem Siemens-Konzern 1924;3:231–9.

[71] Cáceres, C., Sumitomo, T., & Veidt, M. (2003). Pseudoelastic behaviour of cast magnesium AZ91 alloy under cyclic loading–unloading. *Acta Materialia, 51*(20), 6211-6218. doi:10.1016/s1359-6454(03)00444-0

[72] Mann, G., Sumitomo, T., Cáceres, C., & Griffiths, J. (2007). Reversible plastic strain during cyclic loading–unloading of Mg and Mg–Zn alloys. *Materials Science and Engineering: A, 456*(1-2), 138-146. doi:10.1016/j.msea.2006.11.160

[73] Min, J., & Lin, J. (2013). Anelastic behavior and phenomenological modeling of Mg ZEK100-O alloy sheet under cyclic tensile loading–unloading. *Materials Science and Engineering: A, 561*, 174-182. doi:10.1016/j.msea.2012.11.009

[74] Wu, L., Jain, A., Brown, D., Stoica, G., Agnew, S., Clausen, B., . . . Liaw, P. (2008). Twinning–detwinning behavior during the strain-controlled low-cycle fatigue testing of a wrought magnesium alloy, ZK60A. *Acta Materialia,56*(4), 688-695. doi:10.1016/j.actamat.2007.10.030

[75] Heinz Neuber, Theory of stress concentration for shear-strained prismatical bodies with arbitrary nonlinear stress–strain law, Trans. ASME J. Appl. Mech. 28 (1961) 544–550

[76] Kujawski, D., & Teo, J. L. (2017). A Generalization of Neubers Rule for Numerical Applications. *Procedia Structural Integrity, 5*, 883-888. doi:10.1016/j.prostr.2017.07.116

[77] Hoffmann, M., & Seeger, T. (1985). A Generalized Method for Estimating Multiaxial Elastic-Plastic Notch Stresses and Strains, Part 1: Theory. *Journal of Engineering Materials and Technology, 107*(4), 250. doi:10.1115/1.3225814

[78] Lieb, K., Horstman, R., Power, B., Meltzer, R., Vieth, M., Seeger, T., & Heuler, P. (1980). Generalized Application of Neubers Rule. Journal of Testing and Evaluation, 8(4), 199. doi:10.1520/jte11613j

[79] Topper, T. H., Wetzel, R. M., Morrow, J., 1969. Neuber's Rule Applied to Fatigue of Notched Specimens. ASTM, Journal of Materials 4(1), 200-209

[80] L.Y. Lee, J. Pan, R. Hathaway, M. Barkey, Fatigue Testing and Analysis (Theory and Practice), Elsevier, 2005.

[81] Molski K, Glinka G. A method of elastic-plastic stress and strain calculation at a notch root. Mater Sci Eng 1981;50:93–100.

[82] G. Glinka, Calculation of inelastic Notch-tip strain-stress histories under cyclic loading, Eng. Fract. Mech. 2 (S) (1986) 839–954.

[83] Kilambi, S., & Tipton, S. M. (2013). Numerical evaluation of the original “Neuber’s rule” for pure out-of-plane shear loading. *The Journal of Strain Analysis for Engineering Design, 48*(8), 522-535. doi:10.1177/0309324713496407

[84] Moftakhar, A., Buczynski, A., & Glinka, G. (1995). Calculation of elasto-plastic strains and stresses in notches under multiaxial loading. *International Journal of Fracture, 70*(4), 357-373. doi:10.1007/bf00032453

[85] Ye, D. (2004). Further investigation of Neuber’s rule and the equivalent strain energy density (ESED) method. *International Journal of Fatigue, 26*(5), 447-455. doi:10.1016/j.ijfatigue.2003.10.002

[86] Ye, D., Hertel, O., & Vormwald, M. (2008). A unified expression of elastic–plastic notch stress–strain calculation in bodies subjected to multiaxial cyclic loading. *International Journal of Solids and Structures, 45*(24), 6177-6189. doi:10.1016/j.ijsolstr.2008.07.012

[87] Matsuishi, M. & Endo, T. (1968) Fatigue of metals subjected to varying stress, Japan Soc. Mech. Engineering.

[88] Downing, S.D., Socie, D.F. (1982). Simple rainflow counting algorithms. International Journal of Fatigue, Volume 4, Issue 1, January, 31-40.

[89] ASTM E 1049-85. (Reapproved 2005). "Standard practices for cycle counting in fatigue analysis". ASTM International.

[90] Dowling, N. (2003). Local Strain Approach to Fatigue. *Comprehensive Structural Integrity,* 77-94. doi:10.1016/b0-08-043749-4/04031-3

[91] Jahed, H., & Dubey, R. N. (1997). An axisymmetric method of elastic-plastic analysis capable of predicting residual stress field. *Journal of pressure vessel technology*, *119*(3), 264-273.

[92] Jahed, H., Lambert, S. B., & Dubey, R. N. (1998). Total deformation theory for non-proportional loading. *International journal of pressure vessels and piping*, *75*(8), 633-642.

[93] Jahed, H., Sethuraman, R., & Dubey, R. N. (1997). A variable material property approach for solving elastic-plastic problems. *International journal of pressure vessels and piping*, *71*(3), 285-291.

[94] Jahed, H., Moghadam, B. A., & Shambooli, M. (2006). Re-autofrettage. *Journal of pressure vessel technology*, *128*(2), 223-226.

[95] Faghih, S., Jahed, H., & Behravesh, S. B. (2018). Variable Material Properties (VMP) Approach: A Review on Twenty Years of Progress. *Journal of Pressure Vessel Technology*.

[96] Jahed, H., Lambert, S. B., & Dubey, R. N. (2000). Variable material property method in the analysis of cold-worked fastener holes. *The Journal of Strain Analysis for Engineering Design*, *35*(2), 137-142.

[97] Jahed, H., Farshi, B., & Hosseini, M. (2007). The actual unloading behavior effect on thermo-mechanical stress intensity factor and life of autofrettage tubes. *International journal of fatigue*, *29*(2), 360-369.

[98] Jahed, H. (2018). Private communication.

[99] Jahed, H., & Dubey, R. N. (1997). An axisymmetric method of elastic-plastic analysis capable of predicting residual stress field. *Journal of pressure vessel technology*, *119*(3), 264-273.

[100] Jahed, H., & Dubey, R. N. (1997). An axisymmetric method of elastic-plastic analysis capable of predicting residual stress field. *Journal of pressure vessel technology*, *119*(3), 264-273.

[101] Jahed, H., & Albinmousa, J. (2014). Multiaxial behaviour of wrought magnesium alloys–A review and suitability of energy-based fatigue life model. *Theoretical and Applied Fracture Mechanics*, *73*, 97-108.

[102] Noban, M., Jahed, H., Winkler, S., & Ince, A. (2011). Fatigue characterization and modeling of 30CrNiMo8HH under multiaxial loading. *Materials Science and Engineering: A*, *528*(6), 2484-2494.